University of California Santa Cruz

Mechanism and quantitation of cooperative interactions in the cyanobacterial circadian oscillator

a dissertation submitted in partial satisfaction
of the requirements for the degree of

DOCTOR OF PHILOSOPHY

in

Chemistry and Biochemistry

by

Jeffrey A. Swan

June 2022

The dissertation of Jeffrey A. Swan
is approved:

_____
Professor Carrie L. Partch, Advisor

_____
Professor Michael D. Stone

_____
Professor Fitnat H. Yildiz

_____
Peter F. Biehl
Vice Provost of Graduate Studies

Table of Contents

List of Figures

List of Tables

Abstract

Title: Mechanism and quantitation of cooperative interactions in the cyanobacterial circadian oscillator.

Author: Jeffrey Swan

Cyanobacteria are photosynthetic microbes that have shaped the very environment of the world we live in over several billion of years. This is, in large part, because of their ability to perform the chemically exclusive processes of photosynthesis and nitrogen fixation. To segregate these processes temporally, they have evolved an elegant and complex circadian clock that aligns their physiology with the solar day to maximize biological fitness. This clock keeps time through the action of a biochemical oscillator comprising just three proteins: KaiA, KaiB and KaiC, that, along with ATP, can recapitulate a 24-h pacemaking activity *in vitro*. This process is achieved by a negative feedback loop akin to a biochemical game of *Rock, Paper, Scissors*, whereby the phosphorylation state of the hexameric ATPase KaiC is controlled by the nucleotide exchange factor KaiA, the ability of KaiA to stimulate KaiC repression is controlled by the metamorphic protein KaiB, and the ability of KaiB to inactivate KaiA is controlled by KaiC phosphorylation state. This creates a repetitive biochemical cycle that takes just bout 24 hours to complete. Additionally, the output proteins SasA and CikA interact with the clock in various phases of the biochemical oscillation that influence their ability to activate the master circadian

transcription factor RpaA and orchestrate circdain gene expression throughout the cyanobacterial cell.

This thesis focuses on the relationship between KaiC and KaiB. In particular, on positive cooperativity that increases KaiB's affinity for KaiC, or in other words, the process by which initial binding of KaiB to the KaiC hexamer enables more efficient recruitment of KaiB to the remaining 5 binding sites. While this effect is well documented when considering KaiB and KaiC on their own, in Chapter 2 we expand this concept in the in the context of the entire reconstituted clock system including output pathways that link biochemical oscillation to DNA binding by the transcription factor RpaA. In doing so, we uncovered the unexpected result that SasA expands the range of permissive KaiB concentrations for biochemical oscillation to occur. I showed that SasA does this by binding to KaiC analogously to how KaiB does, and then recruiting additional KaiB molecules through positive heterotropic cooperativity. Integrating a novel crystal structure of the interacting domains of KaiC and SasA with existing crystal structures of the KaiC hexamer, I identified SasA mutations that abrogate heterotropic cooperativity but have only minor effects on the output signaling function of SasA. Remarkably, cyanobacteria bearing these mutations have defective circadian rhythms, demonstrating that SasA's ability to bolster KaiB recruitment is an evolved aspect of biochemical oscillation.

Chapter 3 describes our structural analysis of phosphomimetic variants of KaiC that differ in their ability to bind KaiB. Because crystallography has failed to identify the structural basis of this discrimination previously, we employed cryo-

electron microscopy to analyze KaiC particles as a structural ensemble frozen in ice. Each KaiC protomer is composed of two ATPase domains, termed CI and CII. The phase-determining phosphosites are located on CII, and KaiB binds to KaiC over 70 Å away to the ADP-bound form of CI. Our data corroborated previous studies that daytime KaiC, which does not bind KaiB, loses interactions amongst the CII domain protomers within the hexamer, while maintaining a hexameric CI domain. Additionally, we obtained a relatively high resolution (3.2 Å) structure of a compressed form of KaiC where the CII domain breaks into a split washer with 2-fold symmetry, causing two of the CII domain subunits to interact more tightly with their respective CI domains. Using mutagenesis and various functional assays, I identified an allosteric conduit that connects the ATPase domains of the CI and CII domains of KaiC in both intra-protomer and inter-protomer contexts. Importantly, I trace these interactions back to cooperativity in KaiB association, with mutants along the pathway disrupting both KaiB affinity and cooperativity. Furthermore, I link KaiB cooperativity to ATP hydrolysis in the CI domain by identifying a key residue that senses CI nucleotide state. This residue is dispensable for both ATP hydrolysis as well as KaiB association, but is critical for both KaiB cooperativity and *in vivo* circadian rhythms. This, along with additional nucleotide dependence studies reported in Chapter 4, suggests that allosteric control of cooperativity through the CI active site is the structural basis for restriction of KaiB association to the nighttime KaiC phosphostates.

Finally, in the latter half of Chapter 4 I summarize experiments that used the solvatocromatic dye Sypro Orange to detect changes in KaiC structure as a function of temperature and mutagenesis. I describe our preliminary efforts to build on these results by identifying additional solvatochromatic dyes that can leverage this effect to report continuously on the phase of biochemical oscillation by discriminate binding to different KaiC phosphostates at constant temperature.

~

This thesis is
dedicated to my parents,
Roy and Sue Swan.

~

Acknowledgements

The text of this dissertation includes whole or partial reprints of the following previously published material:

Swan, J. A.; Golden, S.; LiWang, A.; Partch, C. L., Structure, function, and mechanism of the core circadian clock in cyanobacteria. *J Biol Chem* **2018**.

The following co-authors are acknowledged for their contributions to the published work: J.A.S. wrote the manuscript with comments and edits from C.L.P, A.L. and S.G.

Chavan, A. G.; Swan, J. A.; Heisler, J.; Sancar, C.; Ernst, D. C.; Fang, M.; Palacios, J. G.; Spangler, R. K.; Bagshaw, C. R.; Tripathi, S.; Crosby, P.; Golden, S. S.; Partch, C. L.; LiWang, A., Reconstitution of an intact clock reveals mechanisms of circadian timekeeping. *Science* **2021,** *374* (6564), eabd4453.

The following co-authors are acknowledged for their contributions to the published work: conceptualization, A.G.C., J.A.S., J.H., S.S.G., C.L.P., and A.L.; methodology, A.G.C., J.H., J.A.S., C.S., D.C.E., M.F., and C.R.B.; investigation, A.G.C., J.A.S., J.H., C.S., D.C.E., M.F., J.G.P., R.K.S., and S.T.; validation, A.G.C., J.A.S., J.H., C.S., D.C.E., M.F., and S.T.; formal analysis, A.G.C., J.H., J.A.S., C.R.B., P.C., C.S., D.C.E., and M.F.; resources, S.S.G., C.L.P., and A.L.; data curation, A.G.C., J.H., J.A.S., and C.S.; writing – original draft, A.G.C., J.H., J.A.S., C.L.P., and A.L.;

writing – reviewing and editing, A.G.C., J.A.S., J.H., D.C.E., C.R.B., S.S.G., C.L.P., and A.L.; funding acquisition, J.H., J.G.P., P.C., S.S.G., C.L.P., and A.L.; supervision, S.S.G., C.L.P., and A.L.; A.G.C., J.A.S and J.H. contributed equally to this work.

Chavan, A. G.; Swan, J. A.; Heisler, J.; Sancar, C.; Ernst, D. C.; Fang, M.; Palacios, J. G.; Spangler, R. K.; Bagshaw, C. R.; Tripathi, S.; Crosby, P.; Golden, S. S.; Partch, C. L.; LiWang, A., Coupling of distant ATPase domains in the circadian clock protein KaiC. *Nature Structural and Molecular Biology* **2022** (*in press*)

The following co-authors are acknowledged for their contributions to the published work: conceptualization, J.A.S., C.R.S., G.L., C.L.P.; investigation, J.A.S., C.R.S., A.G.C., A.M.F., D.E., C.S., D.C.E., J.G.P.; funding acquisition, S.S.G., A.L., G.L., C.L.P.; project administration, J.A.S., G.L., C.L.P.; supervision, S.S.G., A.L., G.L., C.L.P. writing – original draft, J.A.S., C.R.S., G.L., C.L.P. writing – review & editing, J.A.S., C.R.S., S.S.G., A.L., G.L., C.L.P.; J.A.S and C.R.S. contributed equally to this work.

Chapter 1: Introduction to the cyanobacterial clock

1.1 Form and Function of Circadian Clocks

Circadian rhythms are processes through which cells and organisms predict and adapt to the repetitive environmental changes incident to the 24-hour solar day. These rhythms originate intracellularly and persist in the absence of external cues to orchestrate temporal organization of physiology (*1*). To achieve this, circadian clocks must perform three distinct but necessarily intertwined functions: *timekeeping*, *entrainment* and *output signaling*.

Timekeeping is achieved through a cycle of slow biochemical processes that together set the period of oscillation close to 24 hours. For this temporal information to be relevant, biological clocks must appropriately synchronize with their environment through the process of *entrainment*. To actuate its various cellular and organismal effects, temporal information is transmitted from the timekeeping apparatus to the rest of the cell through *output signaling* mechanisms that impart circadian changes in physiology.

Timekeeping mechanisms that have been observed in circadian clocks are broadly categorized as transcription-translation feedback loops (TTFLs) or post-translational oscillators (PTOs) (*2*). TTFLs achieve oscillation via delayed negative feedback, where a gene product represses its own expression when its levels become high enough. This results in an oscillation in the expression level of the gene, with transitions between repression and derepression occurring at critical points in the

oscillatory cycle. By contrast, PTOs utilize timekeeping mechanisms that are independent of transcription. Like TTFLs, PTOs are oscillatory processes; however, instead of being driven by changes in expression levels, their behavior is controlled by post-translational modifications, conformational changes, protein-protein interactions and/or subcellular localization.

Post-translational steps in circadian clocks present unique biochemical challenges and opportunities because they link dynamic molecular processes to biological phenotype through covalent and conformational changes in protein structure. PTOs can operate at constant protein concentrations, and are therefore amenable to *in vitro* study. In the cyanobacterial Kai (*Japanese*, 回, "cycle") system, an entire PTO consisting of only three protein gene products (KaiA, KaiB and KaiC; or KaiABC) can reconstitute circadian biochemical oscillation *in vitro* (*3*). As a result, this system has become an important model for understanding how discrete biochemical steps are integrated to give rise to precise biological timing.

1.2 Circadian Biology in Cyanobacteria

Circadian rhythms are essentially ubiquitous in eukaryotes, but far fewer instances have been documented in prokaryotes (*4*). Cyanobacteria temporally segregate photosynthesis and nitrogen fixation, which require mutually exclusive oxidative environments (*5*). Evolutionary pressures such as this resulted in a cyanobacterial transcriptome in which at least one third of transcripts undergo circadian variation in accumulation levels (*6*) and active transcription of nearly all

transcripts appears to be under circadian control (*7*). These changes in transcriptional output are linked to global changes in chromosome ultrastructure (*8, 9*), but are controlled basally by a core biochemical oscillator (*3, 10*).

The KaiABC gene cluster was originally identified in genetic screens aimed at finding TTFLs involved in cyanobacterial circadian regulation, with deletion resulting in an arrhythmic phenotype (*10*). It was subsequently shown that the products of this gene cluster can recapitulate circadian biochemical oscillation *in vitro* (*3*), and that this circadian oscillation persists *in vivo* even when transcription and translation are inhibited (*11*). Its ability to be reconstituted *in vitro* demonstrates that KaiABC can act as a self-sustained PTO. *In vivo*, this PTO also functions within a TTFL framework; i.e. circadian variation of clock protein expression resulting in a more robust rhythm (*4, 12-14*). Together with three other effector proteins, the KaiABC oscillator comprises a self-contained minimal system that is capable of integrating *timekeeping*, *entrainment* and *output signaling* processes into the cyanobacterial cell.

Domain structures of the six core clock proteins in cyanobacteria are shown in **Fig. 1.1**. Genetic studies on cyanobacterial rhythms have made extensive use of the mesophilic cyanobacterium *Synechococcus elongatus*, from which these genes were originally identified (*10*). Biophysical studies have often taken advantage of proteins produced from homologous gene sequences in the thermophilic variant *Thermosynechococcus elongatus* for their improved solubility and *in vitro* behavior (*17*).

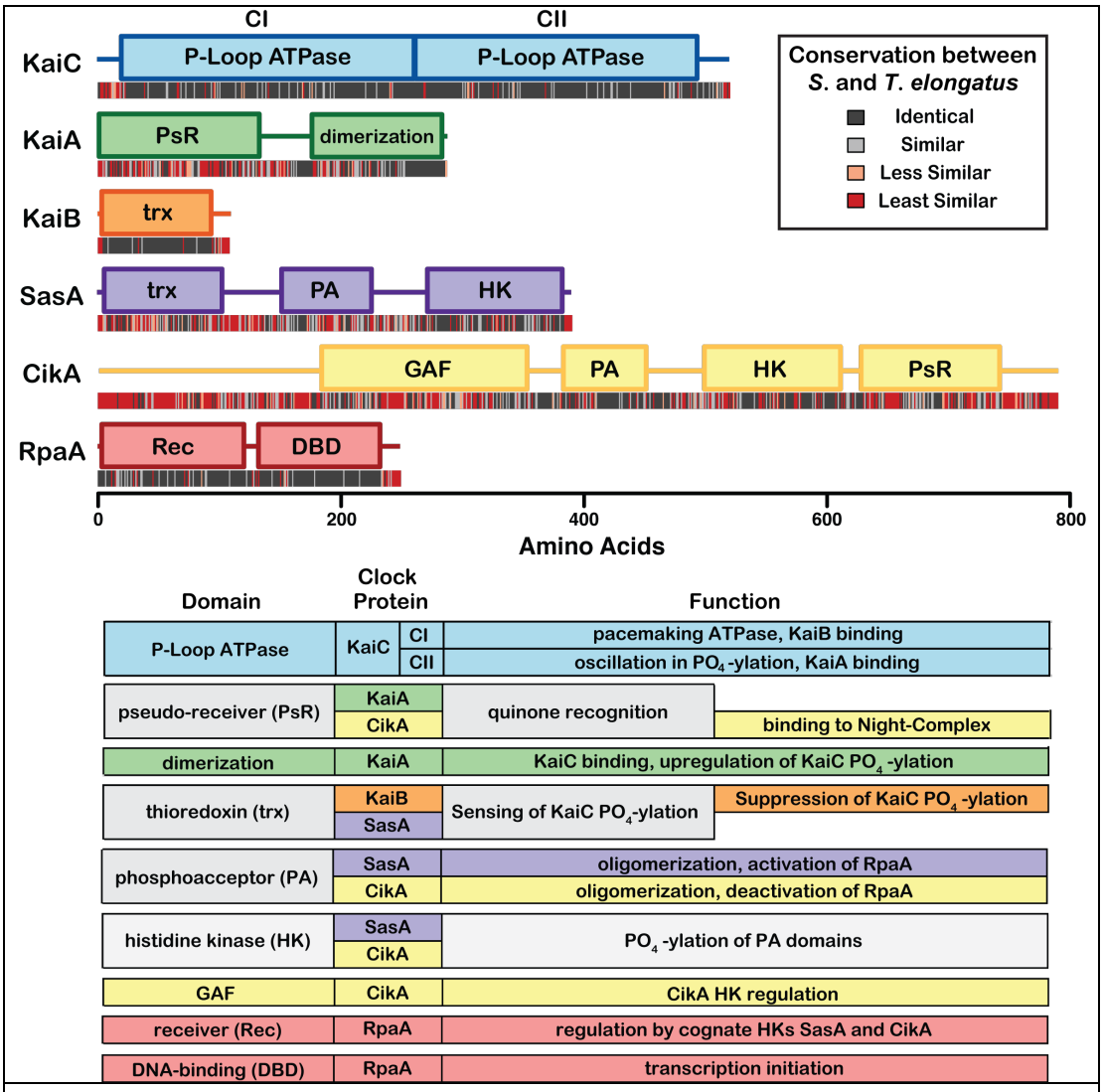

Figure 1.1: Domain structure, conservation, and function of core circadian clock proteins.
Domain structures of the six core clock proteins from S. elongatus are depicted as colored bars using boundaries and bioinformatically predicted functions from the Interpro database *(15)*. Sequences were aligned with homologs from the thermophilic variant T. elongatus using ClustalΩ *(16)*. Identity scores at each position in the alignment are indicated below the domain maps as color-coded bars. A color-coded table summarizes observed function for each of the core clock protein domains.

The six proteins shown in **Fig. 1.1** are conserved between *S.* and *T. elongatus*, and appear to comprise a core unit capable of accounting for all of the required

functions of a circadian clock. Several additional genes have been identified that play roles in the circadian rhythms of cyanobacteria (*18-23*), however this review will focus on the six best-characterized gene products and the mechanisms through which they mediate timekeeping, entrainment and output signaling functions in cyanobacterial circadian rhythms. For a broader review on circadian biology in cyanobacteria, see references (*4, 24*).

1.3 Structure and Function of KaiC

The core cyanobacterial clock is centered around the hexameric ATPase KaiC, which achieves *timekeeping* through circadian oscillations in phosphorylation that are intertwined with oscillations between the quaternary structures depicted in **Fig. 1.2**. The primary sequence of KaiC is a concatenation of two P-loop ATPase domains (*10*), termed CI and CII. In solution, KaiC binds adenosine triphosphate (ATP) to form a hexamer through interactions at the CI subunit interfaces (*25-27*). Homologous ATPase active sites are present at the subunit interfaces of both CI and CII, however, these active sites catalyze distinct chemical transformations. CI transfers phosphate from ATP to water, and CII catalyzes transfer of phosphate between ATP and the sidechain hydroxyl groups of residues S431 and T432 (*28, 29*). Phosphorylation at these sites oscillates circadianly in concert with interactions

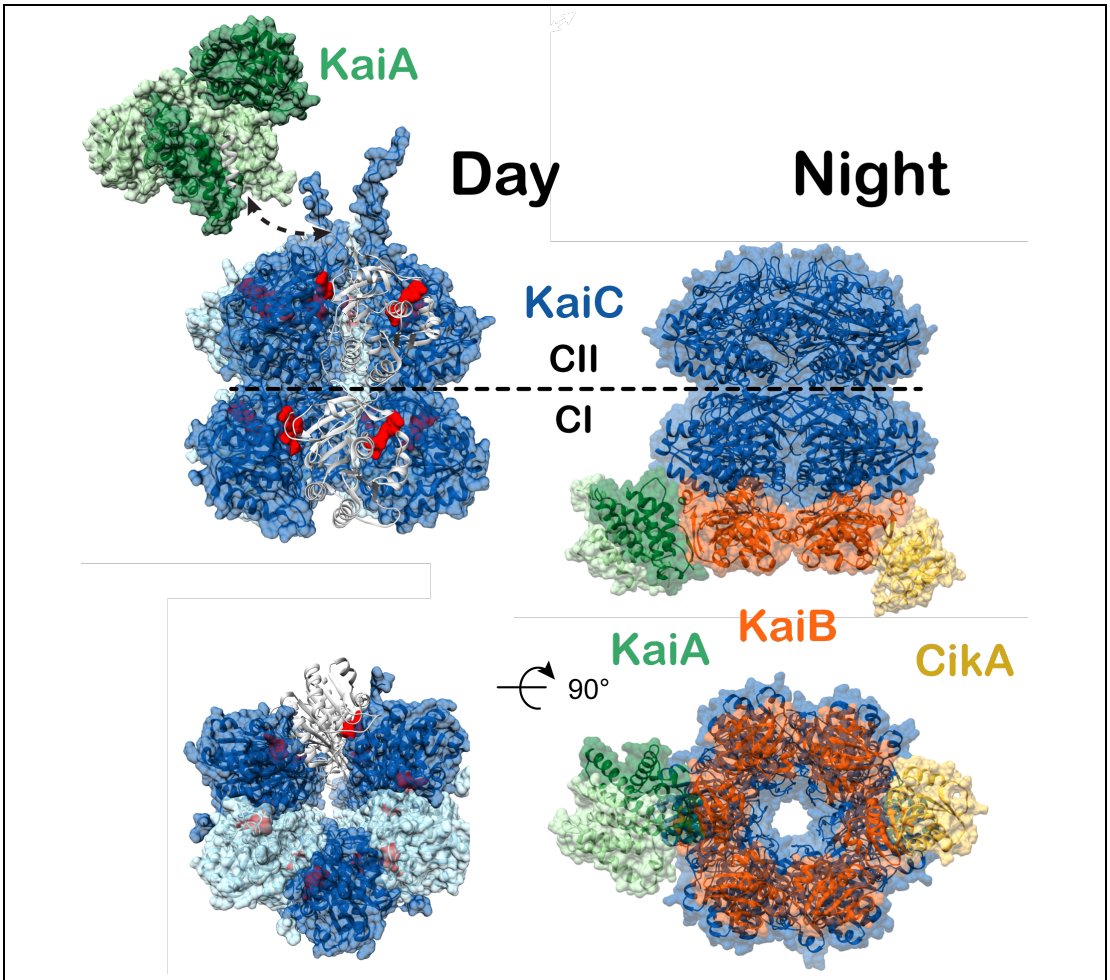

Figure 1.2: Day and Night States of the cyanobacterial clock.
High resolution models of the day and nighttime states of the core oscillator are compared. Coloring scheme is the same as in Figure 1. **A)** The Day Complex. The CI and CII hexamers form stacked doughnuts (alternating subunits shown in light and dark blue for contrast, PDB:3K0C). One subunit is shown in cartoon mode to highlight the nucleotide binding sites at the subunit interfaces (red). The KaiA dimer (light and dark green for contrast) binds to C-terminal A-loops of KaiC (shown bound to KaiA in white, PDB:5C5E). The dashed arrow represents the point of connection between the KaiA-CII loop structure and the CII A-loop extensions shown on the right. **B)** The Night Complex. The intermediate-resolution cryo-EM model (PDB:5NYT) is combined with higher resolution models from studies on independent subcomplexes. The S431E phosphomimetic of the pS/T state of KaiC binds six molecules of KaiB through its B-loops (PDB:5JWQ). This results in the recruitment and sequestration of KaiA near the KaiB-CI interface (PDB:5JWR). Output signaling occurs through interactions between KaiB and the C-terminal PsR domain of CikA (PDB:5JYV), as well as through interactions

between KaiC and SasA at dusk, though no high-resolution structure exists for the latter.

between KaiC and the other core clock proteins KaiA and KaiB (*30, 31*). These interactions are regulated by the phosphostate of KaiC, and take place on non-homologous regions of the CI and CII domains, known as the respective B and A-loops, where they in turn regulate the enzymatic activities on KaiC in a negative feedback loop.

During the day, KaiA is bound to the A-loops on CII where it promotes autophosphorylation (*32-34*). In the evening, KaiB binds to phosphorylated KaiC at the B-loops of the CI domain (*35*) through a slow conformational selection mechanism (*36*), adding a third stacked toroid to the KaiC double-doughnut (*37*) (**Fig. 1.2**). At this point, KaiA is recruited to the KaiB-CI complex where it is inactivated, sequestering it from CII throughout the night (*35, 37*). In the absence of KaiA, enzymatic equilibria at the CII active sites favor the autodephosphorylation of T432 and S431 (*33*). Around dawn, CII phosphorylation is at a minimum and affinity for KaiB is lost (*32*). The repressive complex is released, freeing KaiA to bind to the A-loops and begin the cycle anew.

Post-translational modification at residues S431 and T432 of KaiC occurs in a specific order, with T432 acting as a substrate in the first reaction of both the phosphorylation and dephosphorylation arms of the cycle (*31, 38*). The order of the KaiC phosphorylation states is denoted in this review using the shorthand: S/T → S/pT → pS/pT → pS/T. The S/T and S/pT states are dominant during the daytime

phosphorylation arm of the oscillatory cycle, characterized by binding of KaiA at CII[26,28]. Accumulation of pS/pT initiates the nighttime state (*30, 32, 37*), characterized by the formation of the KaiABC complex, which persists through the pS/T state until phosphorylation reaches a minimum and KaiA is recruited back to CII.

Sustained oscillation requires a power source, and KaiABC appears to achieve this through ATPase activity of the CI domain, whose enzymatic activity is correlated with period both *in vitro* and *in vivo* (*39, 40*). CI ATPase activity oscillates circadianly, with the unphosphorylated forms of KaiC consuming ATP approximately twice as fast as the phosphorylated form (*39*). This enzymatic activity shows a relatively modest rate enhancement of ATP hydrolysis, with an apparent k_{cat}/K_m on the order of 10^{-4} $M^{-1}s^{-1}$, about six orders of magnitude slower than the structurally similar F_1 ATPase (*40*). High-resolution structures have been obtained for the isolated CI ring in the pre-ATP and post-ATP hydrolysis states (*40*) resulting in the three specific structural changes depicted in **Fig. 1.3A** (*40*). Together with studies showing that catalytically dead KaiC is unable to interact with KaiB (*28*), one emerging model is that CI ATPase functions in timing the recruitment of KaiB and resultant formation of the nighttime repressive complex, though no specific structural or biochemical information exists yet on how these two processes might be related.

A direct structural connection between CII phosphorylation and the interactions of KaiC with other clock proteins has also proven difficult to pin down. High-resolution crystal structures exist of different phosphorylated and

phosphomimetic states (*41*), but these structures overlay almost perfectly. This is unexpected given the well-established functional differences between the phosphostates of KaiC. One possible explanation for this structural convergence is that crystallization of KaiC variants in these structures was performed in the presence of non-hydrolyzable ATP analogue (*26, 41*), and structural changes associated with CII phosphorylation could be masked in the pre-ATP hydrolysis state. Alternatively, phosphorylation may influence dynamic structural equilibria that are not observable within a crystal lattice.

The latter idea is supported by lower-resolution studies on the overall shape and dynamic structural properties of KaiC. Time-resolved small angle X-ray scattering data that show an increase in the apparent radius of gyration in the pS/T phosphostate (*42*), providing evidence of a change in shape for KaiC in the night. Interactions between isolated CI and CII domains increase across the phosphorylation cycle with a minimum at the ST state and a maximum in the pS/T state (*43*), and NMR line-shape analysis indicates a more rigid KaiC structure in these states as well (*43*). These structural changes, known collectively as "ring-ring stacking," presumably affect the accessibility of the B-loops to regulate binding of thioredoxin domains.

One of the most surprising observations related to the enzymology of CII is that free radioactive ATP accumulates transiently in dephosphorylation reactions of ^{32}P-labeled pS/pT KaiC (*44*), suggesting that dephosphorylation occurs by transfer of

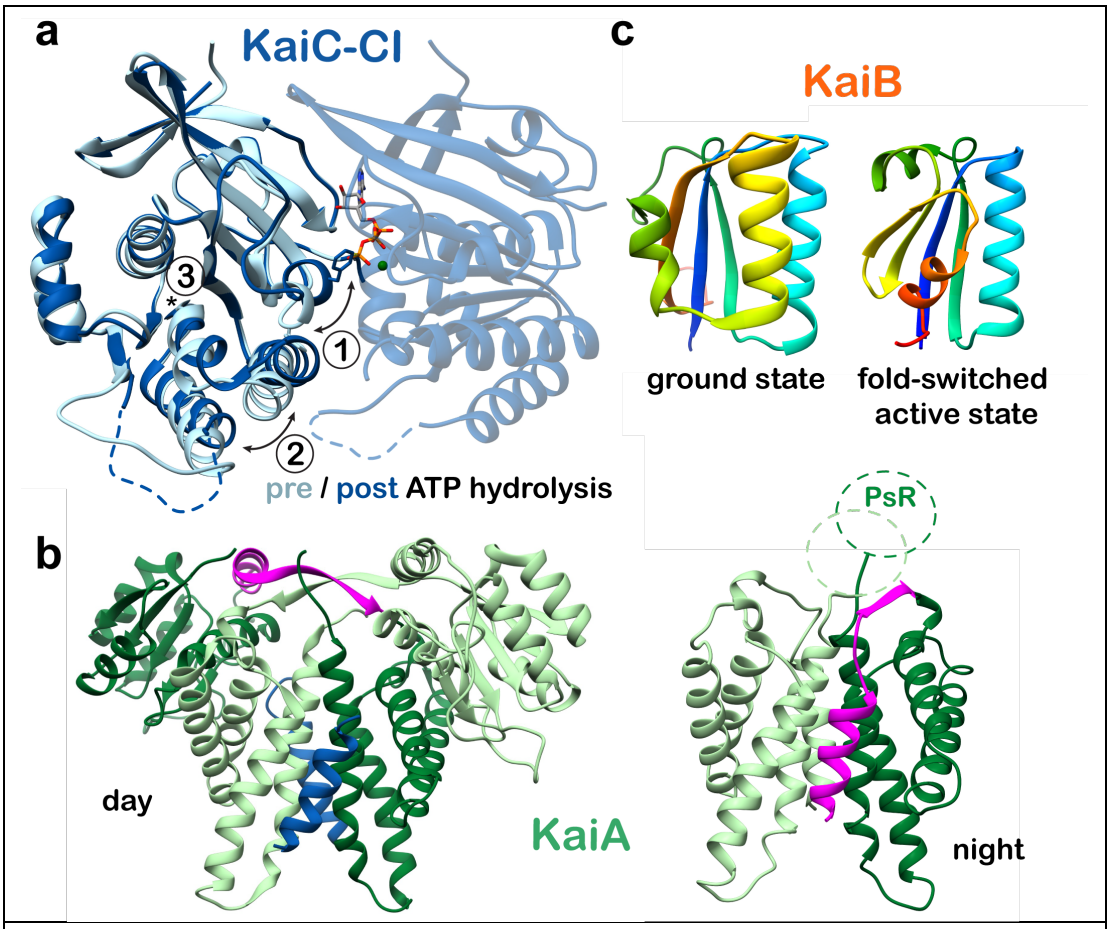

Figure 1.3: Conformational Changes in the Core Oscillator.
A) CI ATP hydrolysis. High-resolution crystal structures of the CI domain of KaiC in the ATP-bound (PDB:4LTA) and ADP-bound states (PDB:4LT9, chain C) are overlaid. Three major structural differences are noted upon ATP hydrolysis: 1) The helix bearing F199 is flipped into an alternate conformation, 2) the α6-α7/α8 helices are repositioned away from the nucleotide binding site, and 3) the *cis* peptide bond between D145 and S146 in the ATP-bound state is found in the *trans* isomer in the ADP-bound state. **B)** KaiA inactivation. The daytime and nighttime states of KaiA are compared. During the day, the A-loops of KaiC (blue) are bound at the dimer interface, and the interdomain linker (pink) crosses over the complex. In the Night Complex, the linker shifts to occupy the A-loop binding site. **C)** KaiB fold-switching. KaiB undergoes a major structural reorganization between its free and KaiC-bound forms, involving changes in both secondary and tertiary structure for the C-terminal half of the protein. Both structures are represented with rainbow coloring, starting with dark blue at the N-terminus. Note that the first half of the two proteins is identical (dark blue through light green), while the C-terminal halves are completely different. This interconversion is thought to happen spontaneously resulting in a conformational selection mechanism for formation of the KaiBC complex.

phosphate from sidechains on KaiC to the β-phosphate of an adenosine diphosphate (ADP) nucleophile. The surprising ability of KaiC to catalyze this energetically expensive reaction has garnered speculation of an evolutionary relationship with F_1F_0 ATP synthase (*45*), which also takes on a double-doughnut-like structure (*46*). Because phosphorylation and dephosphorylation reactions on KaiC-CII appear to occur via the same chemistry going in opposite directions, the equilibrium can be regulated by substrate availability and ground state interactions without major restructuring of the active-site. This model is consistent with the apparent mechanisms by which KaiA regulates CII phosphorylation, as described below.

1.4 KaiA: Primary Regulator of KaiC Phosphorylation

KaiA acts as the primary regulator of enzymatic activity on the CII domain of KaiC, and therefore, the phosphorylation cycle in general. Throughout the day, KaiA promotes phosphorylation of CII via two distinct mechanisms: 1) structural rearrangement of the CII catalytic core (*34, 47*) and 2) exchange of active-site ADP molecules for ATP (*48*). The enzymatic equilibrium of CII favors phosphatase activity when KaiC is in isolation (*33*) making KaiA occupancy the primary determinant of enzymatic equilibrium on CII.

Without KaiA bound, the A-loop residues project into the central cavity of KaiC(*34*). KaiA competes away interactions in this position, binding the loops and causing them to take on an α-helical conformation (*49*). When these loops are deleted, CII is in constitutive phosphorylation mode (*34*), indicating that the

interaction of the A-loops with the cavity of KaiC abrogates CII phosphorylation and that KaiA disrupts those interactions. Additionally, KaiA has been shown to act as a nucleotide exchange factor, controlling the equilibrium of phosphorylation on CII at the level of substrate availability (*48*). KaiA increases the rate of ATP/ADP exchange on KaiC as well as the ratio of bound ATP at equilibrium (*48*). Hence, KaiA promotes CII phosphorylation by increasing the local concentration of ATP, as well as by direct perturbation of the active site.

Inactivation of KaiA during the night occurs through a conformational change that abrogates its A-loop binding activity (Figure 3B). In the daytime state, the A-loops of KaiC form a helical bundle with the KaiA dimerization interface, flanked on either side by its N-terminal pseudo-receiver (PsR) domains. In this conformation, each β-strand from the interdomain linker crosses close to the other to form an intermolecular β-sheet, followed by a helical linker connecting the PsR domain. A high-resolution crystal structure of KaiA in the nighttime state was obtained by crystallizing its C-terminal dimerization domain and interdomain linker as part of a complex with KaiB and an engineered monomeric form of the KaiC-CI domain (*37*). In this structure, KaiA docks onto an exposed β-sheet on KaiB in the KaiBC complex using the β-strand of its interdomain linker, which repositions the helical linker to dock into its own A-loop binding site. The intramolecular interaction between the α-helix of the interdomain linker and the dimerization interface precludes binding to an A-loop peptide from another KaiC hexamer, which demonstrates that binding to the KaiBC complex stabilizes an autoinhibited form of KaiA at night. The PsR domains

of KaiA are not needed to bind KaiBC (*50*) and were omitted for this structure. This structure of an isolated CI-KaiB-KaiA complex agrees with a lower-resolution model obtained by cryo-electron microscopy using full-length wild-type KaiA, KaiB and hexameric KaiC fully assembled in the nighttime state (*51*). Although the PsR domains were included here, they did not give sufficient density to be built into the model, suggesting that they are flexibly tethered to the complex.

1.5 KaiB: Attenuator of KaiC Phosphorylation

The dephosphorylation arm of the KaiABC oscillatory cycle is initiated by the binding of KaiB at the CI domain of KaiC, followed by inactivation of KaiA. Historically, some discord has existed surrounding the location of KaiB binding on KaiC and how this leads to a shift of phosphorylation equilibrium that lasts through the night. Recently, a series of corroborative structural and biochemical studies (*35-37, 51, 52*) have put this controversy to rest. Our understanding of the role of KaiB in the clock has expanded immensely through the discovery of a major conformational rearrangement that occurs between the free and KaiC-bound states of KaiB. In the ground state, KaiB takes on the unique fold depicted in **Fig. 1.3C** and oligomerizes to form a dimer of dimers (*53-55*). When bound to the CI domain of KaiC, KaiB is in a monomeric thioredoxin fold (*36*), referred to as a 'fold-switched' state because it comprises a major conformational shift involving reassignment of secondary and tertiary structure in roughly 50 residues comprising the C-terminal half of KaiB.

Binding of KaiB to KaiC occurs remarkably slowly, taking hours to go to completion *in vitro* (*35, 55*). This binding is quickened by mutations that favor the dimeric or thioredoxin-like monomeric states of KaiB (*36, 55*). Native mass-spectrometry experiments have shown that binding occurs through a monomeric form of KaiB (*56*), and appears to be cooperative, as masses were obtained for KaiC bound to either one KaiB molecule or six, but none of the subsaturated stoichiometries in between (*56*). Together, these results suggest that KaiB binds through a conformational selection mechanism, in which the ground state dimeric and tetrameric forms of KaiB act as a thermodynamic sink to decrease the concentration of KaiC binding-competent KaiB monomer and limiting the rate of binding.

Several different mutations have been identified that stabilize the KaiB monomer, each of which take on the fold-switched conformation (*36, 37*). In addition to increasing the rate of binding to KaiC *in vitro*, these mutations halt circadian oscillation *in vitro* and *in vivo*, resulting in a dominant arrhythmic phenotype that locks KaiC in the unphosphorylated state (*36*). In the fold-switched form, KaiB forms a ternary complex with KaiA and the CI domain of KaiC (*36, 37*), thus rendering KaiA inactive and mediating the dephosphorylation arm of the cycle. Together, these studies paint a unified picture of the repressive state of the cyanobacterial oscillator, and highlight the clarifying role of structural biology, which together with genetic and biochemical studies have demonstrated how the three proteins of the cyanobacterial circadian PTO work in concert with one another to sustain biochemical oscillation.

1.6 Output Signaling: SasA, CikA and RpaA

Output signaling from the cyanobacterial PTO takes place through a two-component regulatory system (*57*). Two-component systems are pervasive in bacterial sensing and signal transduction (*58*). In the archetypal form, they consist of a sensor histidine kinase (HK) and a response regulator (RR) (*59, 60*). There is often overlap between cognate RRs and HKs; for example, an HK may activate multiple RRs, or an RR may be regulated by multiple HKs (*61*). Moreover, the relevant active domains of the components may reside within a single protein that has both kinase and substrate functions. Cross-talk between regulatory networks increases dramatically from prokaryotes to eukaryotes (*62*), and cyanobacteria appear to fall somewhere in the middle of this complexity. The circadian signaling network in cyanobacteria is not yet fully understood, and new components are still being identified (*20, 21*).

Despite the general complexity of regulatory networks in cyanobacteria, a two-component system consisting of two HKs and one RR stands out as being centrally involved in output signaling from the KaiABC oscillator (*57, 63*). RpaA is an RR that governs transcription from a locus encoding additional transcription factors that mediate the global changes in gene expression associated with circadian rhythms (*64*). This regulon includes the cotranscribed KaiBC genes, thus integrating the PTO into a TTFL (*65*).

RpaA is regulated by two cognate HKs, SasA and CikA (*63*). The sensor domain of SasA adopts a thioredoxin fold that is almost identical in structure to the

fold-switched form of KaiB (*36, 66*) and binds to the pS/pT form of KaiC (*36, 63, 67*). Activation of SasA follows a canonical HK signaling mechanism. The sensor domains on SasA recognizes and binds to phosphorylated KaiC, resulting in autophosphorylation of H161 in the SasA kinase domain (*63*) and subsequent transfer of that phosphate to D53 on RpaA, rendering the transcription factor competent for DNA-binding (*65*).

SasA was originally reported to form a trimer in solution (*67*) based on analytical ultracentrifugation, and gel filtration experiments support a stoichiometry of one SasA trimer per KaiC hexamer. However, HKs usually oligomerize as dimers, though in rare cases they have been found to function as higher order oligomers (*68*) or monomers (*69*). More recent studies have reported SasA as a dimer in solution by native mass spectrometry (*70*).

At the biochemical level, SasA competes with KaiB for the B-loops on the CI domain of phosphorylated KaiC (*50*). Binding of SasA is faster than that of KaiB, presumably due to the refolding requirement of KaiB and its conformational selection (*36, 67*). This difference suggests an evolutionary selection for the metamorphic properties of KaiB in controlling the temporal window of SasA signaling, in addition to providing a timing cue for the oscillatory cycle, though more evidence is needed to support either of these models definitively. KaiA also plays a role in the competition between KaiB and SasA for the CI domain of KaiC. While the presence of KaiA does not affect k_{obs} for binding of KaiB to KaiC, it does make a difference in competitive KaiB binding when KaiC is pre-bound with SasA (*50*). This property implicates a

role for KaiA in active eviction of SasA by KaiB, though no physical model for this currently exists.

The activating effect of SasA on RpaA is reversed by CikA, a multi-domain protein that, in addition to its role in dephosphorylating RpaA, ties the clock to subcellular localization and entrainment functions (*71-74*). CikA is incorporated into the Night Complex through the interactions of its pseudo-receiver (PsR) domain with fold-switched KaiB at an interface that overlaps with the KaiA binding site (**Fig. 1.2**). Consistent with a potential competitive mechanism, inclusion of the CikA PsR domain in an *in vitro* oscillation reaction results in shortened period and decreased amplitude (*36*) Combined with the observation that CikA knockout results in a relatively severe gene expression phenotype (*75*), these data suggest that CikA has a more integral role in the *timekeeping* functions *in vivo* than suggested by the known *entrainment* and *output signaling* functions. The integrated roles of CikA and the other core clock proteins are summarized in **Fig. 1.4**.

1.7 Metabolic of Entrainment of the Clock

The cyanobacterial circadian clock achieves *entrainment* by linking the oscillatory cycle to photosynthesis through metabolic processes (*76*), rather than direct entrainment by light via sensory photoreceptors, as is commonly found in eukaryotic organisms (*77*). This metabolic entrainment of the cyanobacterial clock occurs in two ways: through sensitivity of the phosphorylation cycle to ATP/ADP ratios within the cell (*78*) and through the presence of nighttime-associated

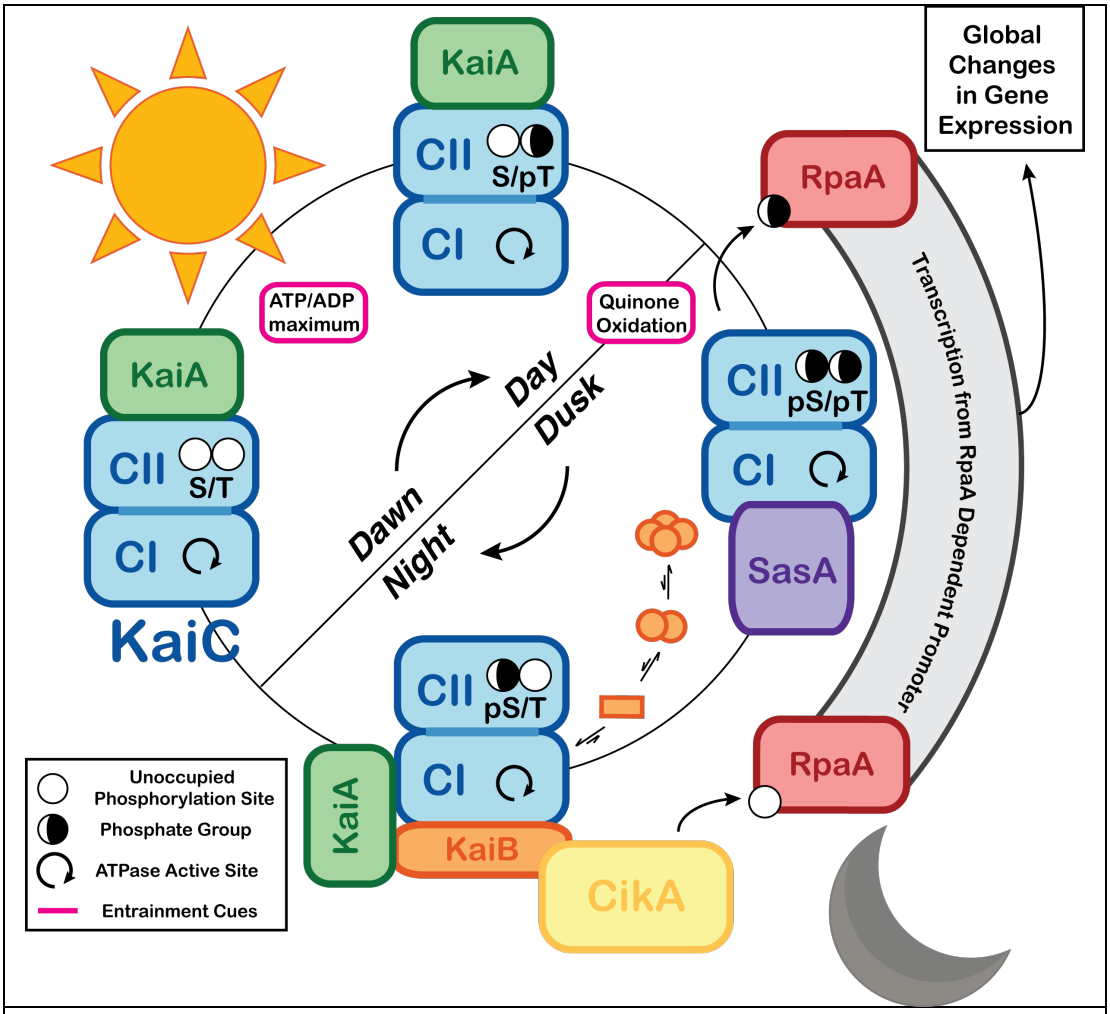

Figure 1.4: Integrated *timekeeping*, *entrainment* and *output signaling* functions of the cyanobacterial clock.
Timekeeping, entrainment and output signaling functions are highlighted within the oscillatory cycle of the cyanobacterial clock. Powered by ATPase activity on its CI domain, of KaiC cycles through a series of phosphorylation states that is interdependent on its quaternary structure. KaiA is bound to the CII domain of KaiC during the day, stimulating phosphorylation. This process is sensitive to the ATP/ADP ratio, which peaks at midday, providing an entrainment cue. At dusk, levels of oxidized quinones rise in the cell, and the clock is entrained by this as well. Around this time, KaiC reaches the pS/pT state, and SasA binds to the CI domain to activate RpaA. CI-bound SasA is eventually competed away by KaiB. Binding of KaiB is slowed by its intrinsically unfavorable equilibrium that sequesters it in inactive states, providing an additional *timing* cue. Accumulation of KaiB in its KaiC-bound form recruits and inactivates KaiA, allowing CII dephosphorylation. The input/output protein CikA also interacts with the fold-switched form of KaiB, causing CikA to dephosphorylate RpaA, inactivating it.

photosynthetic metabolites (*74, 75, 79-81*). The former entrainment cue occurs as a result of enzymatic sensitivity of the core oscillator to ATP/ADP ratios (*78*), causing it to align with the maximal photosynthetic period at midday when this ratio is highest (*78, 82*).

Cyanobacteria utilize quinone pools as intramembrane electron shuttles, reducing them during the process of photosynthesis (*83*). As a result, the concentration of oxidized quinones rises rapidly but briefly when photosynthesis shuts down with the onset of darkness before other pathways restore the redox steady state (*79*). Ectopic introduction of oxidized quinones can entrain the clock both *in vivo* and *in vitro*, and both KaiA and CikA play roles related to entrainment through binding of their PsR domains to oxidized quinones (*74, 75, 79-81*). The aggregation state and/or stability of the proteins is affected by quinone binding *in vivo* (*74, 80*). Still, the precise mechanism by which quinone binding influences the PTO is not currently well-understood.

1.8 Applications in Synthetic Biology

There is considerable interest in synthetic biology to control temporally regulated gene expression (*84, 85*). However, even the most robust synthetic oscillators are far less effective than the fully integrated oscillation of gene expression in cyanobacteria (*86, 87*). Because of its ability to function at constant protein concentrations and provide relatively stable temporal regulation at different temperatures, it could be

enticing to reverse engineer synthetic oscillators from the cyanobacterial PTO. This has been achieved, on a rudimentary level, in a transplantation study where the core oscillator was introduced into *Escherichia coli*, resulting in weak but measurable *in vivo* circadian rhythms in KaiC phosphorylation in a natively non-circadian organism (*88*). In this study, the clock was linked to transcriptional output signaling through a two-hybrid approach, though the researchers were unable to show circadian oscillation of gene expression originating from KaiABC. Thus, a great deal of opportunity still exists to integrate the cyanobacterial PTO more deeply into the physiology of the host organism and achieve clock-driven oscillations in gene expression. Undeniably, these efforts benefit from the mechanistic advances in our understanding of the cyanobacterial PTO. Furthermore, a great deal of work has gone into computational modeling of the cyanobacterial PTO (*38, 89-92*). These studies can inform efforts to re-engineer the oscillatory period of the PTO, leading to future technologies in which the cyanobacterial PTO may be used as a starting point to introduce a flexible range of temporal routines of gene expression into target organisms.

Chapter 2: Reconstitution of an intact clock reveals mechanisms of circadian timekeeping

2.1 Abstract

Circadian clocks control gene expression to provide an internal representation of local time. Here we report reconstitution of a complete cyanobacterial circadian clock *in vitro,* including the central oscillator, signal-transduction pathways, downstream transcription factor, and promoter DNA. The entire system oscillates autonomously and remains phase coherent for many days with a fluorescence-based readout that enables real-time observation of each component simultaneously without user intervention. Leveraging this new system, we find that SasA, a circadian sensor histidine kinase associated with clock output, engages directly with KaiB on the KaiC hexamer to regulate period and amplitude of the central oscillator. SasA uses structural mimicry to cooperatively recruit the rare, fold-switched conformation of KaiB to the KaiC hexamer to form the nighttime repressive complex and enhance rhythmicity of the oscillator, particularly under limiting concentrations of KaiB. Thus, the expanded *in vitro* clock reveals new mechanisms by which the circadian system of cyanobacteria maintains the pace and rhythmicity under variable protein concentrations.

2.2 Introduction

Circadian clocks are intracellular systems that provide organisms with an internal representation of local time and have profound consequences to health and reproductive fitness (*93*). The clock in the cyanobacterium *Synechococcus elongatus* generates circadian rhythms of genetic, physiological, and metabolic activities that enhance fitness (*94, 95*). The core circadian clock genes of cyanobacteria, *kaiA, kaiB,* and *kaiC*, are essential for rhythmic gene expression (*10*), and their proteins generate an autonomous ~24-h rhythm of KaiC phosphorylation *in vivo* (*11*), that can be recapitulated *in vitro (3)*. Ordered phosphorylation of KaiC at residues S431 and T432 (*31, 38*), stimulated by KaiA during the day (*33, 75*) and suppressed by KaiB at night (*96, 97*), helps set the circadian pace and phase of the core oscillator (*35, 40, 43*). The input/output sensor histidine kinases, *Synechococcus* adaptive sensor A, SasA (*98*), and Circadian input kinase A, CikA (*73*), interact with Kai proteins (*43, 74*) to regulate the master transcription factor, RpaA (*57*) and generate circadian rhythms of gene expression in cyanobacteria (*63, 65*).

Although the reconstituted KaiABC oscillator has been a powerful tool to study mechanisms of circadian timekeeping in cyanobacteria (*3, 40, 82, 99, 100*), it does not include the signal transduction machinery necessary to provide a readout of timing encoded by the biochemical oscillator. To explore how each component interacts in the network and how output proteins integrate with the core oscillator, we reconstituted clock-controlled DNA binding in a cell-free system that enables real-time reporting from different partners. In addition to the core oscillator components

KaiA, KaiB and KaiC, this *in vitro* clock (IVC) includes SasA and/or CikA, RpaA and a DNA duplex that carries a clock-controlled promoter, demonstrating that these components are sufficient to form the fundamental regulatory network for autonomous timekeeping and temporal relay to downstream events. We then use this IVC to identify how a loss of function allele in RpaA disrupts circadian rhythms, highlighting its power to provide mechanistic insight for *in vivo* studies. Moreover, through careful deconstruction of our expanded *in vitro* clock, we discovered that SasA helps to cooperatively recruit KaiB to the KaiC hexamer, thus defining a new role for SasA in the core oscillator that it is required for proper circadian rhythms *in vivo*.

2.3 Signal transduction in a reconstituted *in vitro* clock

To monitor protein interactions in the IVC, we attached fluorescent probes (*101*) to each of the individual clock protein components KaiA, KaiB, SasA, CikA, or RpaA using Sortase A-mediated ligation (*102, 103*) and monitored their association into larger complexes using fluorescence polarization anisotropy (FA, **Fig. 2.1A-C**). Fluorescently labeled synthetic dsDNA representing the promoter sequence of the *kaiBC* operon, P*kaiBC*, was used as a representative RpaA target (*65*), and each labeled species was monitored in separate but parallel clock reactions. Control experiments were performed to verify the specific binding events that cause changes

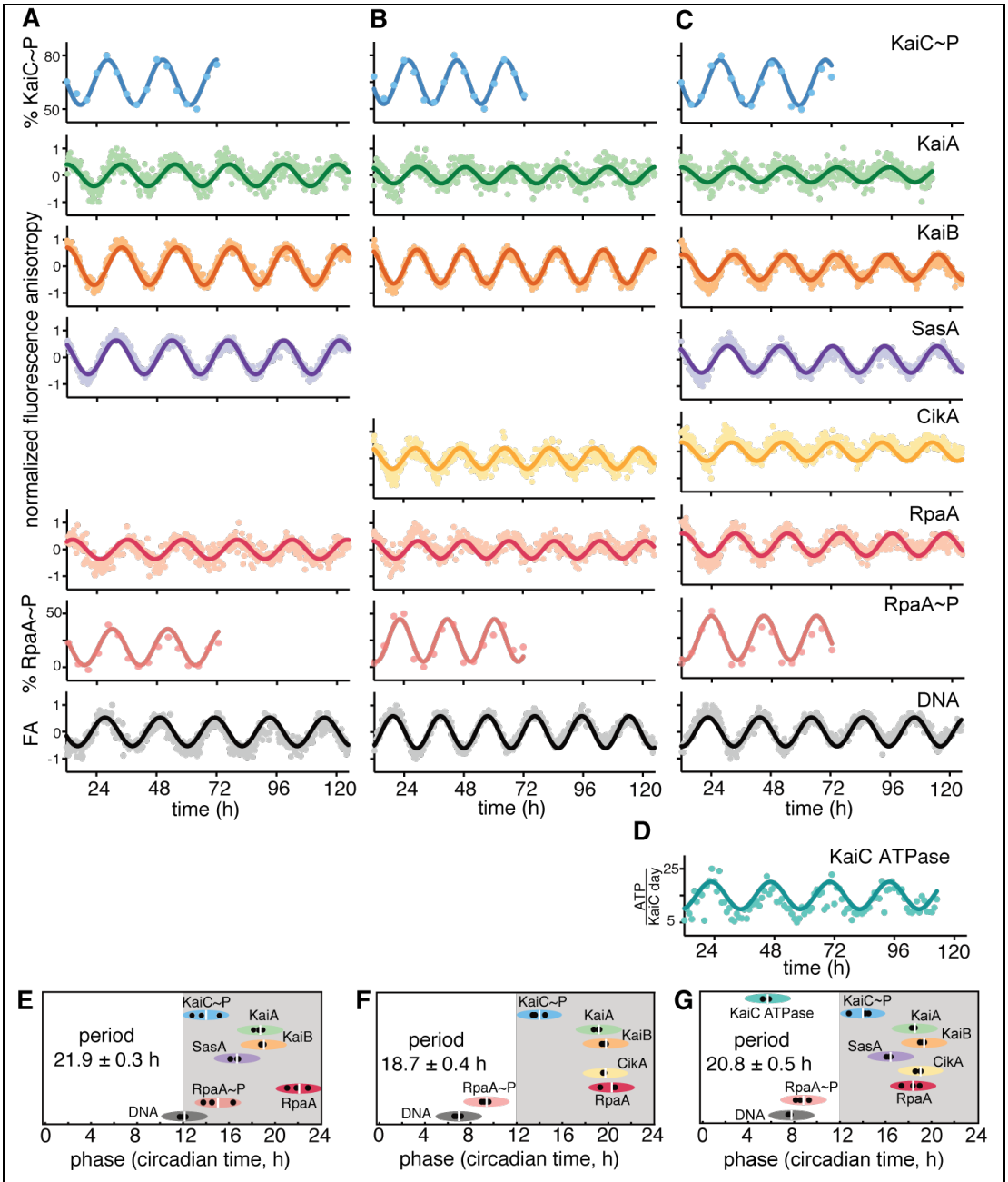

Figure 2.1. Reconstitution of an intact clock that controls rhythmic DNA binding *in vitro*.

A-C) IVC reactions containing KaiA, KaiB, KaiC, RpaA, P*kaiBC* DNA, 1 mM ATP, 5 mM $MgCl_2$, and SasA and/or CikA. 50 nM fluorescently labeled KaiA (green), KaiB (orange), SasA (purple), CikA (yellow), RpaA (red), or 100 nM P*kaiBC* (gray) were included in separate reactions, and their fluorescence anisotropies (FA) were measured in a microplate reader at 30 ºC. For phosphorylation experiments, KaiC~P (blue) and RpaA~P (salmon) were

quantified by gel electrophoresis on SDS-PAGE and Zn^{2+}-Phos-tag^{TM} gels respectively. After truncating the first 12 hours of data collection during which samples approached stable limit cycles, data were baseline-corrected and fit to a damped cosine function to calculate periods and phases (see Materials and Methods). FA values were normalized before fitting. **D)** KaiC-ATPase was measured by real-time ^{1}H-NMR in a KaiABC-only reaction to isolate the KaiC ATPase activity. **E- G**) Relative phases for each component in **A-C,** determined from three separate experiments are shown by black dots with the average denoted by a white vertical line and the peak of KaiC~P is referenced to CT14 (*9*). The width of each ellipse is ±2 h centered at the peak.

in FA of each labeled species (*104*), assigning their corresponding peaks to known interactions and circadian properties.

We used a multimode microplate reader to monitor *in vitro* oscillations in parallel, with individual reactions containing 50-100 nM of a single fluorescently labeled species for each protein or DNA monitored, as well as physiological concentrations (*65*) of each unlabeled clock protein: KaiA, KaiB, KaiC, RpaA, and SasA and/or CikA. This method allows measurement of FA for each clock component in a single plate and in real time over a duration of several days. The data from these experiments were fit to a damped cosine function to extract period and phase relative to maximal KaiC phosphorylation. This was referenced to its peak at circadian time (CT) 14 *in vivo* (*33*), with CT 0 and CT 12 representing subjective dawn and dusk, respectively, under constant lab conditions. Combining FA measurements with traditional time courses of RpaA and KaiC phosphorylation rhythms measured in parallel by gel electrophoresis (**Fig. 1A-C**) (*104*), we now present a comprehensive view of a fully reconstituted *in vitro* clock.

KaiC ATPase activity was monitored in real time by ^{1}H-NMR (**Fig. 2.1D**) (*105*) using the core oscillator to avoid conflation with ATP consumption by the output kinases. During subjective midday, we found that the ATPase activity of KaiC peaks with the hydrolysis of ~13-18 ATPs/KaiC monomer per day but decreases to a nadir of ~7-8 ATPs/KaiC monomer per day during subjective night, consistent with earlier studies (*29*). Using this information, we next established the phase relationships of all the clock components under each IVC condition (**Fig. 2.1E-G**). Notably, we found that the FA of RpaA increased when it was dephosphorylated or interacting with SasA in the absence of KaiC, and that it decreased when RpaA was phosphorylated by CikA or a SasA-KaiC complex (*104*), explaining the observed phase reversal between peak RpaA anisotropy and RpaA phosphorylation.

2.4 Exploring clock output by SasA and CikA

Transcriptional output in cyanobacterial circadian rhythms is based upon the antagonistic activity of two sensor histidine kinases; SasA is a KaiC-dependent kinase that phosphorylates RpaA to stimulate DNA binding and activate gene expression at dusk, while CikA is stimulated to act as a phosphatase that dephosphorylates RpaA when it associates with the Kai complex at night (*8, 57, 63, 73, 98*). To better understand the activities of each sensor histidine kinase in clock output, we first studied the reconstituted clock under conditions where only one was present at a time. In an IVC that contained KaiA, KaiB, KaiC, and SasA alone with RpaA and DNA (**Fig. 2.1A**), the relative phases of the protein interaction rhythms (**Fig. 2.1E**), were

largely consistent with those reported *in vivo* (*31*). For example, FA rhythms of KaiA, KaiB, and SasA peaked from CT 15-22, indicating the formation of large protein complexes during subjective night due to interaction with KaiC. These proteins also form large complexes *in vivo* around Zeitgeber time (ZT) 16-22 (*30*), where ZT 0 and ZT 12 correspond to dawn and dusk under a light-dark cycle. Although SasA and KaiB bind to overlapping sites on KaiC (*50*), we observed that the rhythms of SasA binding to KaiC peak ~3-h earlier than those of KaiB (**Fig. 2.1A and 2.1E**). In principle, this phase difference could provide a temporal window for the KaiC-dependent activation of SasA autophosphorylation (*65*), allowing the phosphoryl transfer from SasA to RpaA (*57*) that is observed around subjective dusk in the IVC (**Fig. 2.1E**). RpaA dephosphorylation in the SasA-only IVC is likely due to a combination of the inherent autophosphatase activity typically seen in response regulators (*106, 107*) and weak phosphatase activity of SasA (*63*).

When SasA was replaced by CikA in the IVC, we still saw circadian rhythms in the interaction of KaiA and KaiB with KaiC in the same relative phase with KaiC phosphorylation (**Figs. 2.1B and 2.1F**), although the period was ~3-h shorter. The FA of CikA peaked in phase with KaiB, consistent with recruitment of the *pseudo*-receiver (PsR) domain of CikA to the KaiB-KaiC complex in the subjective night (*37*). We verified that formation of this complex stimulates the phosphatase activity of CikA towards RpaA and that CikA can act as an RpaA kinase when not associated with the KaiB-KaiC complex (*104*), as previously reported (*36, 63*). The bifunctional switching of CikA between phosphatase and kinase in the IVC likely causes the phase

advance in the rhythms of RpaA phosphorylation and DNA binding relative to the SasA-only IVC by ~5-h (**Fig. 2.1F**). CikA levels *in vivo* are normally low under high intensity light (*23, 104*)**,** suggesting that it may be limited to acting predominantly as a phosphatase at night. However, Δ*sasA* strains generate circadian rhythms in low light (*98*), suggesting that environmental conditions that favor CikA stability can rescue circadian rhythms. We demonstrated robust CikA-dependent circadian rhythms in strains that lack SasA but still express CikA, and in which KaiB and KaiC were boosted to wild-type levels by circumventing autoregulation; notably, these rhythms occurred with a phase advance similar to the CikA-only IVC (*104*). Taken with the observation that Δ*sasA*Δ*cikA* strains are arrhythmic (*64*), these data suggest that the circadian rhythms observed in Δ*sasA* strains arise from a CikA-mediated regulatory circuit on RpaA. When CikA is present constitutively in the IVC, it can drive rhythms of RpaA phosphorylation both in the absence (**Fig. 2.1B)** or presence of SasA (**Fig. 2.1C)** to push the phase of peak DNA binding to midday instead of dusk (**Fig. 2.1F and 2.1G**). Thus, the IVC recapitulates to a reasonable extent the relative *in vivo* phases of the circadian clock of *S. elongatus* and enables aspects of the clock—input (*78, 79*), oscillator (*3*), output (*63-65, 108*) —to be measured under defined conditions with multiple readouts simultaneously in real time, including the phosphorylation-dependent interactions of RpaA (*104*) with a cognate promoter element in DNA.

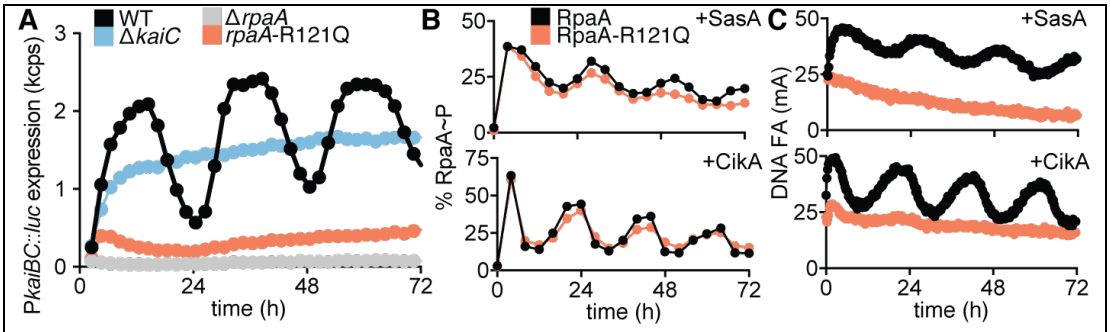

Figure 2.2. The IVC reveals a defect in DNA binding by the RpaA-R121Q mutant.
A) Rhythms of bioluminescence generated by P*kaiBC*::*luc* expression were monitored for entrained wild-type (black), Δ*kaiC* (blue), Δ*rpaA* (gray), and *rpaA*-R121Q (salmon) cyanobacterial strains. Each plot represents an average of six biological replicates. **B)** Rhythms of RpaA phosphorylation or **(C)** FA of P*kaiBC* DNA in IVC reactions containing either SasA or CikA as in **Fig. 2.1A or 2.1B**.

2.5 Leveraging the extended oscillator to study clock mechanisms

Reconstitution of the cyanobacterial clock offers the possibility to ask questions about how downstream signal transduction components are coupled to the KaiABC oscillator to provide deeper mechanistic insight into circadian biology. First, we sought to explore the mechanistic origins of clock disruption in an arrhythmic *S. elongatus* strain that was originally reported as a *crm1* transposon-insertion allele (*109*). However, in addition to disruption of *crm1*, we also noted a single nucleotide polymorphism in the *rpaA* gene located immediately downstream resulting in an R121Q amino acyl substitution in RpaA. When we reconstructed the allele of *rpaA-R121Q* in a wild-type reporter strain by markerless CRISPR-Cas12a editing (*110*), it displayed the same arrhythmic phenotype (**Fig. 2.2A**), demonstrating that mutation of *rpaA*, not *crm1*, disrupted clock function. Despite having a wild-type RpaA phosphorylation pattern (**Fig. 2.2B**), the mutant strain did not produce rhythmic gene

expression (**Fig. 2.2C**). We used the IVC to test the hypothesis that the RpaA-R121Q variant is deficient in DNA binding, even in its phosphorylated form. Although we observed circadian rhythms of FA and phosphorylation (**Figs. 2.2B)** in the mutant that were similar to WT RpaA, the R121Q mutant bound poorly to the P*kaiBC* promoter as indicated by the low amplitude of DNA FA (**Fig. 2.2C**). Thus, the IVC helped to identify the mechanism of clock disruption by the R121Q amino acyl substitution in RpaA — it does not hinder regulatory interactions with SasA or CikA, but instead prevents the phosphorylated sensor domain from regulating its DNA-binding domain.

2.6 Effect of protein concentrations on rhythmicity and period of the clock

The core oscillator has a well-established, albeit relatively narrow, range of concentrations of KaiA, KaiB and KaiC under which sustained biochemical rhythms can be observed *in vitro* (*111*). Using our new fluorescence-based readout, next we measured how rhythms in the core oscillator depend on concentrations of KaiA and KaiB (**Fig. 2.3**). We found a striking convergence with previous studies monitoring rhythms of KaiC phosphorylation by SDS-PAGE (*111*). Because the fluorescence-based oscillator can be monitored non-invasively in 384-well format, we could follow rhythms for many days longer than is practical for the KaiC phosphorylation assay and quantify sensitivity of oscillation amplitude and period to concentrations of the oscillator components. In general, the oscillator functions well with sub-stoichiometric concentrations of KaiA, although the period lengthened as KaiA concentration was decreased (**Fig. 2.3A-C**). By contrast, oscillator period was not

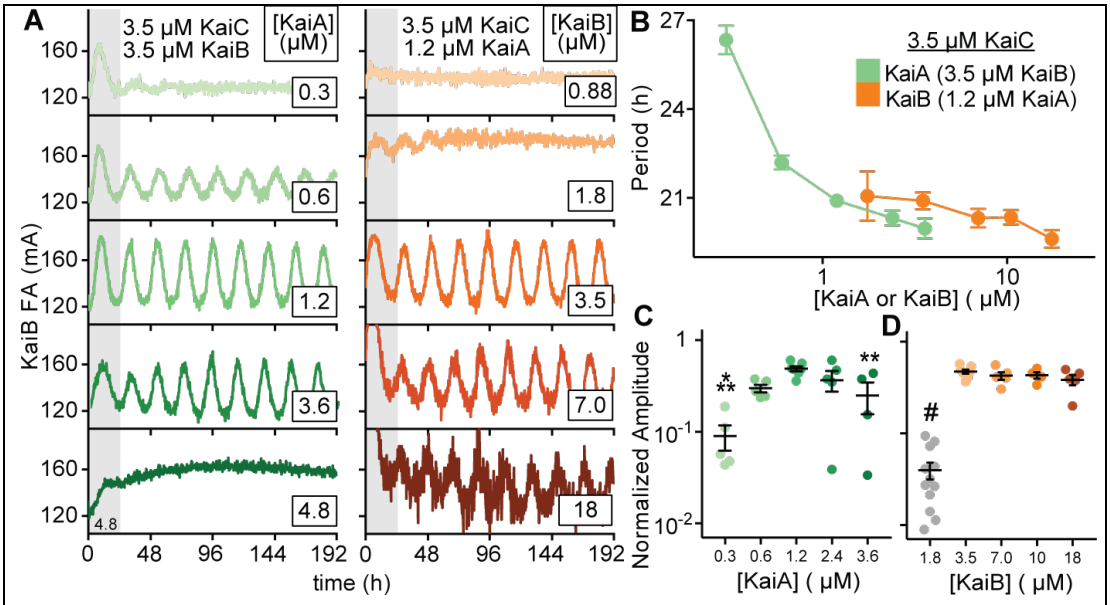

Figure 2.3: Rhythmicity and period of the oscillator depend in different ways on the concentrations of KaiA and KaiB.
A) *In vitro* oscillator reactions containing 3.5 μM KaiC, 3.5 μM KaiB (including 50 nM fluorescently labeled KaiB as a probe) and titrations of KaiA from 0.3-6.0 μM (green scale, left column). Representative assay from n = 3 are shown; the first 24-h of the reactions is shaded gray. Assays were also performed with 3.5 μM KaiC, 1.2 μM KaiA and titrations of KaiB from 0.7-18 μM (orange scale, right panel). FA data were fit to a cosine function to extract period **(B)** and amplitude **(C-D)** as a function of KaiA or KaiB concentration. Amplitudes for KaiB titrations were normalized to account for increasing ratio of unlabeled KaiB to fluorescently labeled probe KaiB. Reactions that did not oscillate were not included. Data are shown as mean ± SD (n ≥ 3). One-way ANOVA with Dunnett's multiple comparisons test was used for comparison between of each suboptimal condition in a with the 1.2 μM KaiA, 3.5 μM KaiB condition: *, $P < 0.05$; **, $P < 0.01$; ***, $P < 0.001$; #, $P < 0.0001$. Where no symbol is shown, differences were determined not to be statistically significant.

affected by titrating KaiB, although there was a clear requirement for KaiB to be present at concentrations equivalent to KaiC (**Fig. 2.3D**). At one-half stoichiometry of KaiB relative to KaiC (1.75 μM KaiB and 3.5 μM KaiC), the oscillator functioned at low amplitude for only a few days with a normal circadian period before significantly

damping to arrhythmicity (**Fig. 2.3A**). As KaiB is found in slight excess over KaiC *in vivo (96, 112)*, it may be essential for the KaiC hexamer to recruit a full stoichiometric complement of six molecules of KaiB to stably sequester KaiA and facilitate the KaiC dephosphorylation phase in subjective night. Consistent with this model, rhythms abruptly diminished as the concentration of KaiA exceeded that of KaiC (**Fig. 2.3A** and (*91, 111*)).

2.7 CikA rescues oscillator period under limiting concentrations of KaiA

Although CikA is primarily considered an input/output protein (*63, 64, 73*), it is known to affect circadian period *in vivo*, and was recently shown to regulate the period of the core oscillator *in vitro* (*36, 113*). We previously determined that the PsR domain of CikA competes for the KaiA binding site on the KaiB-KaiC nighttime complex (*37*). This competition likely underlies period control by CikA; by displacing KaiA from the repressive complex, CikA promotes the activating potential of KaiA to stimulate KaiC phosphorylation (*113*). Using our extended oscillator system, we found that increasing concentrations of CikA led to progressive period shortening, particularly under limiting concentrations of KaiA, bringing it in line with the period found under idealized oscillator conditions (**Fig 2.4A)**. This result demonstrates one way that competitive mechanisms can compensate for fluctuating *in vivo* concentrations of oscillator proteins to influence timekeeping by the cyanobacterial clock.

2.8 SasA rescues oscillations under limiting concentrations of KaiB

SasA was originally described as an amplifier of circadian rhythms needed to maintain robust, high amplitude rhythms, presumably by controlling rhythmic transcription of the *kaiBC* cluster (*98*). In contrast to the effect we observed with CikA, the addition of SasA led to progressive period lengthening (**Fig. 2.4A**). The isolated thioredoxin-like domain of SasA was much less effective at lengthening the period compared to full-length SasA dimer, consistent with the avidity observed in binding studies between KaiC and full-length SasA (*104*). It should be noted that addition of the isolated PsR domain or full-length CikA caused concentration-dependent changes in period length *in vitro* that are apparently balanced out by period changes imparted by SasA (**Fig. 2.4)**. These data support a model in which the proteins that impart output contribute substantively to the timing of the clock through interactions with the Kai proteins.

In exploring the combined effects of KaiB and SasA concentrations on oscillator period, we unexpectedly observed that amplitude and damping in a weak oscillator with suboptimal concentrations of KaiB could be rescued through the addition of SasA (**Figs. 2.4B-D**). To better understand this phenomenon, we set up assays with increasing concentrations of SasA under typical *in vitro* oscillator conditions (*3*) as well as two concentrations where KaiB was limiting relative to KaiC. When KaiB concentrations were too low to support oscillations, we observed low FA values for KaiB, consistent with incomplete recruitment of labeled KaiB to KaiC hexamers (**Fig. 2.4C**, top left column). Addition of SasA up to 1 μM increased

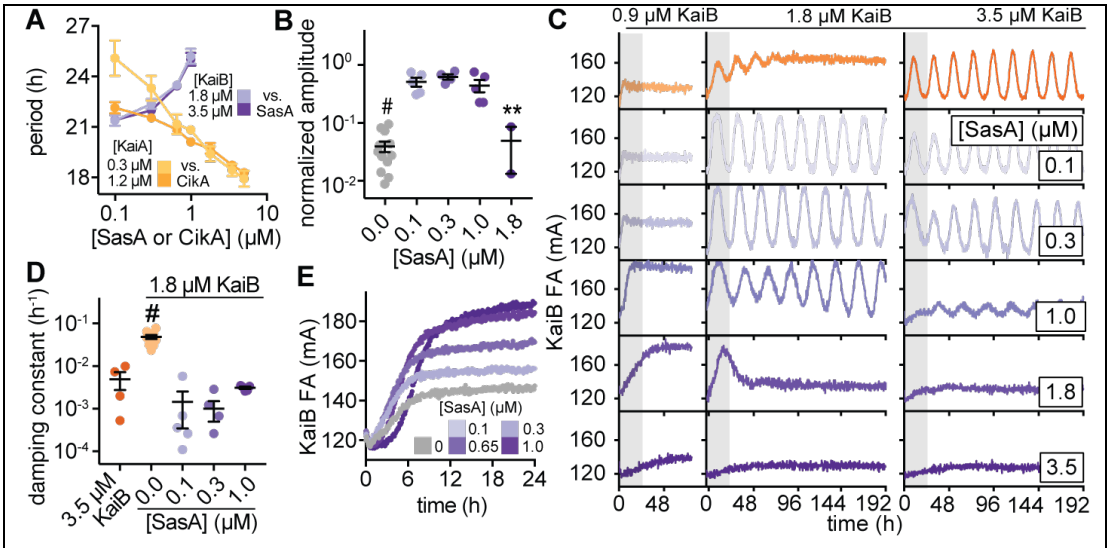

Figure 2.4: Output proteins compensate for period and amplitude defects in suboptimal *in vitro* oscillators.
A) Period of clock reactions with varied concentrations of KaiA (light/dark yellow) or KaiB (light/dark purple) supplemented as a function of CikA or SasA concentration, respectively. **B)** Amplitudes of rhythms with probe KaiB + 1.8 μM unlabeled KaiB in the presence of SasA (gray for KaiB alone; light to dark purple for SasA). Reactions that could not be fit to a sine function because they did not oscillate were not plotted. Statistical analysis was performed exactly as described in **Fig. 2.3C-D**. **C)** *In vitro* oscillator assays with 3.5 μM KaiC, 1.2 μM KaiA, and the indicated concentrations of KaiB as well as various amounts of full-length SasA ranging from 0.1-3.5 μM. Representative assay from n ≥ 3 shown; the first 24-h of the time course is shaded gray. **D)** Damping constants derived from least-squares fitting of the FA data to a damped sine function. **E)** 'Partial oscillator' reactions containing 50 nM KaiB, 3.5 μM KaiC and 1.2 uM KaiA with various amounts of SasA.

KaiB FA, demonstrating that SasA enhances KaiB binding to KaiC. However, as the concentration of SasA approached or exceeded that of KaiC, FA values for KaiB dropped, demonstrating that SasA eventually outcompetes KaiB for binding to the KaiC hexamer as observed before (*50, 55*).

Using a KaiB concentration equal to half that of KaiC, we saw rapidly damping, low amplitude rhythms (**Fig. 2.4C**). Remarkably, we found that addition of sub-stoichiometric amounts of SasA restored full amplitude and eliminated damping of the oscillations (**Fig. 2.4C**, middle column). Increasing SasA concentrations from 0.1 to 1 μM under these conditions did not further influence amplitude, and higher concentrations of SasA attenuated oscillations by outcompeting KaiB for binding to KaiC, as reflected by low anisotropy levels of the labeled KaiB (**Fig. 2.4C**). Under standard oscillator conditions with stoichiometric KaiB and KaiC, the amplitude of oscillation was affected by addition of SasA only at 1.0 μM and higher (**Fig. 2.4B and 2.4C**, right column). The sharp drop in oscillator amplitude and KaiB FA levels demonstrates that a functional switch from recruitment to competition by SasA occurs around ~0.65-1 μM, depending on the exact oscillator conditions. This setpoint is close to the concentration of SasA *in vivo* estimated by quantitative western blotting of around 0.6 μM (*63*).

We hypothesized that SasA expands the range of permissive KaiB concentrations for biochemical oscillation by directly enhancing the interaction of KaiB and KaiC. As a test, we used a partial oscillator experiment in which unlabeled KaiB was omitted from the reaction, and association of the 50 nM labeled KaiB probe was measured as phosphorylated KaiC accumulated upon stimulation by KaiA (**Fig. 2.4E**). We observed a concentration-dependent enhancement in KaiB association as SasA concentration approached the physiological value of ~0.65 μM. This finding suggests that, aside from its role in regulating of transcriptional output from the

oscillator (*98*), SasA also directly modulates KaiBC association to control formation of the nighttime repressive state and stability of the clock itself. Moreover, we observed a delay in KaiB association with KaiC when SasA was present at higher concentrations, consistent with the period lengthening effects observed with SasA in the IVC (**Fig. 2.4A)**.

2.9 Structural mimicry in the KaiC-binding region of SasA and KaiB

During the subjective day when KaiB is free, it exists in a unique ground-state fold, but the fold-switched monomer that binds KaiC at subjective night is thioredoxin-like, which is the same fold adopted by the KaiC-binding domain of SasA ($SasA_{trx}$) (*36*). A high-resolution crystal structure of the sub-complex comprising a single KaiC-CI domain and a fold-switch-locked mutant KaiB I88A from the related thermophilic species, *T. elongatus* (*37*) (I87A in *S. elongatus*, referred to herein as "fsKaiB") illustrates how KaiB docks onto the exposed B-loop of the CI domain (**Fig. 2.5A**). To better understand the relationship between SasA and KaiB recruitment to KaiC, we solved a crystal structure of $SasA_{trx}$ bound to the KaiC-CI domain from *T. elongatus* (**Table 2.1)** to reveal that SasA binds the B-loop in a similar orientation to KaiB (**Fig. 2.5C**). To interrogate the importance of this interface we probed substitutions in several KaiC residues in the B-loop using affinity assays to KaiC hexamer. We performed equilibrium binding assays using the KaiC phosphomimetic mutants KaiC-EE and KaiC-EA, which are widely used to approximate the dusk- like (pS/pT) and nighttime-like phosphoserine (pS/T)

Table 2.1. Refinement statistics for structure determination of KaiC-CI-SasA$_{trx}$ complex.

Data collection	
# crystals used	1
wavelength	1.0 Å
space group	$P2_1$
cell dimensions	
a, *b*, *c* (Å)	107.6, 121.58, 133.59
α, β, γ (º)	90.0, 108.78, 90.0
resolution (Å)	49.05-3.2 (3.30-3.20) *
# total reflections	153257 (13790)
# unique reflections	53267 (4637)
R_{merge}	16.5 (75.7)
R_{pim}	13.0 (57.5)
I/σI	5.5 (1.5)
completeness (%)	98.8 (99.3)
$CC_{1/2}$	0.95 (0.58)
Wilson B-factor	58.3
redundancy	2.9 (3.0)
Refinement	
resolution (Å)	3.20
R_{work}/ R_{free}	22.2/26.6
# atoms	
protein	15469
ligand/ion	30
B-factors	
protein	61.3
ligand/ion	46.1
r.m.s deviations	
bond lengths (Å)	0.003
bond angles (º)	0.78
residues in favored regions (%)	93.1
residues in outlier regions (%)	0.6

*highest resolution shell is shown in parenthesis.

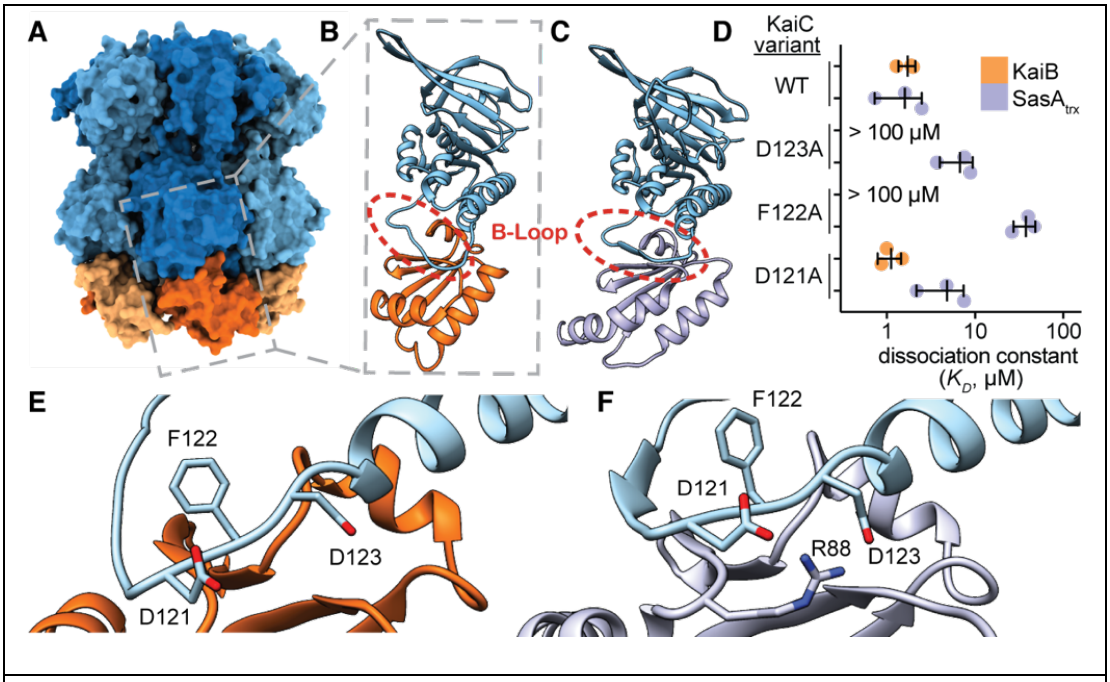

Figure 2.5: SasA and KaiB bind analogously to KaiC.
A) The KaiB-KaiC heterododecamer (PDB:5JWQ) with subunits of KaiC ring depicted in alternating light and dark blue, and fsKaiB subunits in alternating light and dark orange. The gray box indicates the position of the isolated KaiC-CI domain-fsKaiB subcomplex (PDB:5JWO, **B**). **C)** The KaiC-CI domain-SasA$_{trx}$ subcomplex (PDB:6X61), with KaiC (blue), SasA (purple). **D)** Equilibrium dissociation constants (K_D) for KaiB (orange) or SasA$_{trx}$ (purple) binding to KaiC-EE mutants (mean ± SD, n = 3). Where indicated, binding was too weak for curve fitting and K_D is reported as > 100 μM. **E-F)** The interface of KaiC-CI with fsKaiB (**E**) or SasA$_{trx}$ (**F**) with key residues highlighted.

states (*31*). Using these mimetics, we found that KaiB has similar affinity for both states, whereas SasA has a preference for the pS/pT state (**Fig. 2.6A-B**), consistent with prior results (*67*) and its earlier phase of binding in the IVC (**Fig. 2.1A and 2.1E**). Furthermore, although the isolated SasA$_{trx}$ domain is necessary and sufficient for binding to KaiC (*98*), avidity effects in the full-length dimer (**Fig 2.6C-D**) (*70*), enhanced affinity for KaiC-EE by at least two orders of magnitude compared to the isolated, monomeric SasA$_{trx}$ domain (**Fig. 2.6E-F**).

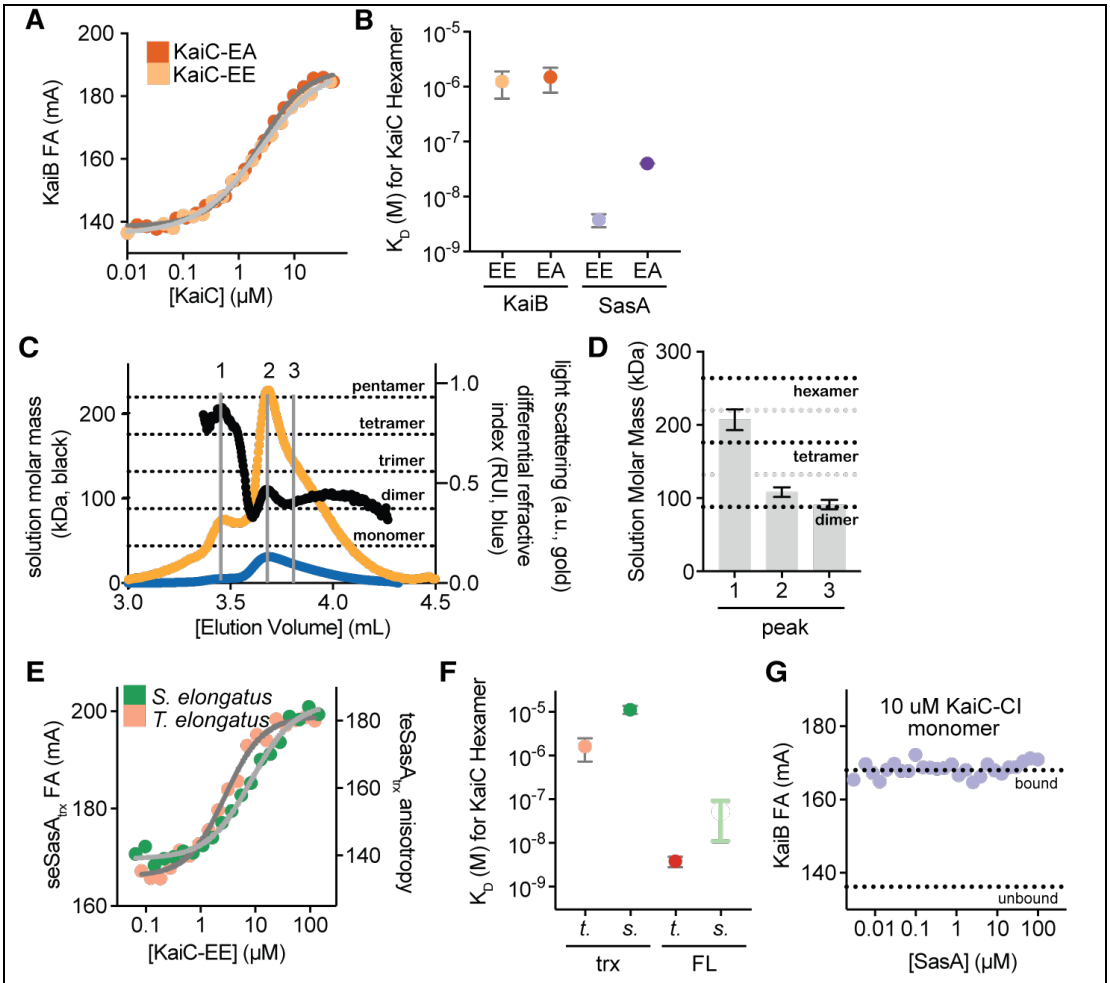

Figure 2.6. Biochemical properties of the SasA-KaiC interaction.
A) KaiB binds to KaiC-EE and KaiC-EA with similar affinity. Representative equilibrium binding assays of 50 nM fluorescently labeled KaiB from *S. elongatus* in the presence of increasing concentrations of *S. elongatus* KaiC-EA (dark orange) and KaiC-EE (light orange). Data were fit to a Langmuir binding isotherm (EA, dark gray; EE, light gray). (**B**) SasA binds KaiC more tightly than does KaiB, with a preference for the pS/pT phosphomimetic, KaiC-EE. Calculated equilibrium dissociation constants (K_D) from binding data in panel **A** (mean ± SD, n = 3; light and dark orange) are compared to affinities from Valencia et al. (*31*) (mean ± SD, K_D measured by SPR; light and dark purple) for full-length SasA from *T. elongatus*. (**C**) Full-length SasA exists primarily a dimer in solution. Traces from a representative size-exclusion chromatography coupled to multiangle light scattering (SEC-MALS) run for full-length SasA from *S. elongatus*. Differential refractive index (blue) is depicted with light scattering (gold) and absolute mass estimation (kDa, black line). (**D**) Quantitative mass analysis of peaks indicated at the top of panel **C** (peaks 1-3) analyzed from triplicate SEC-MALS runs are

consistent with a dimer-tetramer equilibrium (mean mass in kDa ± SD). Calculated masses for dimer, tetramer and hexamer are represented by black dotted lines. (**E**) The $SasA_{trx}$ domain of *T. elongatus* binds with higher affinity than the *S. elongatus* $SasA_{trx}$ domain to the respective KaiC-EE variant from each organism. Equilibrium binding assays of fluorescently labeled $SasA_{trx}$ from *S. elongatus* (dark green) or *T.* (pink) *elongatus*. Data were fit as in panel **A**. (**F**) Full-length SasA (FL) binds much more tightly than the isolated $SasA_{trx}$ domain (trx), suggesting that it relies on avidity for efficient binding to KaiC hexamer. Calculated K_D values extracted from data in panel **E** (mean ± SD, n = 3; pink or dark green) are compared to affinities from Valencia et al. (*31*) (mean ± SD, measured by SPR; red) for full-length SasA from *T. elongatus*. The affinity range of *S. elongatus* SasA calculated from the 2D titration data and our thermodynamic model (**Fig. 6**) is represented as a light green bar. (**G**) Full-length SasA does not display avidity and compete KaiB off of the KaiC-C1 monomer. Fluorescently labeled KaiB was bound to 10 μM monomeric KaiC-CI domain and subsequently titrated with full-length SasA as indicated. Anisotropy values for bound and unbound KaiB (dashed lines) were determined from curve fits in **Fig. 2.6A**.

Comparing the KaiB and SasA binding interfaces on KaiC, we found that substitutions at sites conserved between *S. elongatus* and *T. elongatus* (KaiC F122 and D123) decrease affinity for both KaiB and $SasA_{trx}$ (**Figs. 2.5D, 2.5F**). We then examined how differences in the structures of KaiB and SasA or their orientations on the B-loop might influence binding to adjacent subunits of the KaiC hexamer (**Fig. 2.7**). Small changes in the length and orientation of the C-terminal helix between the $SasA_{trx}$ and KaiB could lead to steric clashes of $SasA_{trx}$ with a neighboring subunit (**Fig. 2.7F-H**). Consistent with this idea, saturation binding experiments showed that $SasA_{trx}$ domains cannot fully occupy all six binding sites on the KaiC hexamer (**Fig. 2.7I**).

2.10 SasA enhances KaiBC interaction through heterotropic cooperativity

Six monomers of the active, thioredoxin-like form of KaiB assemble onto the KaiC hexamer of *S. elongatus* (*37, 51*) to nucleate formation of the nighttime repressive state. Native mass spectrometry and electron paramegnetic resonance analyses demonstrated that KaiB binds to the KaiC hexamer with positive homotropic cooperativity (*56, 70, 100*). Given the similarity between the SasA-KaiC and KaiB-KaiC interactions, we speculated that SasA could facilitate KaiB-KaiC interactions through positive heterotropic cooperativity. We developed an assay to test directly for cooperativity by monitoring 50 nM fluorescently labeled KaiB probe with KaiC-EE using unlabeled SasA or fsKaiB as a secondary titrant (**Fig. 2.8A**). While these assay conditions do not assess the degree of homotropic cooperativity for KaiC-EE with the KaiB probe alone, we found that low concentrations (50-100 nM) of SasA or fsKaiB significantly increased binding of KaiB probe, demonstrating more efficient recruitment to the KaiC hexamer. Higher concentrations of SasA or fsKaiB resulted in competition with the probe, reducing its binding to the KaiC hexamer; an equivalence point was reached when concentration of KaiC-EE matched that of the competitor. We observed a significant overshoot of KaiB probe anisotropy values around this point, consistent with formation of a higher molecular weight complex

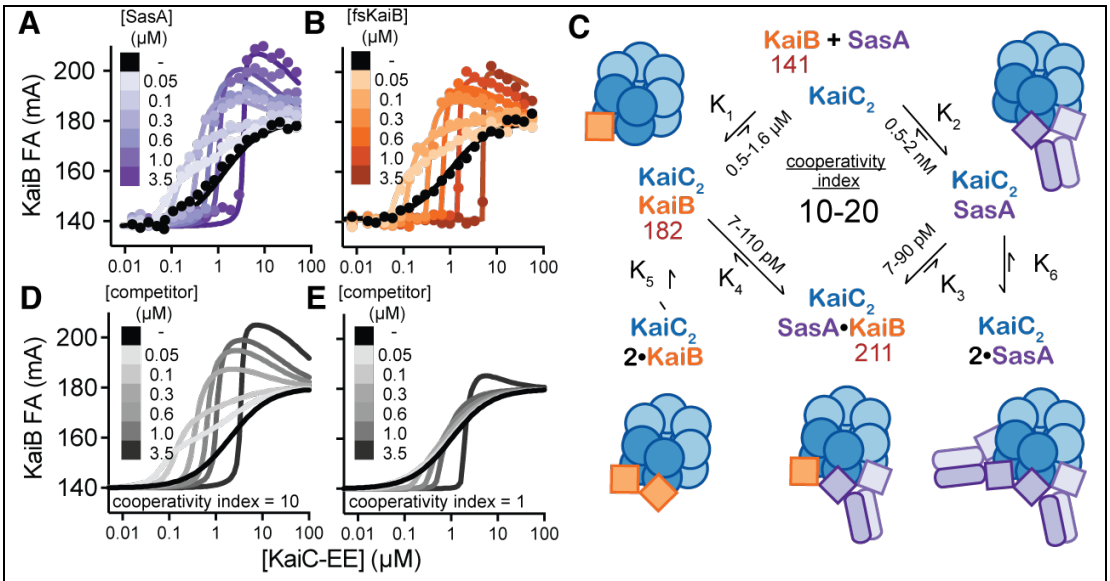

Figure 2.8: The thioredoxin-like fold of SasA and fsKaiB cooperatively recruits KaiB to the KaiC hexamer.
A) Equilibrium binding assays of fluorescently labeled KaiB with KaiC-EE in the absence (black) or presence of unlabeled SasA (light to dark purple) or fsKaiB (**B**, light to dark orange). Each 2D titration is shown from representative assays with best fit lines from global curve-fitting. **C**) Summary of two-site thermodynamic model for SasA heterocooperativity, and mean equilibrium constants derived from least squares fitting of SasA 2D titration assays (n = 3); values in red color are mean peak anisotropy values observed from fitting of all SasA 2D titration datasets using DynaFit software. The cooperativity index is defined as the ratio $K_1/K_3 = K_2/K_4$. This model was used to generate simulated 2D titrations with a cooperativity index of either **D**) 10 or **E**) 1.

consisting of both KaiB probe and SasA bound to the KaiC hexamer. Association of the KaiB probe to the WT KaiC-CI monomer was not significantly affected by the addition of 300 nM SasA or fsKaiB (**Fig. 2.9A**), nor did SasA interact directly with KaiB in the absence of KaiC, demonstrating that these competitors only enhance KaiB association in the context of the KaiC hexamer, as shown using phosphomimetics, consistent with our cooperativity model.

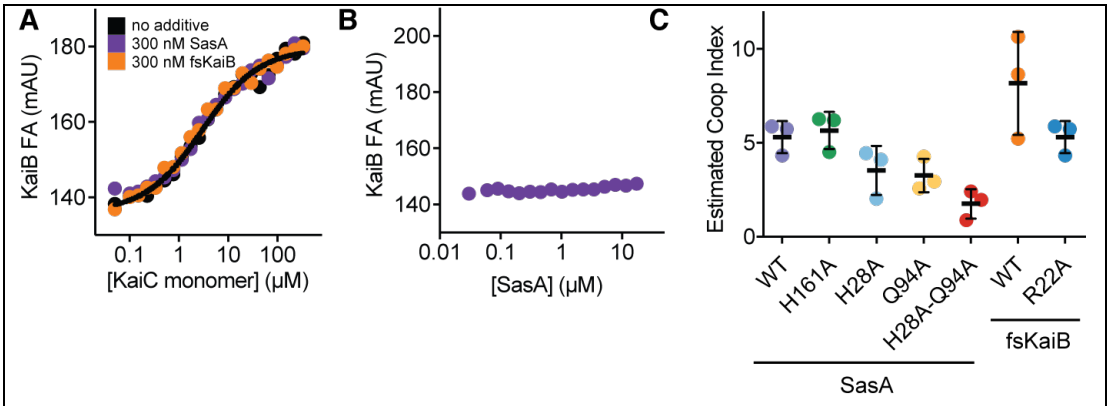

Figure 2.9: Validation of heterocooperative association model of KaiBC association.
A) SasA and fsKaiB additives do not affect binding of 50 nM fluorescently labeled KaiB to KaiC-CI monomer. Equilibrium binding titration of fluorescently labeled KaiB with *S. elongatus* KaiC-CI monomer (black) in the presence of 300 nM fsKaiB (orange) or full-length SasA (purple). (**B**) KaiC is required for KaiB-SasA interactions. Equilibrium titration of fluorescently labeled KaiB with full-length SasA (purple), showing that KaiB anisotropy is unaffected without KaiC present. (**C**) Comparison of estimated cooperativity indices (n = 3, ± SD) of various SasA and fsKaiB variants.

To quantitatively represent the heterotropic cooperativity observed in these 2-dimensional (2D) titrations, a simplified two-site thermodynamic model was found by least squares fitting to be sufficient to account for the data (**Fig. 2.8C**). Within this model, we defined the heterotropic 'cooperativity index' as the fold-increase in KaiB affinity given by the ratio of equilibrium constants K_1/K_3 (= K_2/K_4). Comparison of two-dimensional titrations with SasA or fsKaiB to simulated data representing heterotropic cooperative binding (**Fig. 2.8A-B**), to a model with competition and no cooperativity (**Fig. 2.8D-E**), demonstrates that SasA and fsKaiB similarly influence cooperative recruitment of the KaiB probe on KaiC.

To explore the role of intermolecular KaiB-KaiB interactions in cooperative KaiB-KaiC binding, we characterized KaiB-R22A, a mutant originally identified in *Anabaena* (*114*) that reduces the apparent affinity of KaiB for KaiC although it is not located at the KaiB-KaiC interface (*37*). R22 has been implicated in KaiB cooperativity using native mass-spectrometry (*70*), and is situated at the KaiB-KaiB interface in the KaiBC hexamer structure. We tested this mutant in our cooperativity assay and observed a small decrease in the cooperative recruitment of the KaiB probe relative to that of fsKaiB (**Fig. 2.9C**), demonstrating that inter-subunit KaiB-KaiB interactions have a role in the cooperative recruitment process, and opening the possibility that mutations at the SasA-KaiB interface could also disrupt cooperativity.

2.11 SasA-KaiB complementarity is required for proper circadian timing

To identify whether the enhancement of KaiBC association is important for the function of SasA *in vivo*, we set out to identify point mutations that would separate the cooperativity and output signaling functions of SasA. Toward this end, we first showed that the catalytically-inactive SasA mutant H161A (*67*) is as effective as wild-type SasA in stimulating cooperative recruitment of KaiB to KaiC *in vitro* (**Fig. 2.9C**). Next, we constructed a structural model by overlaying crystal structures of $SasA_{trx}$-CI and KaiB-CI onto the lower resolution structure of the full-length KaiBC hexamer complex (*37*), and used it to predict potential $SasA_{trx}$-KaiB interactions along the clockwise (CW) and counterclockwise (CCW) interfaces of the hybrid complex (**Fig. 2.10A**). Within this framework, we investigated a number of SasA

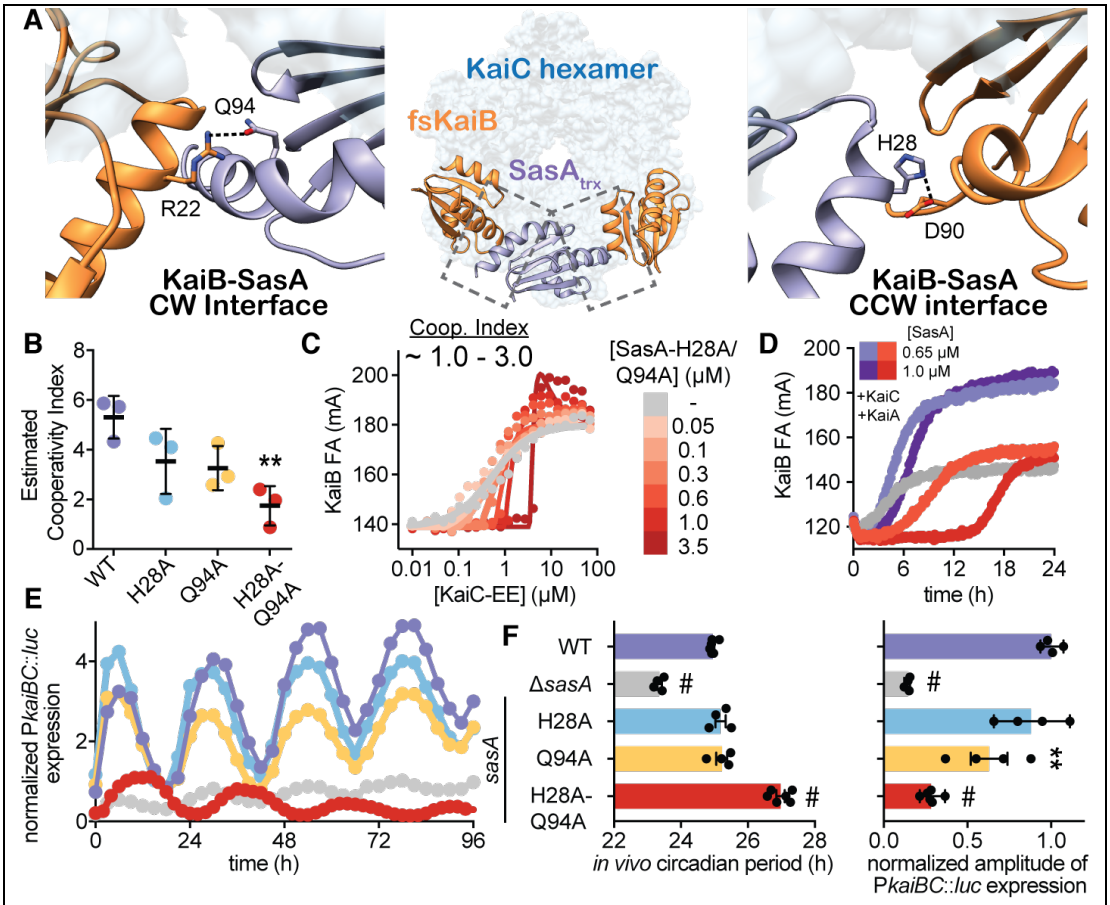

Figure 2.10: SasA-KaiB interactions mediate cooperative recruitment of KaiB *in vitro* and sustain robust circadian rhythms *in vivo*.
A) Structural model of KaiB:SasA interactions on KaiC using KaiC-CI subcomplexes with fsKaiB (orange, PDB:5JWO) and $SasA_{trx}$ (purple, PDB:6X61) modeled onto adjacent subunits of KaiC (light blue) of the KaiBC heterododecamer (PDB:5JWQ). Key residues at clockwise (CW) and counterclockwise (CCW) interfaces are modeled as *S. elongatus* variants based on the alignment in **Fig. 2.11**. Polar contacts predicted by our hybrid structural model are indicated by dashed lines. **B**) Cooperativity indices for SasA variants extracted from KaiC titrations done in the presence of 0.3 μM SasA (mean SD, n = 3). Statistical significance of differences between wild-type and mutant SasA variants was tested using one-way ANOVA with Dunnett's multiple comparisons as described in **Fig. 2.3**. **C**) Representative 2D titration of fluorescently labeled KaiB with KaiC-EE in the absence (gray) or presence (light to dark red) of SasA-H28A-Q94A. **D)** Time-dependent FA trajectories of 50 nM KaiB in the presence of 3.5 μM KaiC and 1.2 uM KaiA with 0.65 or 1.0 μM SasA wild-type (purple shades) or H28A-Q94A mutant (red shades). **E**) Representative time course of bioluminescence driven by P*kaiBC* from *S. elongatus* cultures entrained under 12-h LD cycles for 48-h and subsequently allowed to free run in LL. **F)** Raw luminescence curves were fit to a

sine function to extract amplitude of P*kaiBC*::*luc* expression as well as free running circadian period for each strain. Wild-type control was included for each experiment, and the luminescence of each mutant was normalized to the amplitude of luminescence oscillation for the wild-type control in that run. Error bars depict SEM among replicate cultures (n = 4-6); when error bars are not visible, they were smaller than could be depicted. Symbols indicate significance determined from one-way ANOVA with Dunnett's multiple comparisons between mutant and wild-type *S. elongatus* with symbols to depict significance as summarized in **Fig. 2.3** legend. Normal distribution was confirmed through quantile-quantile plots showing predicted vs. actual residual values in addition to Anderson-Darling, D'Agostino-Pearson omnibus, and Shapiro-Wilk tests, which were all performed in GraphPad PRISM. Equal variance of the data was verified with Brown-Forsythe tests yielding P values above 0.05. Color scheme for data in **E)** is consistent with and indicated on left vertical axis of **F).**

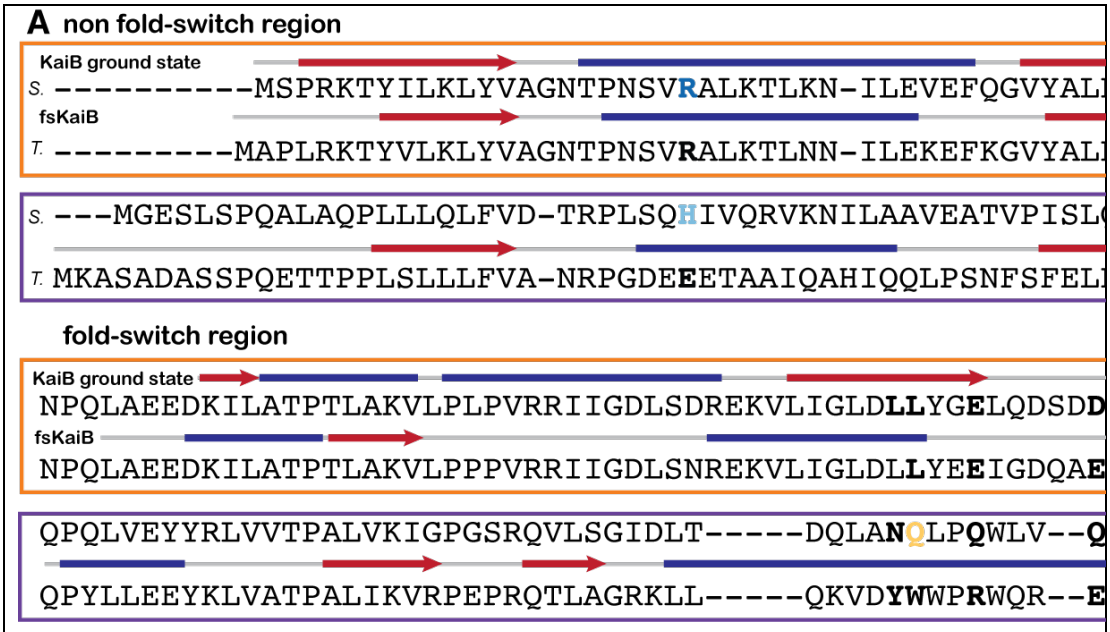

Figure 2.11. Multiple sequence alignment of KaiB and SasA$_{trx}$ from S. and T. elongatus.
A) Multiple sequence alignment of N-terminal (non-fold-switch) and C-terminal (fold-switch) halves of KaiB (orange box) and the structurally analogous SasA$_{trx}$ (purple box) from *S. elongatus* and *T. elongatus*. Red arrows (β-sheets) and blue lines (α-helices) indicate secondary structure from the KaiB tetramer (PDB: 2QKE), fsKaiB monomer (PDB: 5JWO) and SasA$_{trx}$ from the KaiC-CI-SasA$_{trx}$ structure (PDB: 6X61) reported here. Mutations tested in this study are depicted in bold.

substitutions near the CW and CCW interface and estimated their ability to cooperatively recruit KaiB in simplified 2D titration assays comparing as single SasA concentration to the no SasA control. The individual mutants H28A (CCW interface) or Q94A (CW interface) showed decreases in their cooperativity indices that were further decreased in the H28A-Q94A double mutant (**Fig. 2.10B**). It should be noted that the estimates of cooperativity in wild-type were slightly lower than those determined in the full 2D titrations (**Fig. 2.8A** and **2.8C**), likely due to differences in experimental setup. While the H28A-Q94A double mutant did not strongly affect other SasA functions *in vitro*, such as KaiC association and the KaiC-dependent phosphotransfer to RpaA (**Fig. 2.12A-B**), it lacked the ability to stimulate KaiB binding in the 2D titration assay (compare **Fig. 2.10C** and **2.9E**) demonstrating that complementarity on either the CW or CCW interfaces is required for SasA to impart heterotropic cooperativity in KaiB association.

To better understand these mutations in a more native context, we tested the ability of the H28A-Q94A variant to nucleate formation of the repressive complex using a partial oscillator experiment to directly measure the kinetics of KaiBC formation under limiting concentrations of KaiB with WT or H28A/Q94A SasA. (**Fig. 2.10D, 2.12C**). Strikingly, enhancement of KaiB recruitment was essentially non-existent with the SasA H28A-Q94A mutant, instead showing a lengthened competitive phase that occurs even at physiological concentrations of SasA. When concentration of the double mutant was increased beyond physiological levels, the delay in KaiB association became even more exaggerated, demonstrating that

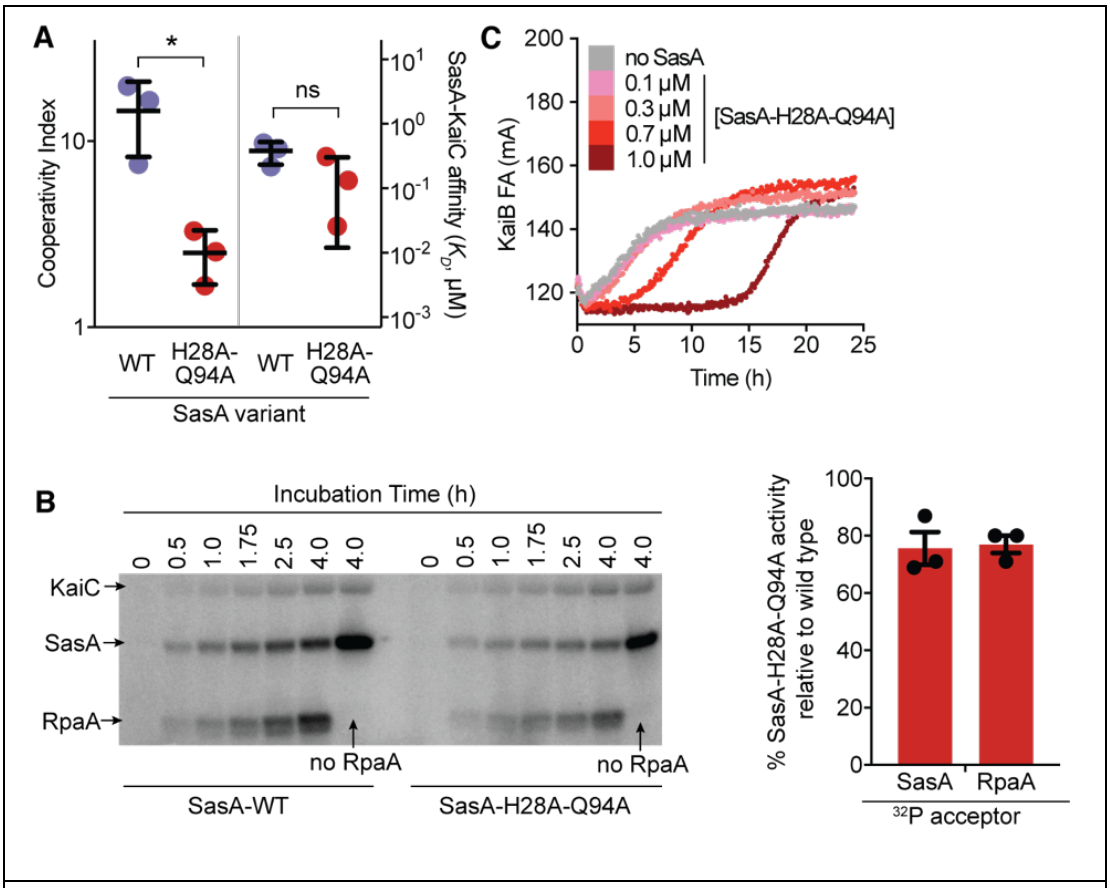

Figure 2.12. Biochemical characterization of various functions of the SasA-H28A-Q94A double mutant.

A) Cooperativity index and KaiC affinity for wild-type SasA (purple dots) and SasA-H28A-Q94A double mutant (red dots) see Data S7. (**B**) Kinase assays were performed in the presence of γ-32P ATP as originally described in Takai *et. al* (*57*). These experiments were conducted with 5 μM KaiC-EE, 3.5 μM RpaA, and 2.5 μM SasA variant in 0.1 mM ATP. SasA-WT and SasA-H28A-Q94A were compared, tracking incorporation of ^{32}P into the proteins by SDS-PAGE and quantifying the result densitometrically. Slopes of the densitometry trajectories were compared in triplicate to estimate activity of the double mutant on RpaA as 77 ± 5% (mean ± standard deviation). A no-RpaA control was included to quantify the efficiency of initial histidine phosphorylation in the SasA variants, and triplicate densitometries were compared at a single timepoint, with SasA-H28A-Q94A autophosphorylation 76 ± 10% as efficient as wild-type. (**C**) Representative trajectory of SasA-H28A-Q94A, titrated in the presence of 50 nM labeled KaiB probe as well as 3.5 μM KaiC and 1.2 μM KaiA (as shown for wild type in **Fig. 2.4E)**. SasA-H28A-Q94A were added here at a range of physiological and sub-physiological concentrations showing ~2-5 h delay in KaiB binding in presence of SasA-H28A-Q94A as compared to WT SasA.

complementarity between the SasA-KaiB interfaces is critical for timely replacement of SasA with KaiB on the Kai hexamer.

With this separation of function mutant in hand, we next set out to test whether the SasA-induced cooperativity we observed for the expanded oscillator *in vitro* could influence circadian rhythms *in vivo*. We introduced the double mutation, as well as several single alanine substitutions, into SasA using markerless CRISPR-Cas12a and monitored bioluminescence from a P*kaiBC* luciferase reporter in constant light (LL) after synchronization in 12-h light:12-h dark cycles (**Figs. 2.10F** and **2.13**). Small effects on amplitude were seen with the individual H28 or Q94 alanine substitutions on their own, but when these were combined in the H28A-Q94A mutant, the amplitude of circadian rhythms decreased to an extent that was similar to the SasA knockout strain (Δ*sasA*, **Fig. 2.10F**), even though the mutant proteins were expressed to a similar level *in vivo* (**Fig. 2.13D**), and the double mutant strain exhibited an~2-h longer period (**Fig. 2.10F** and **2.13**). Taken together, these results provide a clear link between loss of complementarity at SasA-KaiB interfaces and the long-period phenotype observed *in vivo*, further supporting our conclusion that cooperative interactions between SasA and KaiB are crucial for proper circadian timing.

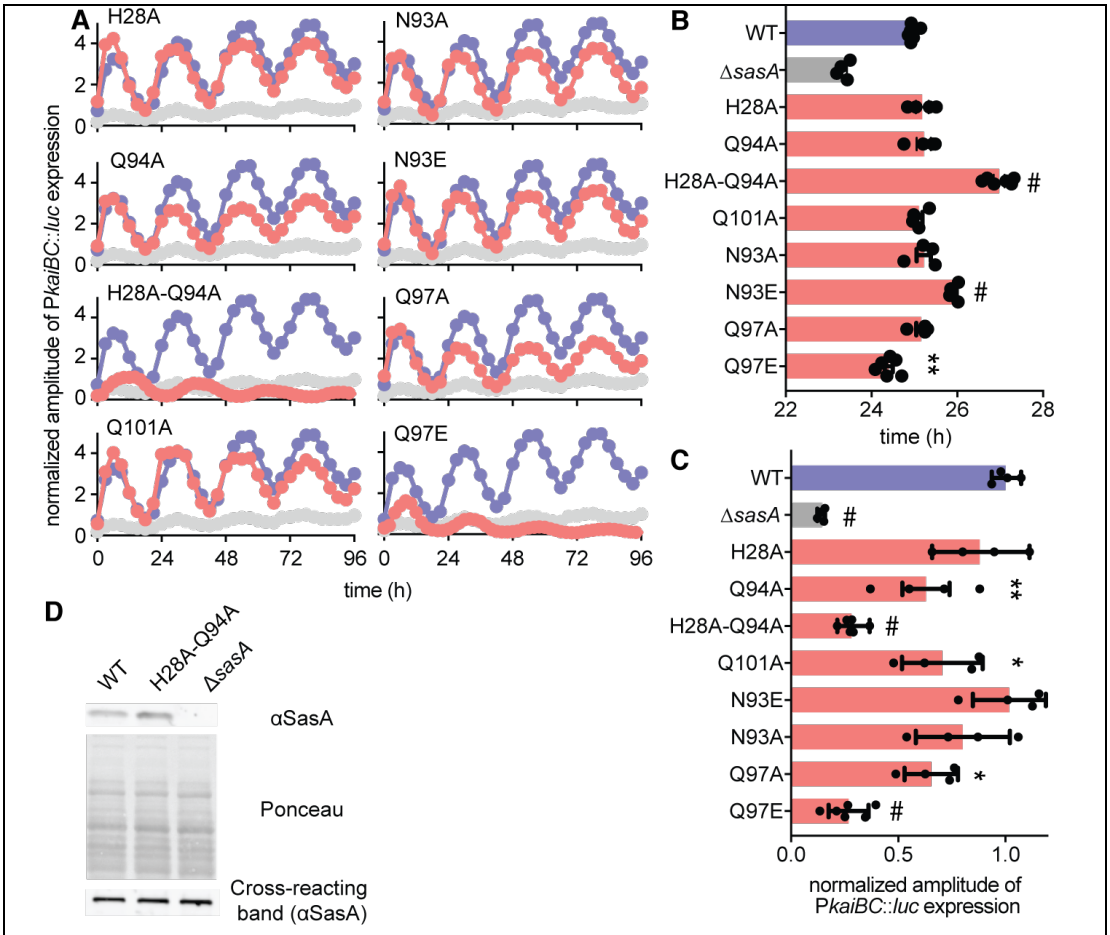

Figure 2.13. Mutations at the SasA-KaiB cooperativity interface alter circadian rhythms in S. elongatus.

A) Bioluminescence traces produced by *S. elongatus* strains based on expression of firefly luciferase driven by the clock-controlled *kaiBC* promoter. Wild type (WT) and Δ*sasA* strains are compared to markerless CRISPR/Cas12a-edited *sasA* mutants, with the relevant amino acid substitutions indicated. Graphs display the averages of 6-12 wells, with standard deviation omitted for better visibility of multiple traces. WT (purple) and mutants, salmon. **B)** Analysis of raw bioluminescence data was performed using BioDare2 to calculate the signal amplitude (in arbitrary units, a.u.) and **C**) period length, with the average and standard deviation reported for 6-12 replicates. One-way ANOVA was performed to identify significant changes (*, $P < 0.05$; **, $P < 0.01$; #, $P < 0.0001$) in amplitude and period length relative to wild type. **D)** Western blot showing similar expression levels of SasA at CT 24 in WT and *sasA*-H28A-Q94A double mutant strains. The cross-reacting band shown at the bottom serves as loading control.

2.12 Discussion

This extended *in vitro* clock is an autonomously oscillating system that remains phase coherent for several days without user intervention, allows real-time observation of rhythmic behaviors of several clock components in parallel, and rhythmically activates the interaction of a transcription factor with a promoter element on DNA. Complementing this assay with parallel measurements of phosphorylation and ATPase activities rounds out a moving picture of an intact cyanobacterial clock. As implemented here, the IVC has revealed a set of minimal components to execute clock-controlled gene expression, helped decouple the mechanistic origins of a clock-disrupting mutant, and provided insight into mechanisms behind the narrow stoichiometric ratios that are tolerated in the *in vitro* oscillator (*111*). In particular, our data demonstrate that SasA, previously regarded solely as an output protein, plays a critical role in the enhancing the oscillator amplitude through heterocooperative regulation of KaiB association with KaiC. This new *in vitro* clock system offers an unparalleled opportunity to explore how the clock maintains consistency *in vivo* despite rhythmic changes in the concentration of clock components that result from the associated transcription-translation feedback (*96, 115*) and protein turnover (*116, 117*), and provides an experimental platform for integrating the oscillator with the upstream and downstream components with which it interacts. By reconstructing, and subsequently deconstructing this elegant system, we have shown that a dichotomous view of timekeeping and signaling components

provides an insufficient representation of the complexity and synergy that has evolved in this ancient circadian clock.

2.13 Materials and Methods

Cloning, expression and purification of proteins

PCR-mediated mutagenesis was performed on the pET-28b vector utilizing Nde I/Hind III restriction sites as described previously (*43*) to modify clock genes from *Synechococcus elongatus* to produce 6x-His-SUMO fusion proteins in *Escherichia coli* BL21(DE3) (Agilent). All constructs are listed in **Table 2.2**. Point mutations were introduced using long-range PCR with overlapping primers (*118*). A single colony from freshly transformed cells was used for inoculation of a starter culture grown in LB medium supplemented with 50 µg/mL kanamycin sulphate at 37 ºC, 220 rpm. After 6.5 h a 5 mL starter culture was transferred to 1 L M9 medium supplemented with 0.2% D-glucose, 2 mM $MgSO_4$, 0.1 mM $CaCl_2$, and 50 µg/mL kanamycin sulfate. Cells were grown to $OD_{600} \approx 0.6$ at 37 ºC before inducing expression by addition of 0.2 mM isopropyl β-d-1-thiogalactopyranoside (IPTG) and incubating cells at 30 ºC for 12 h, except for CikA expression for which cells were incubated at 20 ºC for 22 h.

Cells were harvested and lysed using an Avestin C3 Emulsiflex homogenizer (Avestin Inc, Canada). Cell lysate was clarified by high-speed centrifugation before affinity purification on Ni-NTA resin (QIAGEN) in polypropylene gravity columns using the buffers specified in **Table 2.3**.

Table 2.2: Constructs and shorthand names used in this study.

Shorthand name	***organism***	***Protein full name***
KaiC	*S. elongatus*	FLAG-seKaiC-1-519
KaiC-AA		FLAG-seKaiC-1-519-S431A-T432A
KaiC-AE		FLAG-seKaiC-1-519-S431A-T432E
KaiC-EE		FLAG-seKaiC-1-519-S431E-T432E
KaiC-EA		FLAG-seKaiC-1-519-S431E-T432A
KaiC-CI monomer		FLAG-seKaiC-16-246-R40A-K172A
KaiC-EE	*T. elongatus*	FLAG-teKaiC-1-518-S431E-T432E
KaiC-EE-D121A		FLAG-teKaiC-1-518-D121A-S431E-T432E
KaiC-EE-F122A		FLAG-teKaiC-1-518-F122A-S431E-T432E
KaiC-EE-D123A		FLAG-teKaiC-1-518-D123A-S431E-T432E
KaiC-CI monomer		FLAG-teKaiC-17-247-R41A-K173A
KaiB	*S. elongatus*	seKaiB-1-102-FLAG
G-KaiB		Gly-seKaiB-1-102-FLAG
KaiB-K25C-6IAF		sekaiB-1-102-K25C-FLAG-6-iodoacetamido-fluorescein
fsKaiB		seKaiB-1-99-Y7A-I87A-Y93A-FLAG
fsKaiB-R22A		seKaiB-1-99-Y7A-R22A-I87A-Y93A-FLAG
KaiA		seKaiA-1-284
G-KaiA		Gly-seKaiA-1-284
SasA		seSasA-1-387
G-SasA		Gly-seSasA-1-387
G-SasA-H161A		Gly-seSasA-1-387-H161A
SasA		seSasA-1-387-FLAG
SasA-H161A		seSasA-1-387-H161A-FLAG
SasA-H28A		seSasA-1-387-H28A-FLAG
SasA-Q94A		seSasA-1-387-Q94A-FLAG
SasA-H28A-Q94A		seSasA-1-387-H28A-Q94A-FLAG
$SasA_{trx}$-Q31C*		FLAG-seSasA-13-103-P13A-FLAG
		FLAG-seSasA-13-103-P13A-Q31C-FLAG
$SasA_{trx}$	*T. elongatus*	FLAG-teSasA-16-107-P16A-FLAG
$SasA_{trx}$-A35C*		FLAG-teSasA-16-107-P16A-A35C-FLAG
CikA	*S. elongatus*	FLAG-seCikA-1-754
CikA-LPTEGG-6IAF		FLAG-seCikA-1-754-LPET-GGGYC*(-6IAF)-N

CikA-H393A		FLAG-seCikA-1-754-H393A
CikA		FLAG-seCikA-1-754
$CikA_{psr}$		seCikA-S605-606-745-C644S-C686S-C742S
$CikA_{psr}$-S727C*		seCikA-S605-606-745-C644S-C686S-C742S-S727C
RpaA		seRpaA-1-249
GGG-RpaA		Gly_3-seRpaA-1-249
RpaA-R121Q		seRpaA-1-249-R121Q
G-RpaA-R121Q		Gly_3-seRpaA-1-249-R121Q

* single cysteine residue for labeling with 6-iodoacetamido-fluorescein

Table 2.3: Protein expression and purification conditions

Protein construct	Expression temperature and duration	Ni-NTA Loading buffer	Ni-NTA Wash buffer	Ni-NTA Elution buffer	Gel Filtration Column and Elution Buffer
G-KaiA	30 ºC, 12 h	50 mM NaH_2PO_4, 500 mM NaCl, pH 8	50 mM NaH_2PO_4, 500 mM NaCl, 20 mM imidazole pH 8	50 mM NaH_2PO_4, 500 mM NaCl, 250 mM imidazole pH 8	Superdex-200-1660-pg 20 mM Tris, 150 mM NaCl, 5 mM $MgCl_2$, 1 mM ATP, pH 8
G-KaiB-FLAG	30 ºC, 12 h	50 mM NaH_2PO_4, 500 mM NaCl, pH 8	50 mM NaH_2PO_4, 500 mM NaCl, 20 mM imidazole pH 8	50 mM NaH_2PO_4, 500 mM NaCl, 250 mM imidazole pH 8	Superdex-75-1660-pg 20 mM Tris, 150 mM NaCl, 5 mM $MgCl_2$, 1 mM ATP, pH 8
FLAG-KaiC	30 ºC, 12 h	50 mM NaH_2PO_4, 500 mM NaCl, pH 8	50 mM NaH_2PO_4, 500 mM NaCl, 80 mM imidazole pH 8	50 mM NaH_2PO_4, 500 mM NaCl, 250 mM imidazole pH 8	Superdex-200-1660-pg 20 mM Tris, 150 mM NaCl, 5 mM $MgCl_2$, 1 mM ATP, pH 8

FLAG-KaiC-AA (S431A, T432A)	30 ºC, 12 h	50 mM NaH_2PO_4, 500 mM NaCl, pH 8	50 mM NaH_2PO_4, 500 mM NaCl, 80 mM imidazole pH 8	50 mM NaH_2PO_4, 500 mM NaCl, 250 mM imidazole pH 8	Superdex-200-1660-pg 20 mM Tris, 150 mM NaCl, 5 mM $MgCl_2$, 1 mM ATP, pH 8
FLAG-KaiC-AE (S431A, T432E)	30 ºC, 12 h	50 mM NaH_2PO_4, 500 mM NaCl, pH 8	50 mM NaH_2PO_4, 500 mM NaCl, 80 mM imidazole pH 8	50 mM NaH_2PO_4, 500 mM NaCl, 250 mM imidazole pH 8	Superdex-200-1660-pg 20 mM Tris, 150 mM NaCl, 5 mM $MgCl_2$, 1 mM ATP, pH 8
FLAG-KaiC-EE (S431E, T432E)	30 ºC, 12 h	50 mM NaH_2PO_4, 500 mM NaCl, pH 8	50 mM NaH_2PO_4, 500 mM NaCl, 80 mM imidazole pH 8	50 mM NaH_2PO_4, 500 mM NaCl, 250 mM imidazole pH 8	Superdex-200-1660-pg 20 mM Tris, 150 mM NaCl, 5 mM $MgCl_2$, 1 mM ATP, pH 8
FLAG-KaiC-EA (S431E, T432A)	30 ºC, 12 h	50 mM NaH_2PO_4, 500 mM NaCl, pH 8	50 mM NaH_2PO_4, 500 mM NaCl, 80 mM imidazole pH 8	50 mM NaH_2PO_4, 500 mM NaCl, 250 mM imidazole pH 8	Superdex-200-1660-pg 20 mM Tris, 150 mM NaCl, 5 mM $MgCl_2$,1 mM ATP, pH 8
G-SasA	30 ºC, 12 h	50 mM NaH_2PO_4, 500 mM NaCl, pH 8	50 mM NaH_2PO_4, 500 mM NaCl, 20 mM imidazole pH 8	50 mM NaH_2PO_4, 500 mM NaCl, 250 mM imidazole pH 8 + 10 mM TCEP	Superdex-200-1660-pg 20 mM Tris, 150 mM NaCl, 5 mM $MgCl_2$, 1 mM ATP, pH 8
G-SasA-H161A	30 ºC, 12 h	50 mM NaH_2PO_4, 500 mM	50 mM NaH_2PO_4, 500 mM	50 mM NaH_2PO_4, 500 mM	Superdex-200-1660-pg

		NaCl, pH 8	NaCl, 20 mM imidazole pH 8	NaCl, 250 mM imidazole pH 8 + 10 mM TCEP	20 mM Tris, 150 mM NaCl, 5 mM $MgCl_2$, 1 mM ATP, pH 8
FLAG-CikA-LPETGG	20 ºC, 22 h	50 mM NaH_2PO_4, 500 mM NaCl, pH 8	50 mM NaH_2PO_4, 500 mM NaCl, 20 mM imidazole pH 8	50 mM NaH_2PO_4, 500 mM NaCl, 250 mM imidazole pH 8 + 20 mM TCEP	Superdex-200-1660-pg 20 mM Tris, 150 mM NaCl, 5 mM $MgCl_2$, pH 8
FLAG-CikA-H393A	20 ºC, 22 h	50 mM NaH_2PO_4, 500 mM NaCl, pH 8	50 mM NaH_2PO_4, 500 mM NaCl, 20 mM imidazole pH 8	50 mM NaH_2PO_4, 500 mM NaCl, 250 mM imidazole pH 8 + 20 mM TCEP	Superdex-200-1660-pg 20 mM Tris, 150 mM NaCl, 5 mM $MgCl_2$, pH 8
GGG-RpaA	30 ºC, 12 h	50 mM NaH_2PO_4, 500 mM NaCl, pH 8	50 mM NaH_2PO_4, 500 mM NaCl, 20 mM imidazole pH 8	50 mM NaH_2PO_4, 500 mM NaCl, 250 mM imidazole pH 8	Superdex-75-1660-pg 20 mM Tris, 150 mM NaCl, 5 mM $MgCl_2$, 1 mM ATP, pH 8
GGG-RpaA-R121Q	30 ºC, 12 h	50 mM NaH_2PO_4, 500 mM NaCl, pH 8	50 mM NaH_2PO_4, 500 mM NaCl, 20 mM imidazole pH 8	50 mM NaH_2PO_4, 500 mM NaCl, 250 mM imidazole pH 8	Superdex-75-1660-pg 20 mM Tris, 150 mM NaCl, 5 mM $MgCl_2$, 1 mM ATP, pH 8

All purification steps were carried out at 4 ºC. For cleavage of the 6x-His-SUMO fusion protein, 6x-His-ULP1 protease was added to final concentration of 3 µM and incubated at 4 ºC for 15 h. Reductant tris(2-carboxyethyl)-phosphine (TCEP) was added to SasA and CikA samples during ULP1 cleavage (concentrations given in **Table 2.3**). 6x-His-SUMO was removed by loading the cleaved protein on a Ni-NTA column for a second time. The flow-through was concentrated using 10 kDa molecular weight cut-off (MWCO) membrane filters in an Amicon™ (Millipore Sigma) stir-celled concentrator at 4 ºC before purifying by gel-filtration chromatography.

SasA used for two-dimensional titration experiments was purified as His-Gβ1-tagged full-length SasA constructs over Ni-NTA resin using the standard protocol described previously (*43*), followed by overnight cleavage at 4°C with TEV protease with final concentration of 0.1 mg/mL. SasA was subsequently resolved from the His-Gβ1 tag on a Sephadex 200 size-exclusion column (GE Healthcare) equilibrated with 20 mM Tris, 150 mM NaCl pH 7.4.

Fluorescent labeling of proteins

N-terminal sortase-mediated ligations were performed for full-length protein constructs used in IVC that had been modified to carry an N-terminal glycyl residue. The fluorophore-containing peptides 5-carboxyfluorescein (5-FAM)-LPETGG and C-(Cy3)-LPETGG were purchased from GenScript (New Jersey). For C-terminal ligations, target proteins were fused to sortase-A recognition peptide LPETGG at the

C-terminus. The peptide GGGYCN was expressed and purified in-house as a 6x-His-SUMO-fusion protein. The cysteinyl residue on the purified fusion protein was labeled with the fluorophore 6-iodoacetamidofluorescein (6-IAF) (Invitrogen) as described previously (*101*). The labeled peptide was cut from the SUMO-fusion protein using ULP1 and passed through 10 kDa MWCO membrane in stirred cell concentrator. The flow-through containing labeled peptide was further purified by C4 reverse-phase column chromatography. The peptide was eluted with a linear acetonitrile gradient and then lyophilized. Dried peptide was dissolved in sortase buffer before use. Concentration was determined by UV absorbance by the 6-IAF fluorophore at 493 nm. Each target protein was buffer exchanged in sortase buffer (20 mM Tris, 150 mM NaCl, pH 7.5) before ligation. For ligation, 50 μM target protein was incubated with 250 μM fluorophore peptide, 5 μM sortase-A, and 10 mM $CaCl_2$ in the dark at 4 ºC for 12-16 h. Sortase-A was separated from reaction mixtures by Ni-NTA chromatography using prepacked 5 mL HiTrap-Ni-NTA columns (GE Healthcare) on an AKTA FPLC using a step gradient of imidazole. Labeled protein fractions were concentrated and purified further by gel-filtration chromatography using a Superose-6-Increase-10/300 GL analytical grade column (GE Healthcare). Fluorescence labeling of fsKaiB, $SasA_{trx}$, and $CikA_{psr}$ constructs was done with 6-iodoacetamidofluorescein (6-IAF, Invitrogen) as described previously (*36*).

Reconstitution of clock reactions for fluorescence anisotropy measurements

For monitoring multiple probes simultaneously, a master mix of oscillator reactions was prepared in 20 mM Tris, 150 mM NaCl, 5 mM $MgCl_2$, 1 mM ATP, and pH 8.0 buffer by mixing unlabeled proteins at the final concentrations shown in **Table 2.3,** except for KaiC and fluorescently labeled probes. IVC reactions were initiated by adding a solution of KaiC and ATP to the master mix. Aliquots (95 µL) of reaction master mix were pipetted into black, non-binding 384-well microplates (Greiner BioOne). Finally, 5-µL aliquots of fluorophore-labeled protein (50 nM final concentration) or DNA (100 nM final concentration) were added to separate wells. The plate was sealed using clear, adhesive film (MicroAmp™). The plate was transferred to a CLARIOstar multimode microplate reader (BMG Labtech), pre-equilibrated at 30 ºC. The plate was incubated for 30 minutes prior to starting measurements to allow equilibration of all samples. Detector gain for parallel and perpendicular channels was adjusted on a 50 nM or 100 nM fluorescent probe mixed in buffer, where the target polarization was set to 10% of the maximum theoretical polarization of fluorescein (350 milli-polarization units). Fluorescence polarization was measured in kinetic mode, every 15 minutes for 800 cycles. Fluorescence polarization (FP) was converted to fluorescence anisotropy (FA) in CLARIOstar MARS software before analysis. All the anisotropy values are reported in millianisotropy (mA) units.

Fluorescence anisotropy oscillator data in Figs. 3 and 4 and Figs. S15-S20 were collected *in vitro* on either a CLARIOstar (BMG) or Spark 10M (TECAN) microplate reader. The fluorescein channel was used for all data collection ($\lambda_{excitation}$, 482 ± 8 nm; $\lambda_{emission}$, 530 ± 20 nm). Fluorescence anisotropy was monitored from each well in the 384-well plate and recorded every 15 minutes, with time zero representing 3-5 minutes following the addition of KaiC to oscillation reactions.

Phosphorylation assays for KaiC and RpaA

For phosphorylation measurements, 250 µL samples from identical clock reactions were incubated in parallel with the FA experiments and special attention was taken to ensure that phosphorylation reactions were initiated identically to FA reactions by the addition of a solution of KaiC and ATP to a master mix. For detection of RpaA phospho-states, fluorophore-labeled RpaA (50% of total concentration) was used. Samples were incubated at 30 ºC in a benchtop water bath. Aliquots (8 µL) were removed every 4 h by manual pipetting over a period of 72 h. Each aliquot was immediately flash frozen by dipping the tubes in liquid nitrogen and storing at -80 ºC until all the aliquots were collected. For phosphorylation analysis, time points were first run on Zn^{2+}-Phos-tag^{TM} gels as described below and then the same set of aliquots was run on 7.5% SDS-PAGE for analysis of KaiC~P states.

Sample preparation and analysis on Phos-tagTM gels

Frozen protein aliquots were thawed on ice for 15 minutes and mixed with 8 µL of chilled 2x-SDS-PAGE loading buffer. Samples were spun at 1500 rpm for 30 seconds and transferred quickly to ice. In each lane 4 µL samples were loaded on precast 50 µM-Zn^{2+}-Phos-tag™ -12.5% SDS-PAGE gels (Wako Chemicals, Japan). Phosphorylated RpaA was separated by electrophoresis at constant voltage (140 V) for 2 h in freshly prepared 1x running buffer (100 mM Tris, 100 mM MOPS, 0.1% SDS and 5 mM sodium bisulfite, pH 7.8). The electrophoresis apparatus was kept in an ice bath during electrophoresis and running buffer was chilled to 4 ºC before use. Fluorescent bands of RpaA were visualized under UV transillumination (E-Gel Imager, Thermo fisher) immediately after electrophoresis was completed and before staining the gels with Coomassie blue protein gel stain.

SDS-PAGE for KaiC phosphorylation

Aliquots prepared for Phos-tag™ gels were saved at -20 ºC until analysis. Samples were boiled at 95 ºC for 5 min and spun down at 15000 rpm for 30 seconds before loading on 7.5% SDS-PAGE gels. Samples (4 µL) were loaded in each well and two-step electrophoresis was performed at 60 V for 30 min followed by at 140 V for 1 h 40 min. The electrophoresis apparatus was kept in an ice bath and pre-chilled running buffer was used. Gels were stained with InstantBlue® protein gel stain (Expedeon Inc., Novus Biologicals, Centennial Co.) for at least 1 h followed by de-staining in D.I. water for 30 minutes. Gels were imaged by E-gel Imager (Invitrogen,

Thermo Fisher Scientific). Densitometry of gel images was performed using NIH ImageJ software (*119*).

ATPase activity measured by 1H-NMR

A solution of 1.2 μM KaiA, 3.5 μM KaiB, 3.5 μM KaiC, 95% H_2O, 5% D_2O, and 10 μM DSS was prepared in a reaction buffer containing 20 mM Tris, 100 mM NaCl, 1 mM ATP, 5 mM $MgCl_2$, pH 8. The oscillator reaction was initiated by adding a solution of KaiC and ATP to a solution of KaiA and KaiB. One-dimensional proton NMR spectra were measured at 30 ºC, every hour for 5 days. The ATP and ADP peaks were fit using an interpolation function in Wolfram Mathematica. Peak intensities were plotted as function of time and fit to a straight line from which overall ATPase activity was determined. Oscillations of ATP and ADP resonances about the line provided the determination of ATPase rhythms.

Data fitting for phase and period analysis

First 12 h of raw data were removed before analysis because during this time samples are approaching stable limit cycles. Anisotropy and phosphorylation data were baseline-corrected using a quadratic function and normalized to ±1 before fitting to a damped single cosine function:

$$Y = a\ cos\ [2\pi\left(\frac{t}{p}\right) - \phi]e^{-kt}$$

where, a = amplitude, p = period, $\phi = phase\ angle$, k = decay constant.

Fluorescence data quantification and statistical analyses in titration experiments

Fluorescence anisotropy readings from clock reactions were collected in MARS Data Analysis Software or SparkControl Software for experiments run on the BMG CLARIOstar Plus or TECAN Spark 10M, respectively. All data were analyzed in the online BioDare suite by FFT-NLLS (*120, 121*) (https://biodare2.ed.ac.uk/welcome). Prior to analysis, fluorescence anisotropy rhythms were baseline detrended and normalized to [-1, 1] with mean of zero. The first 12-h of data were disregarded for quantification of period, amplitude, and phase.

Comparisons of the effects of added SasA or CikA on period and amplitude under different concentrations of the core clock proteins KaiA and KaiB were determined by ordinary two-way ANOVA with Dunnett's multiple comparison tests in Prism 8 (GraphPad). The damping constant, k, was determined in Prism 8 (GraphPad) using a nonlinear least square regression cosinor fit:

$$y = m * x + amplitude * e^{-kx} * cos\left[\left(2\pi * \frac{x}{period}\right) + phase\right]$$

where y is the signal, x the corresponding time, amplitude is the height of the peak of the waveform above the trend line, k is the decay constant (such that 1/k is the half-life), period is the time taken for a complete cycle to occur and phase is the shift in x relative to a cosinor wave.

Strains and culture conditions for in vivo experiments

Synechococcus elongatus PCC 7942 and its derivative strains were maintained on BG-11 medium containing antibiotics as needed for selection (*122*). Growth on

plates or in liquid medium was carried out at 30 ºC under 150 µmol m^{-2} s^{-1} light. *E. coli* DH5α used for cloning was grown on LB with the appropriate antibiotics at 37 ºC.

Construction of rpaA-R121Q strain

Introduction of point mutations into the *S. elongatus* chromosome was accomplished using a previously described CRISPR-editing approach *(110).* The pSL2680 (Km^R) plasmid used for CRISPR-Cas12a (formerly Cpf1) editing was purchased from Addgene (Plasmid #85581). Primers rpaA_gRNA_F and rpaA_gRNA_R were annealed together and ligated into AarI-cut pSL2680 to serve as the *rpaA-R121Q* gRNA template. The resulting construct was purified and digested with KpnI to facilitate insertion of the *rpaA-R121Q* homology directed repair (HDR) template. The HDR template was generated by amplifying overlapping upstream and downstream fragments using primers rpaA_HDR-UP_F and rpaA_HDR-UP_R (AMC1722 genomic DNA as template) and rpaA_HDR-DWN_F and rpaA_HDR-DWN_R (AMC541 genomic DNA as template), respectively. The upstream and downstream HDR fragments were assembled into KpnI-cut pSL2680+gRNA using the GeneArt Seamless Assembly Kit (Thermo Fisher Scientific), forming pDE32. Plasmid pDE32 was electroporated into *E. coli* DH10B containing a helper plasmid pRL623 (chloramphenicol resistance, Cm^R) and conjugal plasmid pRL443 (ampicillin resistance, Ap^R) *(123)*. The resulting strain was grown overnight in LB medium containing antibiotics (Ap, kanamycin (Km), and Cm), washed 3x with fresh LB, and

mixed in a 1:2 ratio with an *S. elongatus* reporter-strain aliquot. The cell mixture was plated onto BG-11 agar with added LB (5% vol/vol), incubated under 100 μmol m^{-2} s^{-1} light for 36 h, then underlaid with Km (10 μg/ml final concentration) to select for *S. elongatus* cells that contain pDE32. Colonies that emerged after 6-8 days were passaged three times on BG-11 agar containing Km to allow editing to occur. Successful editing of chromosomal *rpaA* was verified by sequencing. Plasmid pDE32 was cured from the edited strain by inoculating cells into non-selective BG-11 medium, growing the culture to OD_{750} = 0.6, then dilution plating on non-selective BG-11 plates. Fifty colonies were picked and replica patched to selective (Km) and non-selective medium to identify and isolate clones that had lost pDE32.

Generation of SasA mutants in S. elongatus

Markerless point mutations were introduced in *sasA* of *Synechococcus elongatus* PCC 7942 by CRISPR/Cas12a engineering as previously described (*110*). Briefly, oligos with complementarity to the guide RNA (gRNA) recognition site were annealed and cloned into AarI-cut pSL2680 (Addgene Plasmid #85581). Clones of pSL2680 that carry the appropriate gRNA insert were isolated and plasmid sequences were verified. Upstream and downstream homologous repair templates that encode the point mutation(s) of interest were amplified by PCR and assembled (GeneArt Seamless Assembly, Thermo Fisher) into KpnI-cut constructs that contain the respective gRNAs. Recovered plasmids were checked for accuracy by Sanger sequencing prior to editing in *S. elongatus*.

The RSF1010-based editing constructs were electroporated into *E. coli* AM1359 that contain conjugal helper plasmids (pRL623 and pRL443) as previously described (*124-127*). The resulting *E. coli* strains were grown overnight in LB containing ampicillin (100 µg/ml), chloramphenicol (17 µg/ml) and kanamycin (50 µg/ml). Cells from a 1 ml aliquot were washed three times with fresh LB and resuspended in a final volume of 100 µl LB, then mixed with 100 µl of an *S. elongatus* clock-reporter strain (AMC541) concentrated down from 2 ml of a dense culture (OD_{750} = ~0.6). The mixed culture was plated to solid BG-11 medium containing 5% LB (v/v) and incubated at 30˚C under 30 µmol photons m^{-2} s^{-1} (µE) illumination for 24 hours. Plates were then underlaid with kanamycin (5 µg/ml final concentration) to select for the editing plasmid. *S. elongatus* colonies that emerged after 8-10 days at 30˚C and 100 µE light were serially patched three times to BG-11 containing kanamycin to maintain the editing plasmid long enough to complete segregation of the mutant allele in all copies of the chromosome. After editing, *sasA* was amplified by colony PCR using primers that anneal outside of the homologous repair region and the resulting PCR product was submitted for Sanger sequencing to confirm segregation of the point mutation(s) of interest.

Bioluminescence monitoring of S. elongatus circadian rhythms

Bioluminescence was monitored using a P*kaiBC*::*luc* firefly luciferase fusion reporter inserted into a neutral site of the *S. elongatus* chromosome as previously described *(122)*. Strains to be monitored were grown in liquid culture to OD_{750} = 0.4-

0.7, diluted to OD_{750} = 0.2, and added as 20 µl aliquots to 280 µl of BG-11 agar containing 3.5 mM firefly luciferin arrayed in 96-well plates. Plates were covered with a gas-permeable seal and cells were entrained under 12-h light-dark cycles (80 µmol m^{-2} s^{-1} light) to synchronize clock phases. After 48 h of entrainment, cells were released into continuous light (30 µmol m^{-2} s^{-1}) and bioluminescence was monitored every 2 h using a Tecan Infinite Pro M200 Bioluminescence Plate Reader. Mutant *sasA* strains, along with positive and negative clock-output controls, were grown in BG-11 medium, diluted to OD_{750} = 0.2 and arrayed in 96-well plates containing solid BG-11 medium and 10 µl of 5 mM D-luciferin. Plates were covered by a gas permeable seal and incubated in a light-dark chamber at 30˚C for 48 hours, with 12 h intervals of 120 µE light and darkness. Following release into constant light at the end of 48 hours, plates were transferred to a lighted stacker (40 µE light) attached to a Tecan Infinite M200 Pro and bioluminescence was monitored every 2-3 hours. The raw bioluminescence data were plotted as a function of time (GraphPad Prism 8) and processed using BioDare2 to determine period and amplitude for each set of replicates.

Immunoblotting

For detection of RpaA phosphorylation flask-grown cells were collected (15 ml) at ZT 0 and ZT 12 from liquid cultures (OD_{750} = 0.6-0.7) incubated under 12-h light-dark cycles (40 µmol m^{-2} s^{-1}). Cells were pelleted, washed once with cold 10 mM sodium chloride solution and frozen at -80 ºC. Cell pellets were thawed on ice

and resuspended in tris-buffered saline (pH 7.4) containing 1 mM phenylmethylsulfonyl fluoride, then disrupted by bead beating at 4 ºC (30 s of beating, followed by 2 min on ice for 10 cycles). Following centrifugation (20,000 x *g* for 10 min), protein concentrations were determined by the Bradford assay and a total of 10 µg of protein was loaded per well. Phos-tag™ reagent (20 µM) (Wako Chemicals, Japan) and manganese chloride (100 µM) were added to standard SDS-PAGE gels (12.5 %) to allow detection of phosphorylated RpaA. Electrophoresis was conducted on ice using pre-chilled running buffer to limit hydrolysis of the heat-labile phospho-aspartate. Current was maintained at 25 mA until the bromophenol blue dye reached the bottom edge of the gel. The gel was then incubated for 10 min in transfer buffer containing 10 mM EDTA, followed by a 10 min incubation in transfer buffer without EDTA prior to semi-dry transfer to a PVDF membrane using a Trans-Blot Turbo System (BioRad). Detection of RpaA was achieved using RpaA-antiserum (gift from E. O'Shea, HHMI–Janelia, Ashburn, VA) at a dilution of 1:2000 as described previously *(128, 129)*. Secondary antibody (goat anti-rabbit IgG; 401315, Calbiochem) was used at a dilution of 1:100,000 and chemiluminescent signal was produced using the SuperSignal West Femto Maximum Sensitivity Substrate (Thermo Fisher Scientific).

For detection of total SasA levels protein extraction was performed as described above. Bio-Rad Any kD™ Mini-PROTEAN® TGX™ Precast Protein Gels (cat #4569036) were used to perform SDS-PAGE with 10 µg of protein loaded per well. Detection of SasA was achieved using SasA-antiserum (Aves Lab) at a dilution

of 1:4000. Secondary antibody (goat anti-chicken IgY; ab96947, Abcam) was used at a dilution of 1:5000 and chemiluminescent signal was detected by using the SuperSignal West Femto Maximum Sensitivity Substrate (Thermo Fisher Scientific) and imaging with BioRad ChemiDoc system.

Crystallization of monomeric T. elongatus C1 domain in complex with T. elongatus $SasA_{trx}$

A monomeric mutant of *T. elongatus* KaiC-CI domain (see **Table 2.2** for details) was incubated at 250 μM with an excess of *T. elongatus* $SasA_{trx}$ (460 μM) overnight in 20 mM Tris pH 7.0, 150 mM NaCl, 5 mM DTT, 1 mM $MgCl_2$ and 1 mM ATP at room temperature. The complex was subsequently purified by size-exclusion chromatography on a Sephadex 70 column (GE Healthcare) equilibrated in the same buffer, but with $MgCl_2$ and ATP concentrations reduced to 0.5 mM. The complex was mixed in a 1:1 ratio to a final concentration of 10.8 mg/mL with the crystallization buffer containing 1.26 M NaH_2PO4, 0.54 M K_2HPO_4 (pH unadjusted, total PO_4 concentration 1.8 M), 0.1 M Glycine (added from a 1 M solution adjusted to pH 10.5) and 0.2 M $Li_2(SO_4)_2$. Crystals formed over 10 days at 22 °C using the hanging drop method. The flat, plate-like crystals were then frozen in liquid nitrogen after soaking in cryoprotectant composed of the crystallization buffer plus 20% (v/v) glycerol.

Structure determination and refinement

Single crystal diffraction data were collected with a wavelength of 1 Å on the 23-ID-D X-ray source at the Advanced Photon Source at the Argonne National Laboratory. Data were processed and scaled using iMOSFLM (*130*) and Aimless (*131*). Phases were solved by molecular replacement with the structure of *T. elongatus* KaiC-CI monomer in complex with fsKaiB (PDB 5JWO) using Phaser (*132*). Refinement and model building were performed using Phenix (*133*) and Coot (*134*). See **Table 2.1** for crystal and refinement statistics. Structural figures were made using UCSF Chimera (*135, 136*) and ChimeraX (*137*).

Equilibrium binding assays

Binding titrations were performed in 20 mM Tris pH 7.4, 150 mM NaCl, 1 mM ATP, 1 mM $MgCl_2$ and 0.1 % (v/v) Tween-20. Fluorescein-labeled KaiB or $SasA_{trx}$ probes were present at 50 nM, while the titrant was diluted serially in 1/3-fold increments. Serial dilutions were performed in a 384-well plate before sealing with tape and incubating at room temperature overnight (9-15 h). Fluorescence polarization anisotropy measurements were subsequently collected on a Synergy2 plate reader (BioTek). Twenty replicate measurements were collected and averaged for each well. For 2D titration assays looking at the effect of an additive on KaiB binding to KaiC, fsKaiB or SasA additives were included in both KaiC and diluent buffer to maintain a constant concentration. Diluent was added to the 384-well plate

using a single channel pipettor, and additives were mixed into the KaiC stock last and diluted within 10 minutes. See thermodynamic modeling of binding equilibria below for more information.

Thermodynamic modeling of binding equilibria

The fluorescence anisotropy titrations outlined above involve cooperative and competitive reactions and span a wide range of concentrations, such that free ligand concentrations cannot be approximated by the total added concentration. Consequently, these data cannot be analyzed by fitting to standard analytical equations (*138*). Fitting the data to the profiles simulated by a model avoids this problem but introduces others in terms of the complexity of the model that is required for the fit. Initially, we attempted to fit to a general hexameric model for KaiC but found there were too many parameters to reach convergence. When simplified to a dimer model, the fits were reasonably robust and showed no systematic deviations. Nevertheless, such a simplified model required positive heterotropic or homotropic cooperativity between KaiB and additives such as SasA and fsKaiB, respectively, as well as competition between these additives. Thus, a dimer model captures the essence of the interaction, although how this relates in detail to cooperativity within the KaiC hexamer remains in question.

Least-squares fitting analysis to models was performed using DynaFit (BioKin) (*139*). Statistical analysis was performed using the Monte Carlo routine whereby cooperativity indices (defined by $K_1/K_3 = K_2/K_4$) were calculated for each

simulation (n = 1000) and median and 95% confidence intervals taken as ranks 500, 25 and 975 (respectively) in the n = 1000 simulation. Where replicate measurements are reported, the values of median or 95% confidence boundaries were averaged amongst the replicates.

In order to reduce the number of parameters of the fit, the binding of KaiB alone was initially modeled without any homotropic cooperativity by assigning $K_5 = 4*K_1$, as is appropriate for the macroscopic equilibrium constants for two-site independent binding. When K_5 was floated, a slightly improved fit was obtained with a returned $K_5 < K_1$, indicative of homotropic cooperativity, but K_5 was not robustly defined. The value of the heterotropic cooperativity index in the presence of additives increased when K_5 was floated, however, we report fits where K_5 was defined as $4*K_1$ for simplicity, which gives a minimal estimate of the heterotropic cooperativity index.

Triplicate 2D titrations were collected with SasA to optimize the analysis and showed some variability that was ameliorated by floating additive concentrations at the 3 highest additive concentrations. The averages from these fits were used for SasA and KaiB variant 2D titration datasets when analyzing 300 nM data, where additive concentrations were also allowed to float. Little variation was seen in the experimental anisotropy values determined for fluorescently labeled KaiB alone or the final peak values for the KaiB-KaiC complex, though the average peak experimental anisotropy values of putative ternary complexes seeded by

heterocooperativity differed modestly between the SasA and fsKaiB variants (KaiB peak anisotropy = 0.211 for SasA or 0.205 for fsKaiB).

Size-exclusion chromatography-multiangle light-scattering (SEC-MALS)

SEC-MALS assays were performed at room temperature using a silica-based size-exclusion column (particle size 5 μm, pore size 500 Angstrom, 4.6 mm ID, Cat. No. WTC-050N5, Wyatt Technologies) to resolve the oligomeric state of SasA. 20 μL injections of full-length SasA at 1.5 mg/mL were made using an Agilent G1311A quaternary pump and manual injector (Rheodyne), run over the silica-based column, and analyzed by a T-rEX refractometer and miniDAWN TREOS II static multiangle light scattering instrument (Wyatt Technologies) directly after the column. Analysis of absolute molecular weight was carried out using Astra 6.0 software (Wyatt Technologies).

^{32}P phosphotransfer assay

Assays were performed in the presence of **γ**-^{32}P ATP as originally described (*57*). These experiments were conducted with 5 μM KaiC-EE, 3.5 μM RpaA, and 2.5 μM SasA variant in 0.1 mM ATP. To do this 100 μM KaiC in 1.0 mM ATP was diluted with 20 mM Tris pH 7.4, 150 mM NaCl, 1 mM $MgCl_2$, 1 mM TCEP. 4 μL of undiluted **γ**-^{32}P ATP (EasyTides).

SasA-WT and SasA-DM were compared in this assay by quenching the reactions at discrete timepoints using an equivalent volume of 6x SDS-PAGE loading

buffer. ^{32}P labeled protein was separated on an anyK_D^{TM} pre-cast SDS-PAGE gel (BioRad). Gels were dried and exposed overnight for visualization on a Typhoon phosphorimager, and subsequent quantification by densitometry. Slopes of the resulting trajectories were compared in triplicate between wild-type SasA and SasA-H28A-Q94A to determine the % activity the double mutant. A control was also included where no RpaA was added to quantify the efficiency of initial histidine phosphorylation to the SasA variants, and triplicate densitometries were compared at a single timepoint.

Chapter 3: Coupling of distant ATPase domains in the circadian clock protein KaiC

3.1 Abstract

The AAA+ family member KaiC is the central pacemaker for circadian rhythms in the cyanobacterium *Synechococcus elongatus*. Composed of two hexameric rings of adenosine triphosphatase (ATPase) domains with tightly coupled activities, KaiC undergoes a cycle of autophosphorylation and autodephosphorylation on its C-terminal (CII) domain that restricts binding of clock proteins on its N-terminal (CI) domain to the evening. Here, we use cryo-electron microscopy to investigate how daytime and nighttime states of CII regulate KaiB binding on CI. We find that the CII hexamer is destabilized during the day but takes on a rigidified C_2-symmetric state at night, concomitant with ring-ring compression. Residues at the CI-CII interface are required for phospho-dependent KaiB association, coupling ATPase activity on CI to cooperative KaiB recruitment. Together, these studies clarify a key step in the regulation of cyanobacterial circadian rhythms by KaiC phosphorylation.

3.2 Introduction

Cyanobacteria possess an internal circadian clock that temporally aligns gene expression with the solar day to maximize photosynthetic output and coordinate integrated metabolic processes (*10, 76, 140*). The most basic manifestation of this timekeeping function is a cyclic pattern of autophosphorylation in CII domain of the hexameric clock protein KaiC (*29*) that results in the following sequence of post-translational modifications at residues S431 and T432: S/T → S/pT → pS/pT → pS/T (*31, 38*). During the day, autophosphorylation is stimulated by another clock protein, KaiA, which binds to the C-terminal end of KaiC, known as the A-loop, to upregulate KaiC autophosphorylation (*34*). At night, compression of the two KaiC rings partially opens the CI ring to expose binding sites (*35*) that allow a third clock protein, KaiB, to be cooperatively recruited to KaiC (*56, 70, 100, 104*), where it undergoes a conformational change to bind and sequester KaiA (*35, 50*). Without KaiA bound to CII, the equilibrium of KaiC shifts toward CII autodephosphorylation (*34*), which proceeds until affinity for KaiB on CI is lost. At this point, KaiA and KaiB dissociate from CI, as well as from each other, allowing KaiA to once again bind KaiC via its A-loops, thus completing a negative feedback loop that takes around 24 hours per cycle.

Both *in vitro* and *in vivo* studies have linked the S/T and S/pT phosphostates of KaiC with the daytime when the CII domains are loosely bound to each other (*43*) and the A-loops are exposed (*50*), facilitating KaiA binding (*31, 38*). By contrast, the pS/pT and pS/T states are associated with the KaiB-bound nighttime state of KaiC,

where KaiA is sequestered in its inactive form on the CI domain (*35, 37, 51*). Formation of the repressive nighttime complex is linked to the ATPase cycle of the CI domain, as mutations that block CI ATPase activity are deficient in KaiB binding (*28*) and the KaiC CI domain is only found in the ADP-bound form when bound to KaiB (*37, 51*).

CI ATPase activity and CII autophosphorylation appear to be functionally linked as well because mutations in either domain can give rise to correlated changes in CI ATP hydrolysis and the overall period of biochemical oscillations (*39*). In particular, substitutions of the Tyr402 residue at the interface between CI and CII gives rise to extreme changes in period and correlated ATPase activity depending on the amino acid substituted into this position (*99*). This residue is poised on the CII-α8 helix near a patch of CI residues known as the arginine tetrad that are essential for circadian rhythms *in vivo* (*141*), suggesting the existence of an allosteric conduit connecting the CI and CII active sites that runs through these regions. However, no direct structural evidence exists for this hypothesis, and it currently remains unclear how the information encoded by CII phosphorylation state is transduced roughly 70 Å to regulate KaiB binding on CI.

KaiC can be trapped in its daytime or nighttime-like states using phosphomimetic substitutions at the CII autophosphorylation sites (*31, 55, 142*). Herein, we used KaiC-S431A-T432E as a daytime phosphomimetic (referred to as KaiC-AE) and KaiC-S431E-T432A to represent the nighttime variant (KaiC-EA) to study how phosphorylation influences conformational changes and coupling between

CI and CII domains. Solution biophysical studies have demonstrated modest changes in the global conformation of KaiC throughout the phosphocycle (*42, 143*) as well as in the intra- (*cis*) and inter- (*trans*) subunit interactions of ATPase domains using these phosphomimetics mutations (*43, 144*).

Despite the stark differences in KaiC protein dynamics and clock protein association observed in solution studies, crystallographic experiments have not provided a suitable explanation for the distinct biochemical properties of KaiC phosphomimetics (*41, 141*), likely due to crystal packing forces. Given the intrinsically dynamic nature of KaiC (*143, 145, 146*) and incident shallow conformational energy landscape, we sought to circumvent these issues by employing cryo-electron microscopy (cryo-EM) to obtain structures of daytime and nighttime KaiC by single particle reconstruction. This revealed previously unobserved conformations that demonstrate how information encoded by CII phosphorylation is transmitted through dynamic structural features to regulate biochemical activity on CI.

3.3 Comparison of daytime and nighttime KaiC structures

To establish a baseline for KaiB discrimination between the phosphomimetics, we first compared KaiB affinity in the daytime and nighttime-trapped forms of KaiC (**Fig. 1A, Supplemental Fig. 1**). We observed ≥30-fold tighter binding of KaiB to nighttime KaiC than the daytime variant, recapitulating the previously observed day/night distinction between KaiC-AE and KaiC-EA phosphomimetics (*31*). Next,

we subjected KaiC-EA and KaiC-AE to comparison by cryo-EM in the presence of saturating concentrations of ATP to identify potential structural differences between the phosphomimetic variants.

For daytime KaiC, we observed a decrease in well-defined cryo-EM density for the CII ring (**Fig. 1B**), consistent with previous solution studies where the S/pT state or phosphomimetic AE mutant of KaiC exhibited an 'open' or destabilized CII hexamer (*43, 147*). Since flexible domains are often susceptible to damaging interactions with the hydrophobic air-water interface during sample preparation, we also characterized daytime KaiC in the presence of perfluorinated *fos*-choline, which limits air-water-interface interactions (*148*). KaiC phosphomimetics maintained their functional discrimination for KaiB binding in the presence of *fos*-choline (**Fig. 3.2**), indicating that the structures observed under these conditions are functionally relevant. The inclusion of *fos*-choline stabilized the same 'extended' conformation in daytime KaiC that was originally observed by crystallography (*26*) (**Fig. 3.3A**), resolved to ~3.8 Å in our cryo-EM structure.

Although a saturating concentration of ATP was present in solution, we found ADP bound at CII-CII interfaces in the 'extended' conformation of daytime KaiC (**Fig. 3.4A**). It should be noted that because both phosphorylation sites were mutated in our constructs, the ADP nucleotide accumulated at this site likely came from low concentrations of ADP present in solution, possibly arising from catalytic turnover at the CI domain. Because the original structures were obtained from crystals grown in the presence of non-hydrolyzable ATP analogues (*26, 41*), this suggests that the C_6-

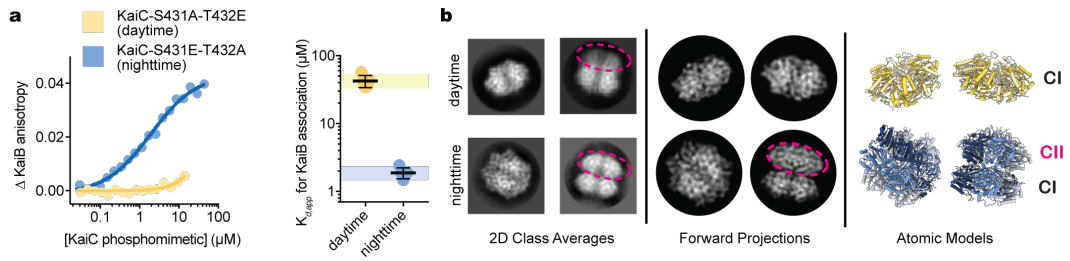

Fig. 3.1. Daytime and nighttime phosphomimetics confer distinct biochemical activities and global conformations to KaiC.

A) Titration curves and apparent binding constants ($K_{d,app}$) for KaiB association with daytime or nighttime KaiC phosphomimetics in units of protomer concentration, as measured using fluorescence anisotropy of labeled KaiB in KaiC titrations. Black lines and error bars represent mean ± standard deviation (sd) from n = 5 independent titrations. The hashtag (#) represents $P < 0.0001$ from a 2-sided unpaired parametric t-test between the two phosphomimetics. 95% confidence interval (c.i.) for the measurements on the daytime and nighttime phosphomimetic variant are depicted as colored boxes (light blue for nighttime, light yellow for daytime). This depiction is used throughout the manuscript for comparison of other variants to the unsubstituted phosphmimetics. Mean $K_{d,app}$ ± sd is 2 ± 0.4 μM for nighttime KaiC and ≥ 43 ± 8 μM for daytime KaiC. In cases where upper bound is reported, $K_{d,app}$ was too high to measure (see Fig. S1 and Methods). **B**) Reference-free 2-dimensional class averages from electron micrographs of KaiC phosphomimetics. Dashed ovals indicate the CII rings, where visible, as inferred from forward projections obtained using the atomic models shown.

symmetric 'extended' conformation can accommodate either ATP- or ADP-bound nucleotide state at CII in daytime KaiC, though ADP appears to be preferred. Notably, we also observed the C_6-symmetric extended conformation favored by crystallography in nighttime KaiC, this time at ~2.8 Å resolution, but with ATP in the CII active sites (**3.4B**). Because CII dephosphorylation proceeds through an ADP-bound intermediate (*44, 48*), this preference likely functions to delay dephosphorylation of the nighttime state until the ATP/ADP ratio has fallen sufficiently, aligning the phase of the oscillator with cellular metabolism (*76, 82*).

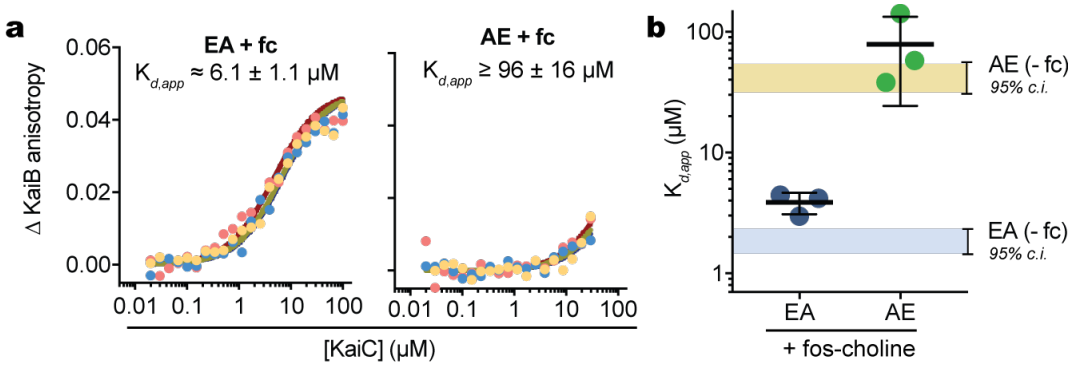

Fig. 3.2. Structural and biochemical analysis of KaiC-AE in the presence of *fos*-choline.

A) Equilibrium binding assays of nighttime and daytime KaiC at 4 mM *fos*-choline. Triplicate measurements are shown in red, yellow, and blue. Darker lines indicate best fit to the Langmuir isotherm as described in Methods. **B**) Values for $K_{d,app}$ extracted from binding assays with *fos*-choline are reported as mean values from n = 3 independent titrations with with error bars representing standard deviation. 95% confidence intervals from experiments done without *fos*-choline from **Fig. S1** are shown for comparison.

For the nighttime phosphomimetic, single-particle analysis also returned an additional distinct map with both the CI and CII rings resolved (**Fig. 3.3A**) in a novel C_2-symmetric structure that was resolved to ~3.2 Å. This new subpopulation of KaiC hexamers has a widened central pore (**Fig. 3.3B-C**), coupled with accumulation of ADP at two of the six CII-CII interfaces (**Fig. 3.4C-D**) opposite each other in the hexameric ring. KaiC protomers adjacent to these sites adopt a 'compressed' conformation that brings the CI and CII domains together (**Figs. 3.3A, 3.5A**), whereas the other four protomers remain in the extended conformation. It should be noted that C_2-symmetry is apparently rare in hexameric AAA+ proteins, with only a few other examples having been reported to date (*149-151*). In contrast to these previously

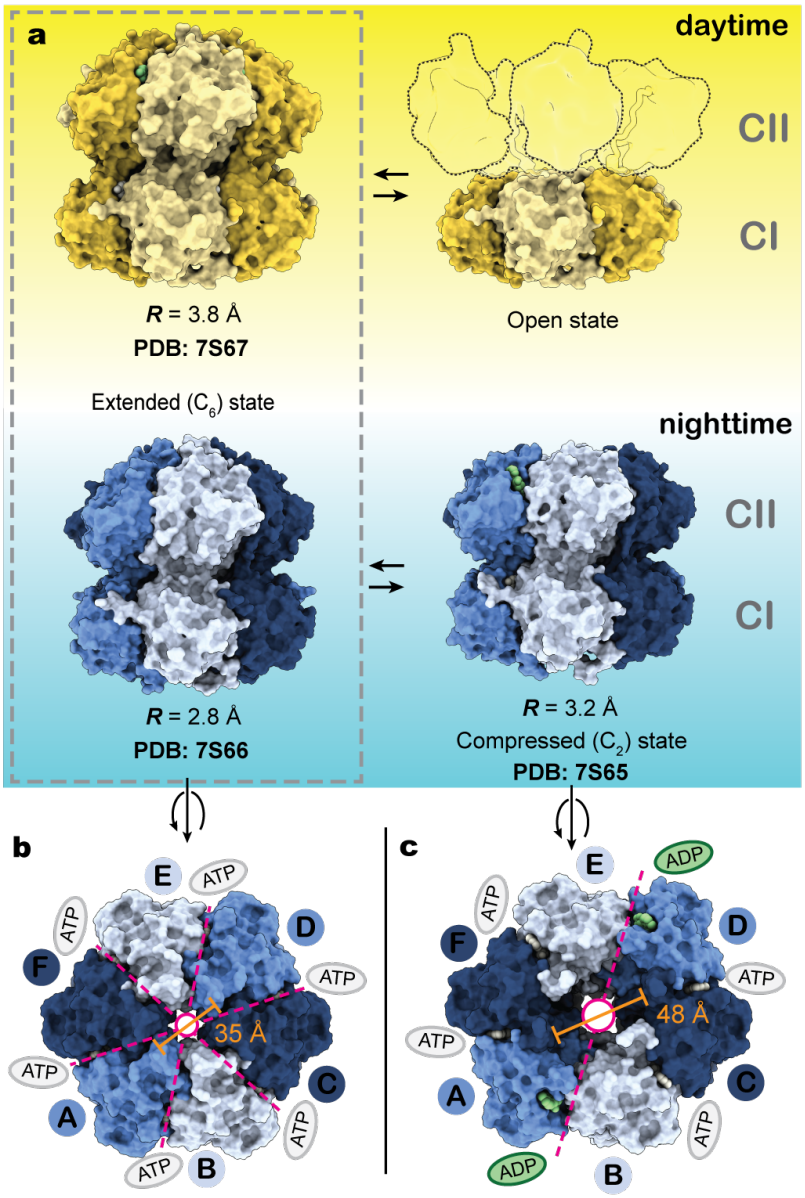

Fig. 3.3. Overview of 3-dimensional models obtained for daytime and nighttime KaC variants

A) Space-filling depictions of daytime and nighttime KaiC conformations observed by cryo-EM. The 'open' daytime state is depicted with outlines to represent the destabilized CII protomers as rigid bodies flexibly tethered to the visible CI hexamer. **B**) Axial view of the extended and compressed (**C**) nighttime KaiC hexamers, viewed from the CII side. Dashed lines indicate the axes of symmetry with colored ovals denoting nucleotide state in the CII ring. Pore diameters are reported as measured between C_α atoms of V433 on A and D protomers.

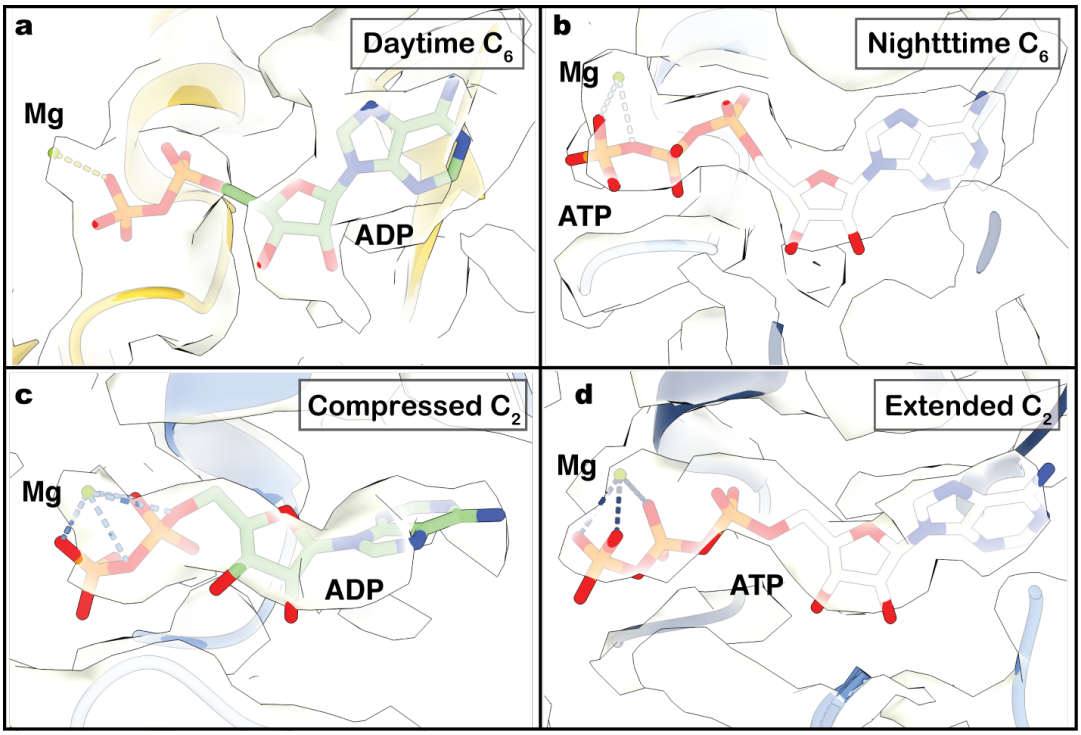

Fig. 3.4. CII nucleotide state in extended and compressed KaiC structures. **A**) Electron volume and atomic model for CII nucleotide in the KaiC-AE structure determined in the presence of 4 mM *fos*-choline, **B**) the C_6-symmetric KaiC-EA structure and **C**) extended or **D**) compressed subunits of the C_2-symmetric nighttime KaiC structure.

described 'dimer of trimer' states that each exhibit apo nucleotide pockets at their seam protomers (**Fig. 3.6**), the C_2-symmetric state of KaiC is unique in having its seam protomers occupied by ADP, suggesting that nucleotide binding on CII is an important regulator of CI-CII communication.

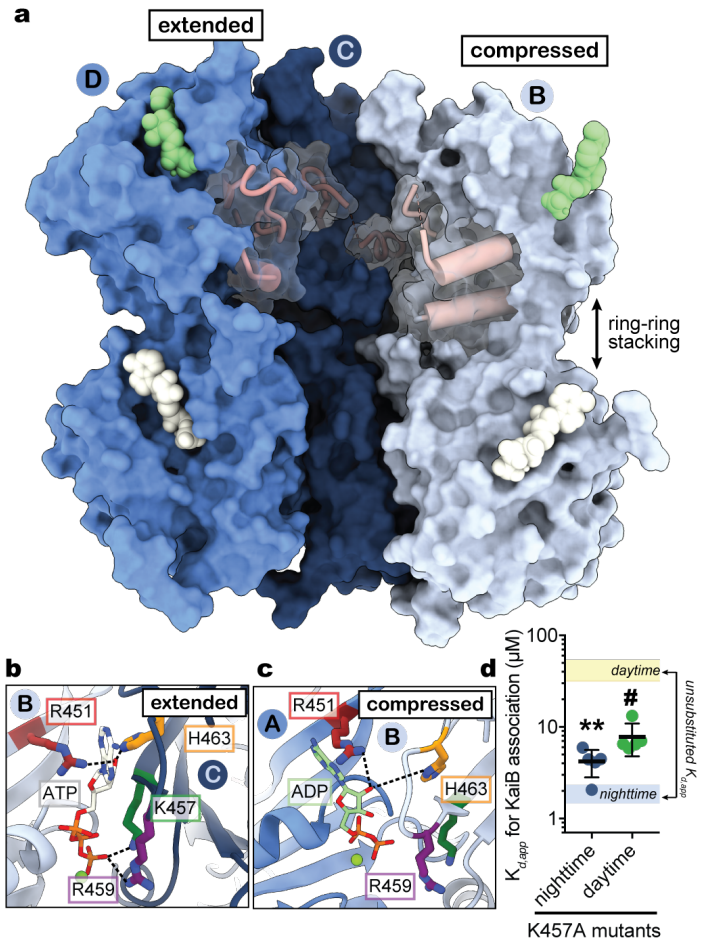

Fig. 3.5. Nucleotide interactions at CII-CII interfaces govern the transition between extended and compressed conformations.

A) Surface representation of KaiC protomers B, C, and D in the C_2-symmetric hexamer with CII-α8 and CII-α9 depicted as pink cylinders. Three subunits (A, E, and F) have been removed to view inside the hexamer. ATP nucleotides are depicted as white surfaces, and ADP in green. **B-C**) Close-ups of the CII nucleotide interface in the (panel **B**) extended and (panel **C**) compressed KaiC protomers. **D**) $K_{d,app}$ for the interaction of KaiB with daytime (green) and nighttime (dark blue) KaiC variants the bearing K457A mutation. Black lines and error bars represent mean ± sd from n = 5 independent titrations. Colored bars representing the 95% confidence interval for analogous measurement on KaiC phosphomimetics without the mutation are provided for comparison. Symbols (#, $P < 0.0001$; **: $P < 0.01$) represent the results of 2- sided unpaired parametric t-tests comparing each mutant to its respective unsubstituted phosphomimetic. Mean $K_{d,app}$ ± sd is 7.3 ± 1.9 μM for daytime KaiC-K457A and 4.6 ± 1.8 μM for nighttime KaiC-K457A.

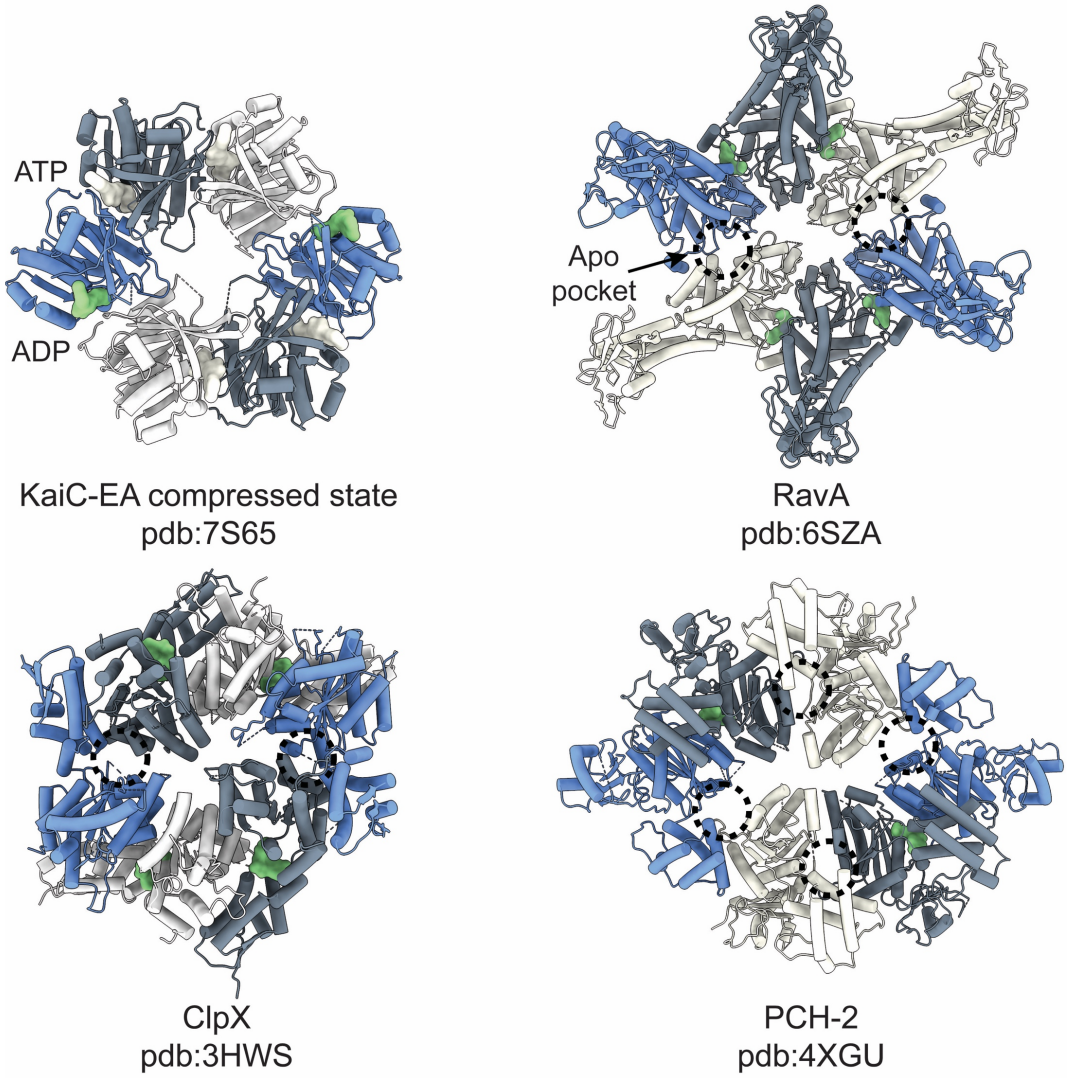

Fig. 3.6. Structural comparison of C_2-symmetric ATPase structures.

Seam protomers are depicted in blue while ATP and ADP nucleotides are shown in white and green, respectively. Apo nucleotide pockets are indicated with dashed circles. While other C_2-symmetric ATPases are unliganded at their seam protomers, KaiC is ADP-bound at these subunits.

Another feature of the C_2-symmetric state we observed is the loss of A-loop interactions within the central pore of CII, driven by disruption of interactions across

the compressed CII protomer interface (**Fig. 3.7A**). To test whether these interactions influence catalytic activity on CII, we measured the phosphorylation state of several KaiC mutants in this region (**Fig. 3.7B-C**). We found that the E444S mutant, which disrupts the hydrogen bond between the sidechain of E444 and the backbone amide of I490, significantly upregulated KaiC autophosphorylation in the absence of KaiA, similar to a prior study where an E444D mutation also resulted in constitutive hyperphosphorylation of KaiC (*34*). Our observation of coupling between A-loop conformations across the hexamer in our C_2-symmetric structure of nighttime KaiC suggests that coupling could also exist across KaiC protomers during the day, possibly explaining why only sub-stoichiometric levels of KaiA are needed to maintain robust oscillations (*111*).

3.4 Role of the compressed state in KaiB association

These observations raise the question: how does ring compression influence KaiB association? In the extended KaiC protomers of both the C_6 and C_2-symmetric structures, the sidechains of residues K457 and R459 interact directly with the γ-phosphate of ATP (**Fig. 3.5B**). However, contact with these sidechains is lost at the ADP-occupied CII interfaces (**Fig. 3.5C**) and the CII domain on the compressed protomer breaks away from the adjacent CII interface. Computational studies have highlighted the importance of nucleotide interactions at CII interfaces on the global conformational dynamics of KaiC (*146*). Given the apparent coupling between CII nucleotide interactions and the configuration of *cis*-interacting domains in the

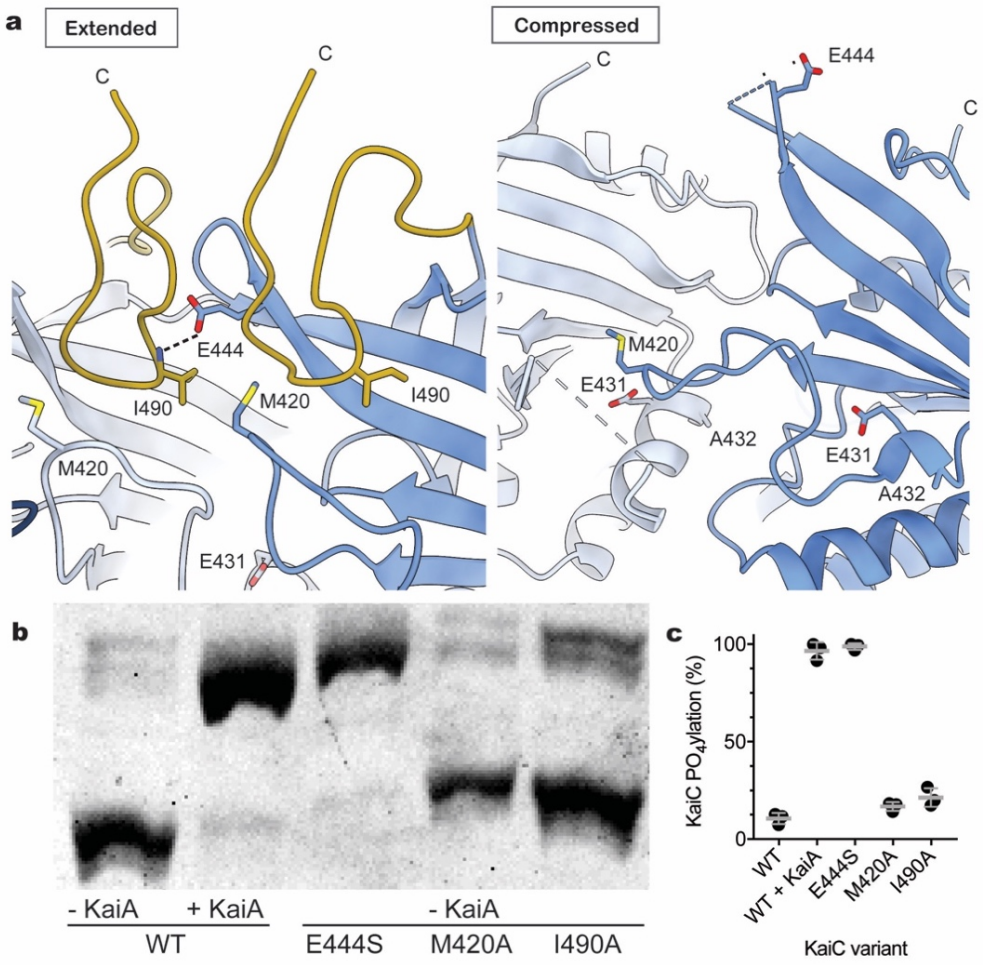

Fig 3.7. Allostery about the CII ring regulates KaiC autophosphorylation.

A) In the expanded state, the A-loop of an adjacent protomer (yellow) is positioned near the phosphosite-adjacent 422-loop through a hydrophobic interaction between I490 and M420. E444's sidechain forms a hydrogen bond with the mainchain nitrogen of I490 in *trans*. In the compressed state of KaiC-EA, E444 in the ADP-bound protomers is positioned away from the pore and no longer stabilizes the A-loops, allowing them to become disordered and causing the 422-loops to collapse towards phosphosite-containing α9. Binding of KaiA to the C-terminus of KaiC may disrupt this tripartite interaction and stimulate hyperphosphorylation. **B**) Sypro orange fluorescence of KaiC mutants that were run on a 10% denaturing polyacrylamide gel containing 50μM Phos-tag^{TM} reagent and 100μM Mn^{2+}. **C**) Densitometric analysis of bands corresponding to phosphorylated and unphosphorylated KaiC. Gray bars represent mean ± standard deviation for n = 3 repeats.

compressed protomers, we hypothesized that introducing an alanine residue in place of K457 would make this state accessible to the daytime variant to enhance KaiB association. Consistent with our prediction, the K457A mutation resulted in a ~6-fold increase in KaiB affinity for daytime KaiC (**Figs. 3.5D**), showing that KaiB association is bolstered by mutations that promote the compressed conformer in the daytime state. Furthermore, a modest loss of affinity was also observed in the nighttime K457A variant, suggesting that the extended conformations observed in the C_2-symmetric structure, which are stabilized by K457 interactions, also play a role in efficient KaiB association.

These changes in CII nucleotide state and associated 'breaking away' of the CII-CII interface resulted changes to secondary structure in the compressed protomers of C_2-symmetric KaiC structure. In particular, the CII-α9 helix, where the phosphomimetic-substituted autophosphorylation sites are located, comprises only a single turn in the extended protomers (**Fig. 3.8A**), but was lengthened in the ADP-bound, compressed protomers (**Fig. 3.8B**). When we inhibited this helical elongation by mutating I430 to glycine, we observed a ≥50-fold decrease in KaiB affinity (**Fig. 3.8C**), demonstrating that KaiB association is dependent on helix extension near the CII autophosphorylation sites.

Lengthening of CII-α9 resulted in translocation of the nearby CII-α8 helix toward the CI-CII interface about 5 Å in our compressed KaiC structure (**Fig. 3.8D**). This is notable because a recent study identified the CII-α8 residue Tyrosine 402 as a

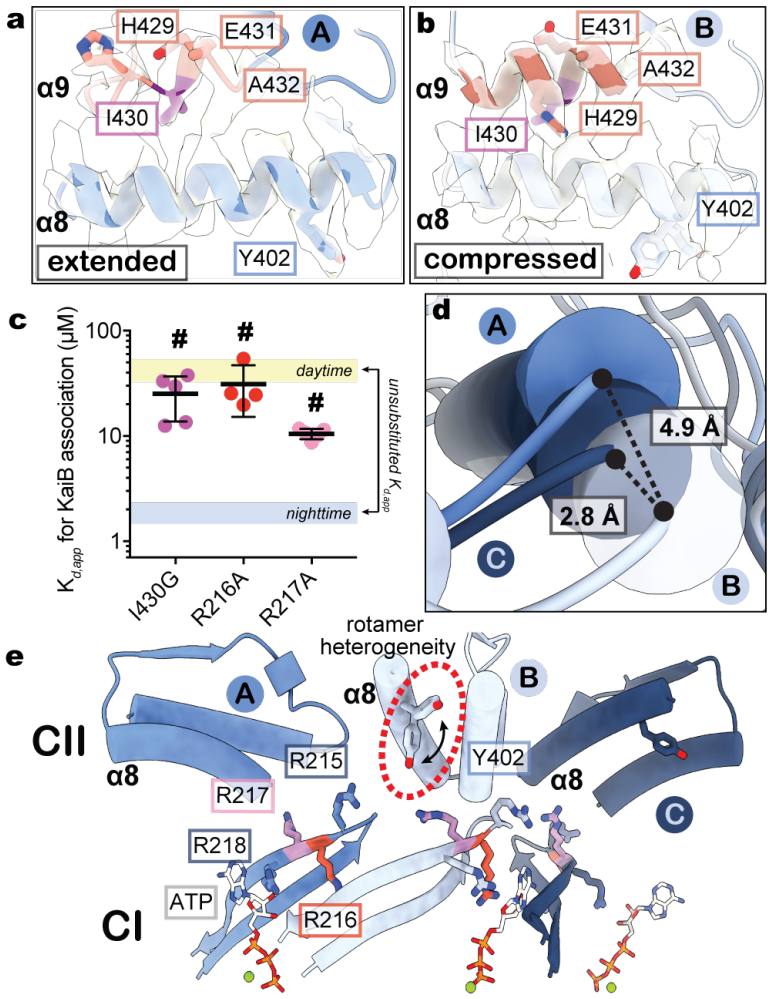

Fig. 3.8. Compression of the *cis* CI-CII interface primes nighttime KaiC for KaiB association.

A-B) EM density and atomic models for residues S424 through T434 (pink) and CII-α8 helices in extended (**A**, contour = 0.0343) and compressed (**B**, contour = 0.0307) protomers of the C_2-symmetric state of KaiC-EA. **C**) KaiB affinity for nighttime KaiC with variants with mutations\s of CII-α9 or arginine tetrad. Line and error represent mean ± standard deviation for n = 5 (n = 4 for R216A) measurements. Symbols represent one-way ANOVA (#, $P < 0.0001$) with Dunnett's multiple comparisons for each mutant against nighttime KaiC. Mean $K_{d,app}$ is ≥ 25 ± 12 μM (I430G), ≥ 25 ± 4 μM (R216A) and ≥ 13 ± 4 μM (R217A) for the nighttime KaiC mutants. **D**) Cylinder depictions of the CII-α8 helices from the three unique protomer conformations of the compressed hexamer, aligned about their CI domains. **E**) Proximity of CII-α8 to the arginine tetrad in the C_2-symmetric state.

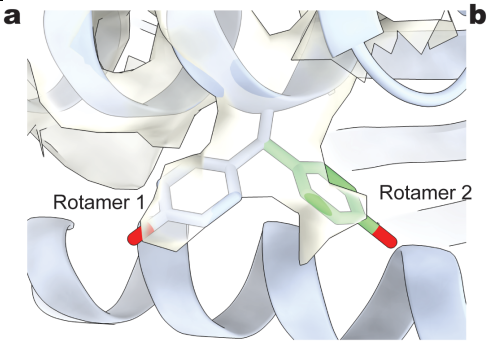

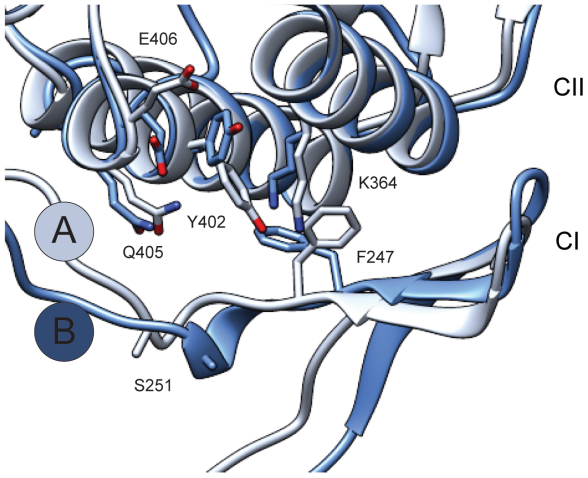

	Rotamer 1	Rotamer 2
Rotamer probability	43 %	34 %
Residue Model vs. Data CC (Phenix)	0.74	0.65

Fig 3.9. KaiC residue Y402 exhibits rotameric heterogeneity in the compressed conformation.

A) Close-up view of the two Y402 rotamer conformations from the compressed protomer of the C_2-symmetric KaiC-EA structure. Cryo-EM density is depicted in white and semi-transparent for clarity. Analysis from the modeling software Coot[59] indicates that both rotamers are allowed with similar probabilities. Model vs. Data Cross Correlation in Phenix[60] indicates that Rotamer 1 has a higher correlation compared to Rotamer 2, but that both are favorable. **B**) Superposition of compressed protomer B with expanded protomer A, aligned by the CII domain. The rotameric heterogeneity of Y402 in the compressed protomer is associated with rotameric deviations in nearby residues in comparison to an expanded protomer.

key regulator of timing in KaiC (*99*), with mutants at this position exhibiting extreme changes in CI ATPase activity and correlated *in vivo* circadian period (e.g., 15 hours to >6 days). Strikingly, we observed EM density for distinct rotamer conformations of Y402 only in the compressed protomers (**Figs. 3.8E, 3.9**) situated near other period-determining residues on the linker connecting CI and CII (*39*), indicating that period regulation by Tyrosine 402 likely occurs through dynamic interactions at the CI-CII interface.

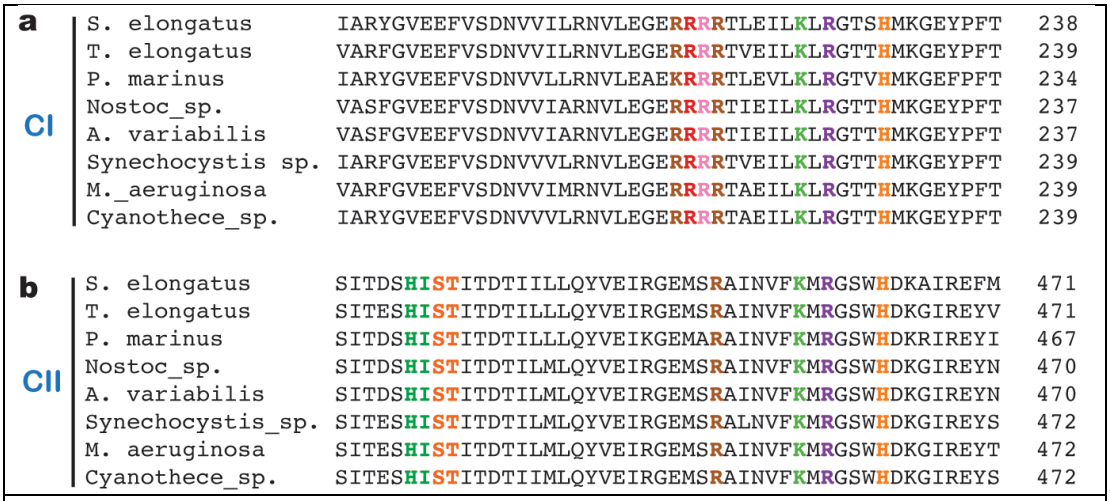

Fig. 3.10. Multiple sequence alignment of key KaiC regions from various species of cyanobacteria.

A) Protein sequences of the CI and **B**) CII regions of KaiC from eight distinct strains of cyanobacteria. Sequences are presented with each domain grouped to together and aligned amongst the species, and also aligned about the CI and CII domains within a given protein sequence. Key residues are highlighted with colors illustrating their conservation between the CI and CII domains.

Translocation of CII-α8 via C_2-symmetric ring compression appears to regulate the biochemical activity of CI via four sequential, highly conserved arginine residues in the CI domain known as the 'arginine tetrad' (**Figs. 3.8E, 3.10 and 3.11A**) (*141*). These residues are essential for circadian rhythms and form a network of electrostatic interactions that join each CI protomer to both clockwise and counter-clockwise neighbors (**Fig. 3.11B-C**) (*40, 141*). This nexus of KaiC regulation is situated between the CI and CII domains at the tip of the CI-β9 hairpin that leads directly into the nucleotide binding pocket of CI (**Fig. 3.11B**), where enzymatic activity is required for KaiB association (*28*). We measured KaiB binding for several alanine mutants within the arginine tetrad and found that affinity was reduced by >10-

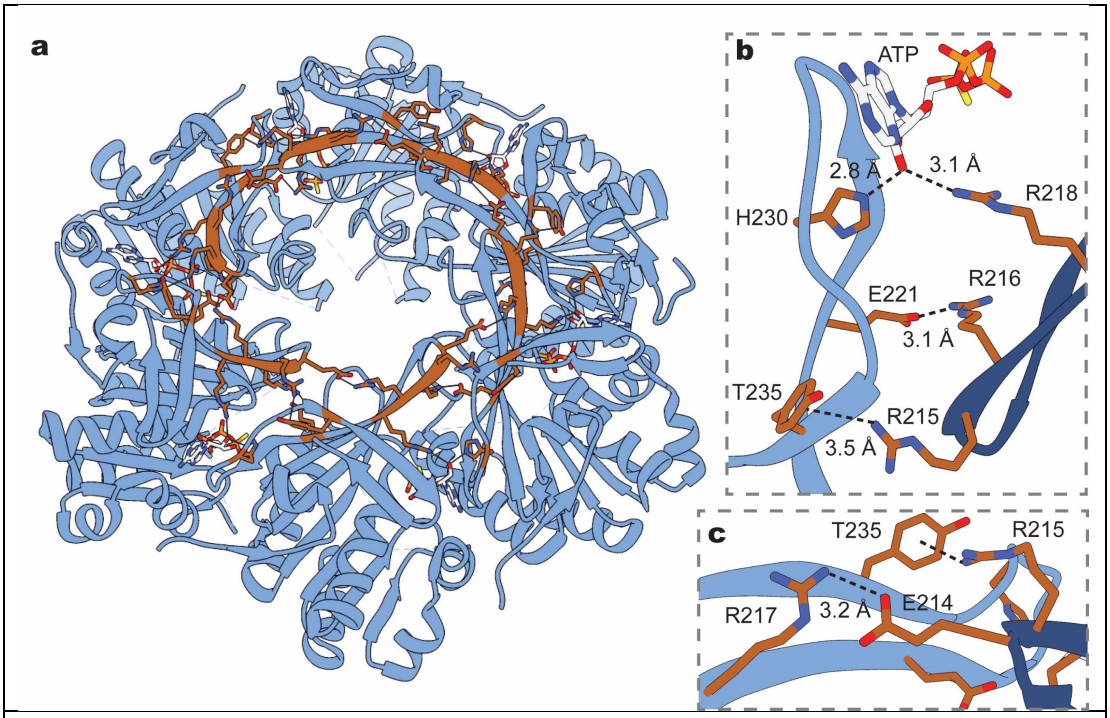

Figure 3.11. The arginine tetrad creates a network of CI-CI *trans* interactions.

A) Crystal structure (PDB 4TL8[39]) is shown as light blue ribbons with the P-loops displayed in darker blue. Arginine tetrad sidechains at clockwise (**B**) or counterclockwise (**C**) subunits as well as their electrostatic interaction partners are shown in brown. Average interatomic distance from the six interfaces are shown.

fold for R216A (**Fig. 3.8C**) and by ~6-fold for R217A, highlighting the importance of interdomain interactions in this region for KaiB association.

3.5 Transduction of phosphostate information throughout CI

The cooperative nature by which KaiB monomers are recruited to the KaiC hexamer is well established (*56, 70, 100, 104*). Given that the arginine tetrad is structurally poised to facilitate both *cis* and *trans* protomer regulation, we next wondered if the KaiC-R217A mutant would influence this cooperativity. To assess

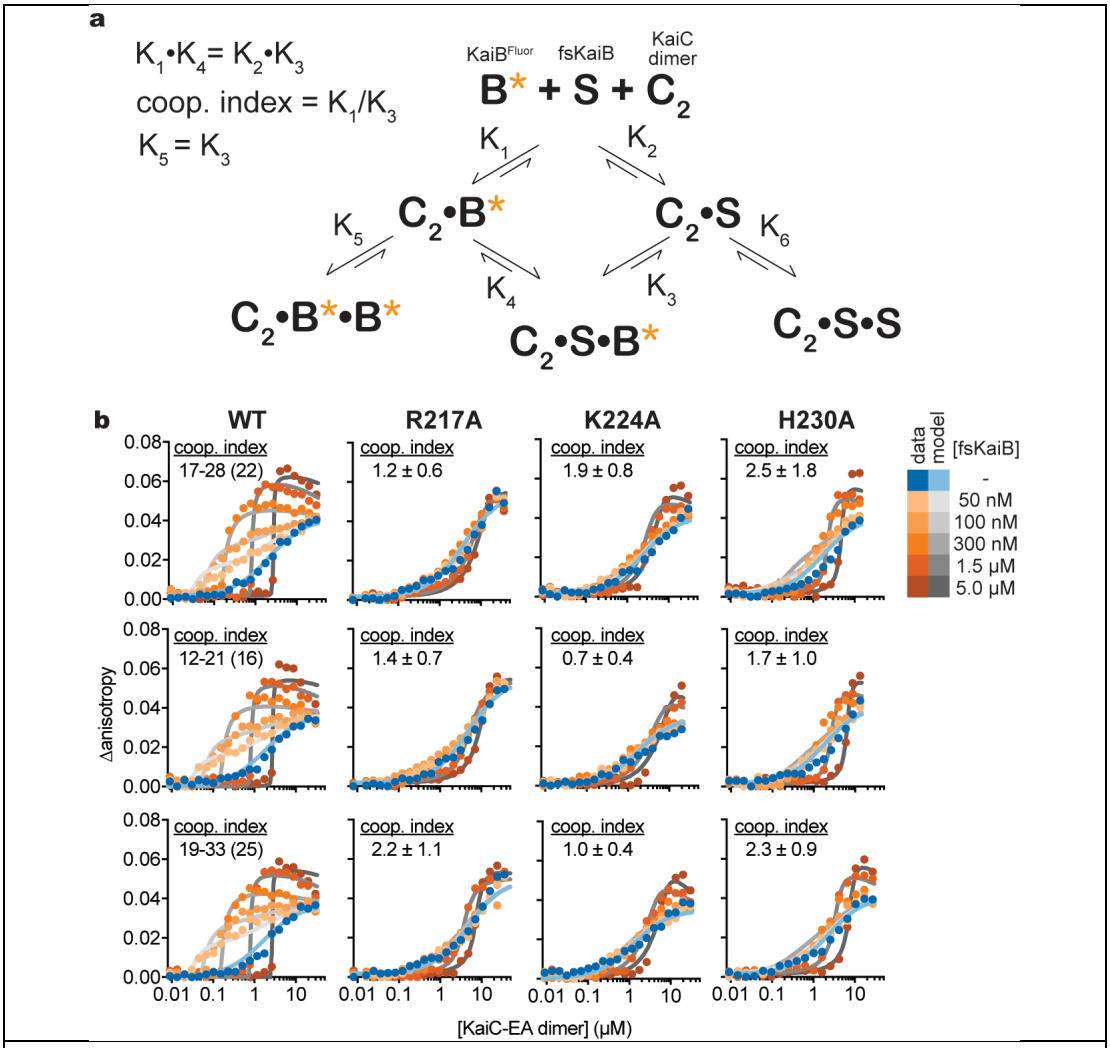

Fig. 3.12. Cooperativity analysis of KaiC mutants.

A) Thermodynamic model, based on the one originally derived for heterotropic cooperativity in Chavan *et al.*(*152*) In this case, the heterotropic cooperativity factor, S, is replaced with the homotropic factor represented by unlabeled KaiB-I87A (fsKaiB), which binds much tighter to KaiC than wild-type KaiB.(*37*) Wild-type KaiB is monitored, as indicated by an orange asterisk. **B**) 2-dimensional titrations are overlaid with titration curves derived from least-squares fitting of the data from each individual dataset. For unsubstituted (WT) KaiC-EA, the 95% confidence intervals from n=1000 Monte Carlo simulation is reported. These represent the n = 25 and n = 975 values from the simulation, which gave median (n = 500) values of 22, 16 and 25 (top panel to bottom panel). For each 2D-titration of the mutant nighttime KaiC variants, best fit cooperativity indices from least-squares analysis are reported as best fit ± standard error. See methods for more information on how these values and standard errors were determined.

this, we updated our method for quantifying KaiB cooperativity (*104*) to reflect the intrinsic homotropic cooperativity when unlabeled KaiB-I87A, often referred to as fold-switched or fsKaiB, is used to stimulate cooperative association of fluorescently labeled wild-type KaiB in KaiC binding assays (**Fig. 3.12A**). Using this approach, we measured a KaiB cooperativity index of ~21 ± 2 for KaiC-EA (**Figs. 3.13A, 3.12B**) using fsKaiB as a secondary titrant in KaiC affinity assays.

Because wild-type KaiB takes on the structure of fsKaiB when associated with KaiC (*36, 37, 51*), we can interpret this as a ~21-fold affinity enhancement for the subsequent association of KaiB after the first KaiB molecule binds to the hexamer. Strikingly, the R217A mutant showed a severe reduction of the cooperativity index (~1.6 ± 0.5), suggesting that the arginine tetrad is essential not only for communication between CI and CII domains in *cis*, but that *trans* protomer communication must also run through this conduit. Another arginine tetrad residue, R218, interacts directly with the 2' hydroxyl of the nucleotide at CI-CI interfaces, which is sandwiched between protomers by hydrogen bonds to R218 and H230 (**Figs. 3.13B, 3.14**). To test whether this nucleotide-mediated CI-CI interaction is important for KaiB association, we substituted H230 with alanine, and observed significantly diminished cooperativity (**Fig. 3.13A**), as well as about a 4-fold reduction in overall affinity for KaiB (**Fig. 3.13C**), demonstrating that the CI-CI interactions must traverse both the arginine tetrad and the nucleotide binding pocket for efficient KaiB association.

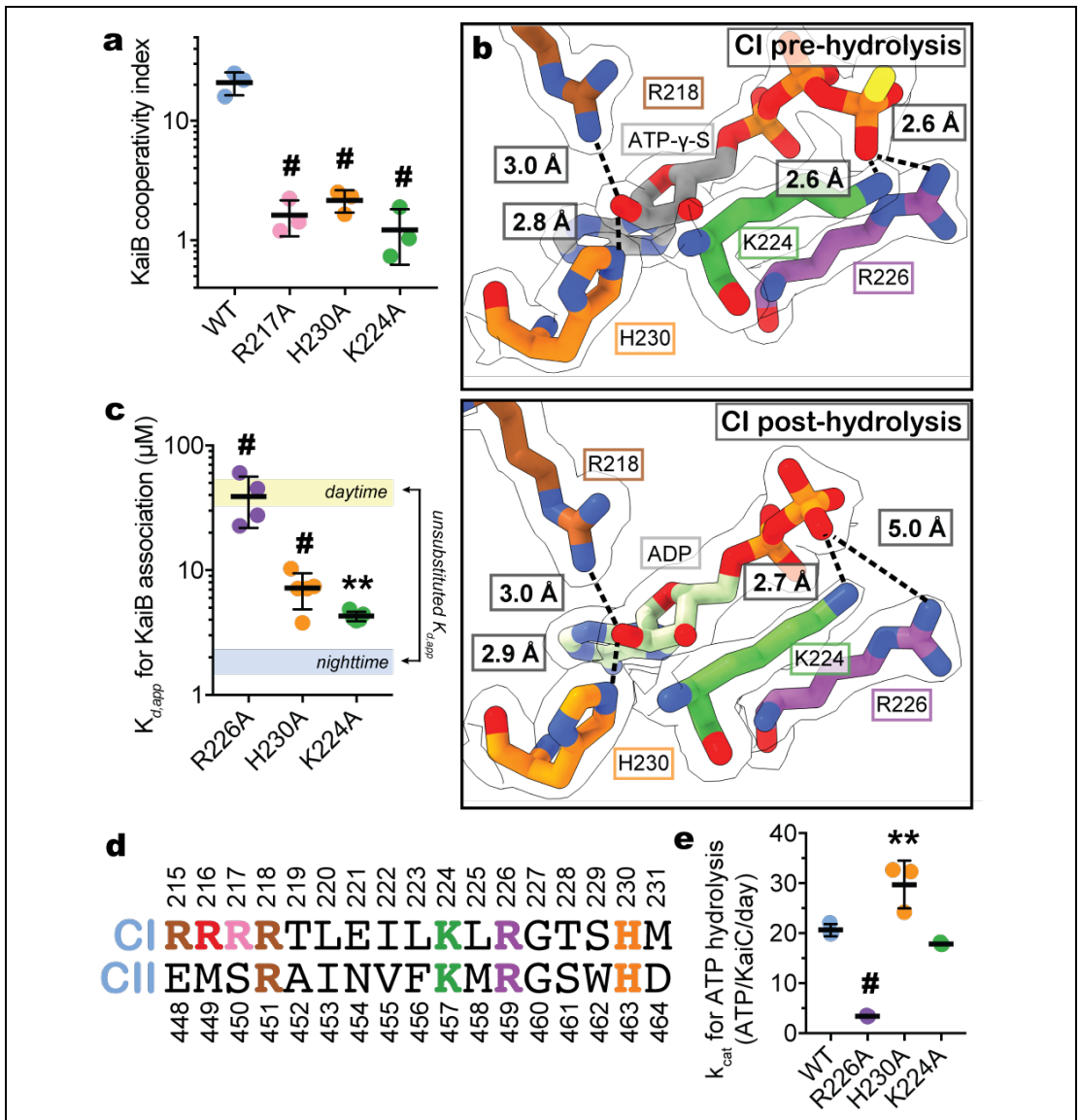

Fig. 3.13. Interactions in the CI nucleotide binding pocket link ATP hydrolysis to cooperative KaiB recruitment.

A) Cooperativity indices for nighttime KaiC variants determined with fsKaiB as secondary titrant Lines and errorbars represent mean ± sd for n = 3 independent titrations. Symbols represent one-way ANOVA (ns, not significant; **: $P < 0.01$; #, $P < 0.0001$) with Dunnett's multiple comparisons to unsubstituted nighttime KaiC. **B**) Atomic models and electron density (F_c-F_0, σ = 0.21) for nucleotide interactions from the pre-hydrolysis (PDB 4TL8, top) or post-hydrolysis (PDB 4TLA chain C, bottom) CI domain crystal structures.(*40*) **C**) KaiB binding affinity for nighttime KaiC active site mutants. Lines and error bars represent mean and sd from n = 4 (n = 5 for K224A) independent titations. Symbols represent statistical analysis

identical to that described for (**A**). Mean $K_{d,app}$ values are 5.9 ± 1.5 μM (H230A), ≥ 38 ± 18 μM (R226A) and 4.6 ± 0.3 μM (K224A). **D**) Alignment of CI and CII protein sequences from *S. elongatus*. **E**) Turnover rate constants (k_{cat}) for ATP hydrolysis by KaiC-EA variants. Lines and error bars represent mean values ± sd with statistical analysis as described for (**A**).

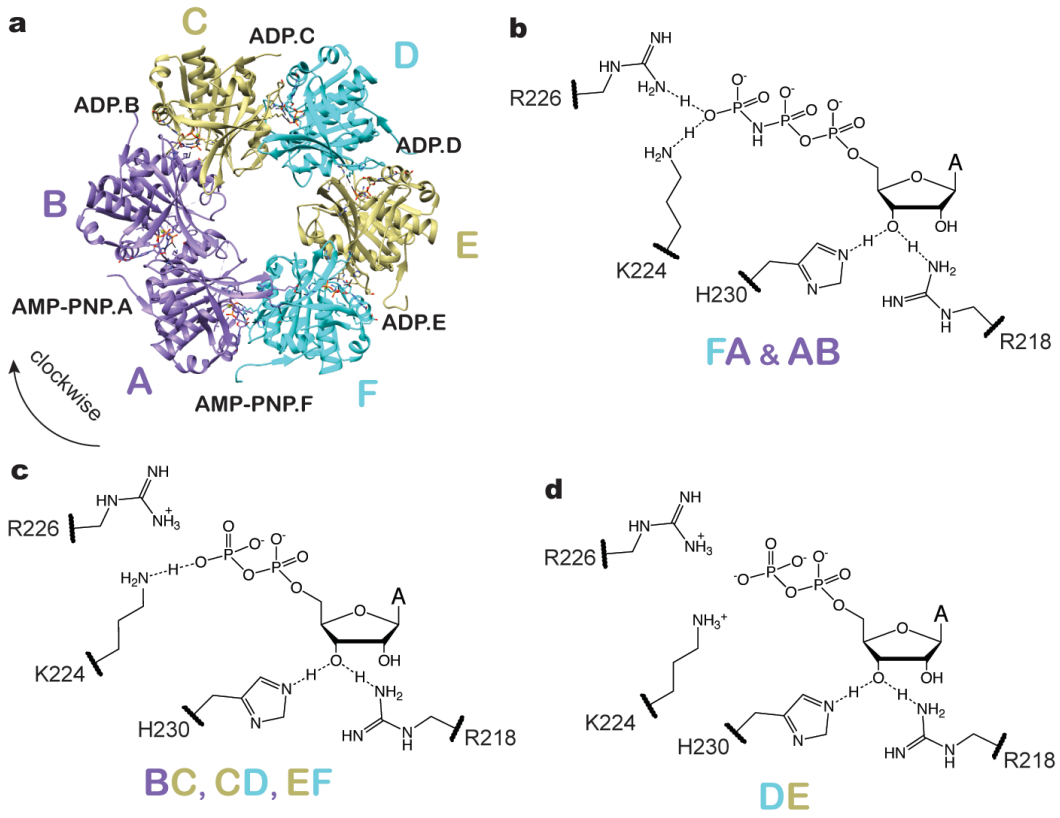

Fig. 3.14: Analysis of CI-CI nucleotide contacts from PDB 4TLA.

A) Top-down view of the CI domain from the mixed nucleotide state CI structure reported in Abe et al.[39] with the nucleotides observed at each interface labeled. Schematic depictions of the specific atomic interactions with the 2' hydroxyls as well as residues K224 and R226 observed at each interface exhibiting either two (**B**), one (**C**) or no (**D**) electrostatic interactions with the nucleotide phosphates.

It should be noted that the overall architecture of the nucleotide binding pocket is strikingly well-conserved between the CI and CII domains of KaiC and is nearly invariant in KaiC across cyanobacteria (**Figs. 3.13D and 3.10**). Residues R215, R216 and R217 of the arginine tetrad are unique to CI, indicative of their role

in CI-CII and CI-CI interdomain regulation in KaiC. However, CI residues R218 and H230 have analogs in CII, R451 and H463, that play similar structural roles leading to *trans* CII-CII interdomain interactions between protomers that bridge the nucleotide (**Fig. 3.5B**). Furthermore, CI and CII domains also contain a conserved lysine/arginine pair (K224 and R226 in CI, K457 and R459 in CII) near the nucleotide binding site. Given the importance of nucleotide interactions we observed in the CII domain, we revisited the atomic resolution structures of CI hexamers previously reported by Abe et al. (*40*) In these structures, K224 changes its orientation to coordinate the ultimate nucleotide phosphate at both pre- and post-hydrolysis CI-CI interfaces (**Figs. 3.13B**, **3.14**), whereas R226 coordinates nucleotide only in the ATP-bound state, playing a catalytic role in ATP hydrolysis (*40*).

Given the importance of K457 in nucleotide-mediated CII-CII interactions and KaiB affinity, we next set out to explore the functional role of the analogous CI residue, K224, and its neighboring residues R226 and H230 in more detail. To determine how these mutations influence CI ATP hydrolysis, we measured the enzymatic turnover rate (k_{cat}) of alanine substitution mutants at residues R226, K224, and H230 (**Figs. 3.13E, 3.15**). As expected, the R226A mutation significantly decreased both ATPase activity and KaiB affinity, similar to other catalytically dead variants (*28*). The H230A mutant exhibited increased ATPase activity which, combined with its diminished affinity for KaiB, shows that ATPase activity and KaiB binding are not simply correlated in a linear fashion. Notably, the K224A mutant had

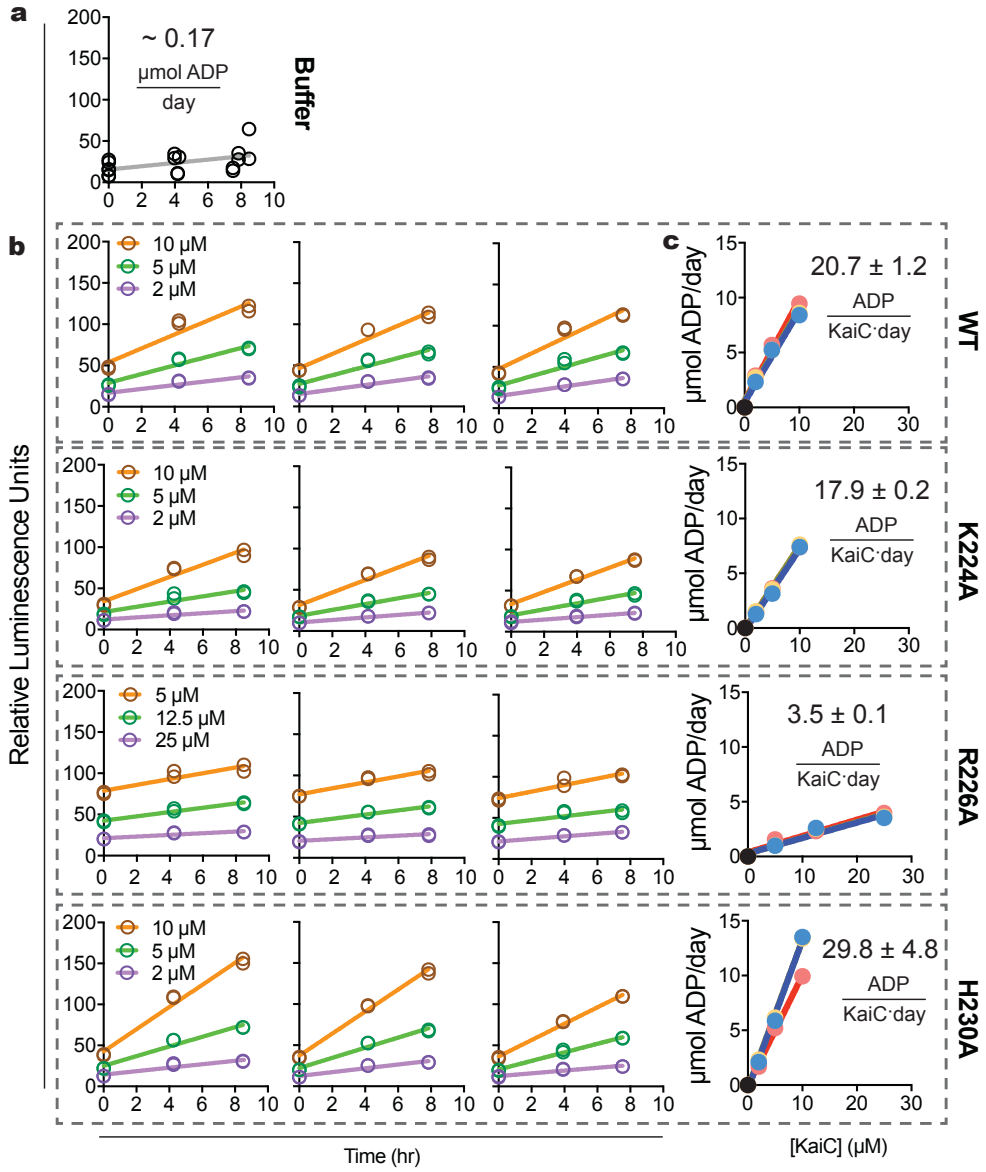

Fig. 3.15. ATPase Assays.

A) Triplicate trajectories of luciferase signal in ADP-Glo assays for background ATP hydrolysis from buffer alone, fit to a single regression line giving an overall rate of 0.17 μmol/day. **B**) Luminescence trajectories of KaiC-dependent ATP-hydrolysis monitored by ADP-Glo at three concentrations of KaiC-EA. **C**) Turnover rate constants (k_{cat}) were subsequently extracted from the slopes of the KaiC trajectories (red, yellow, and blue for replicate measurements) plotted against the concentration of the KaiC-EA variant, using the buffer rate as the zero point (black).

minor reductions in both KaiB affinity and ATPase activity (**Fig. 3.13E**) despite its role in the coordination of the nucleotide phosphates in CI. Both the H230A and K224A mutations essentially eliminated the cooperative recruitment of KaiB to the KaiC-EA hexamer (**Fig. 3.13A**), demonstrating that interactions around the CI nucleotide are critical for KaiB recruitment to KaiC through *trans* regulation of the CI domain.

The coupling of CI ATPase activity to cooperative KaiB recruitment could impart a switch-like nature to the assembly of this critical protein complex—a function that has been proposed for other RecA-like AAA+ proteins (*153, 154*). To assess the functional consequences of disrupting KaiB cooperativity, we set up *in vitro* oscillator reactions with the K224A or H230A KaiC mutants in the presence of KaiA and KaiB, and observed that both mutations resulted in a total loss of biochemical rhythms (**Fig. 3.16A**). This severe phenotype could potentially be explained by decreases in the affinity of KaiB for KaiC, though KaiC-EA K224A showed only a two-fold decrease in affinity, and weak rhythms would have been expected to persist (*104, 111*).

We recently reported that decreasing KaiB to sub-saturating concentrations just below its $K_{d,app}$ significantly reduced the amplitude of oscillations *in vitro,* but that rhythms could be rescued by the clock protein SasA, which uses heterotropic cooperativity to stimulate KaiB binding to KaiC (*104*). The concentration of KaiC *in vivo* has been estimated at 6 ± 1 μM (*63*), and KaiB is present at roughly twice that (*96*); however, marked changes in the sub-cellular localization of clock proteins

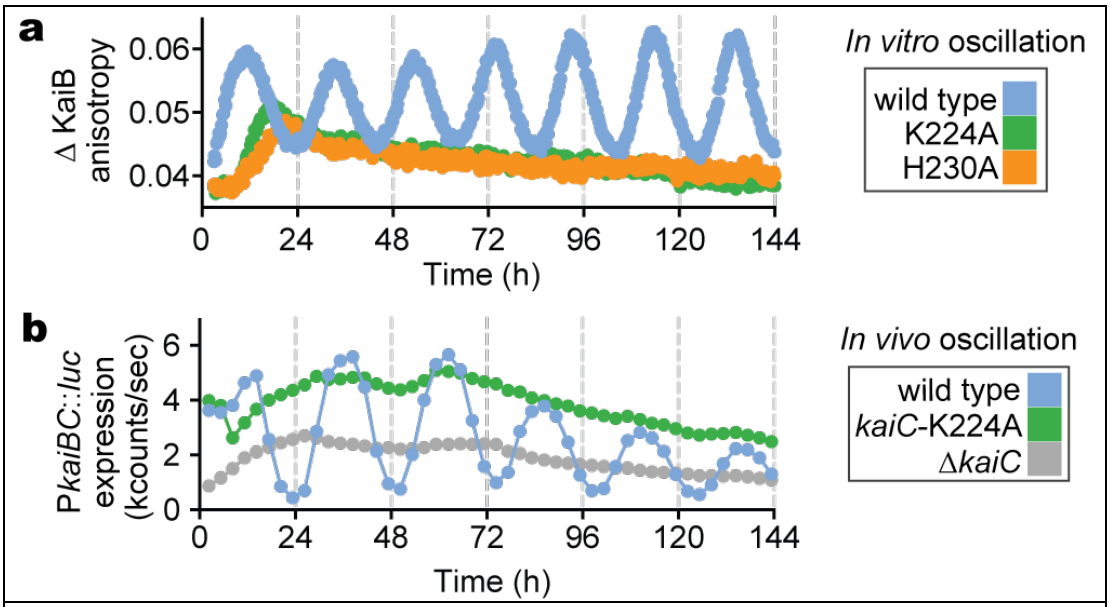

Fig 3.16. Functional characterization of CI active site mutants.

A) Representative *in vitro* oscillation reactions of KaiC in the presence of KaiA and KaiB measured by fluorescence polarization anisotropy of labeled KaiB (n = 3). **B**) Representative bioluminescence time courses from a luciferase reporter gene driven by P*kaiBC* in *S. elongatus* cultures entrained under 12-h light/dark cycles for 48-hr and subsequently allowed to free-run in constant light (n = 6).

throughout the day (*71*) could alter their local concentrations to influence clock protein assembly. Therefore, we introduced the K224A mutation into KaiC in *S. elongatus* using CRISPR/Cas12a and found that this KaiC variant could not support circadian rhythms *in vivo* (**Fig. 3.16B**). Therefore, no cellular factors can compensate for the modest reduction in KaiB affinity and loss of CI nucleotide sensing, demonstrating that *trans* regulation of the CI domain through K224 is essential for circadian rhythms.

CI ATP-hydrolysis is required for KaiB association (*28*) and ADP-bound CI interfaces have been observed in all KaiB-bound KaiC structures solved to date (*37, 51*). However, we did not observe ADP-bound CI domains in our cryo-EM structures

of isolated KaiC, suggesting that the phospho-dependent regulation of KaiB association by CII does not occur by simply trapping the ADP-bound state in CI prior to KaiB association. Rather, we propose that ADP is replaced with ATP after hydrolysis unless KaiB association locks the CI domain into the post-hydrolysis state by inhibiting ADP release.

3.6 Discussion

This work provides an important mechanistic link between the daily phosphorylation cycle of KaiC and quaternary structural changes that mediate negative feedback in the cyanobacterial circadian pacemaker. Our cryo-EM studies on the daytime state corroborate prior solution studies that observed a destabilized CII ring in the S/pT phosphostate (*35, 43*),(*144*). These results suggest that the destabilized CII state lacks the ability to engage the CI domain in a way that is permissive for initial KaiB association, i.e., through the C_2-symmetric compressed state (**Fig. 7A**). Because the compressed state is important for KaiB association, we propose that both the dusk-like pSpT and nighttime pST phosphostates are able to take on this conformation, as our prior studies on a KaiC-EE (pS/pT) phosphomimetic showed a similar affinity and cooperativity of KaiB binding compared to the nighttime state (*104*). Our results therefore support a model where phosphorylation of S431 regulates the CI domain through elongation of the CII-α9

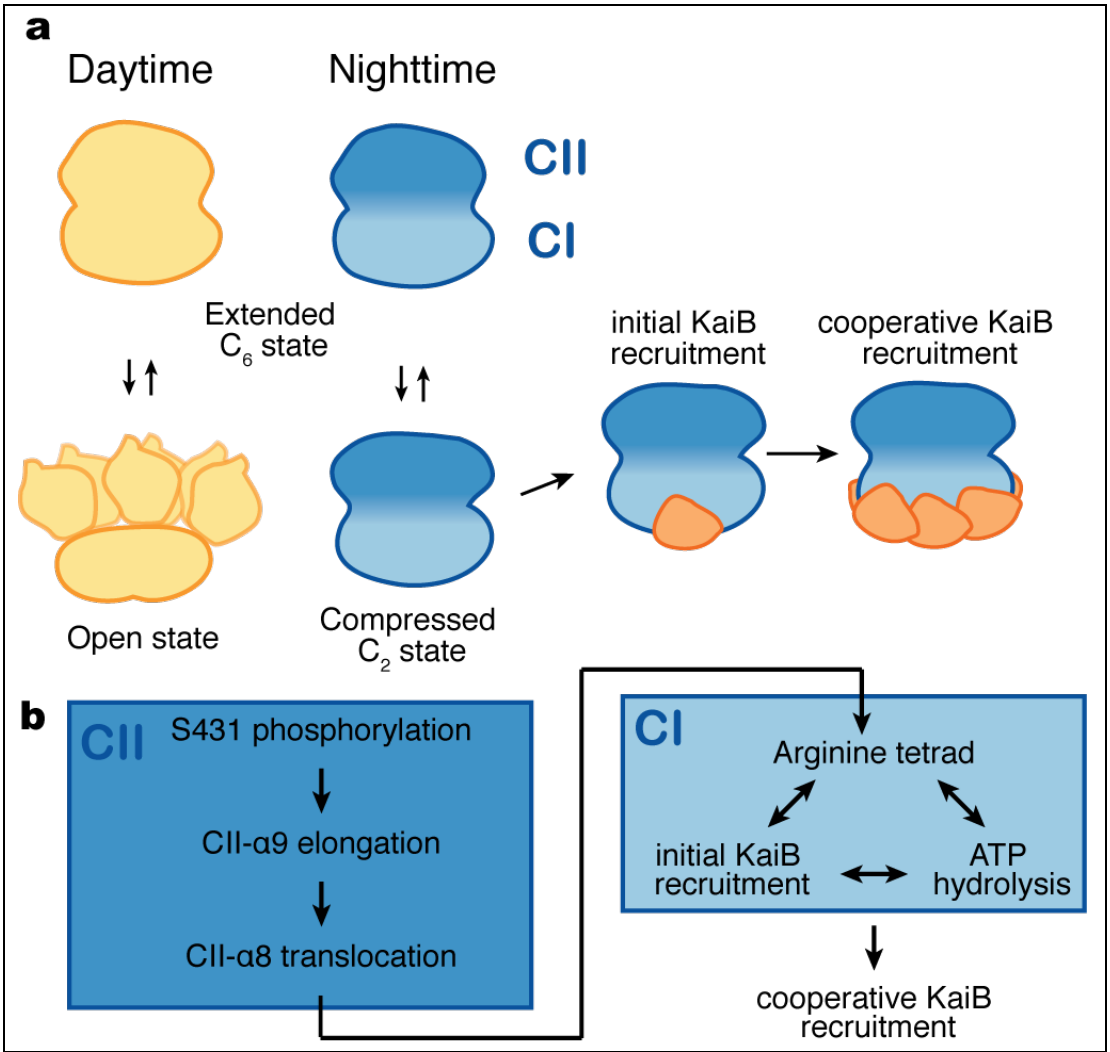

Fig. 3.17. Model for regulation of KaiB association by KaiC phosphostate.

A) Cartoon depiction of the KaiB association pathway. Daytime (yellow) and nighttime (blue) states of KaiC both adopt an extended C_6-symmetric ground state. During the day, the extended state is in equilibrium with an open state where the CII hexamer is destabilized relative to the CI domain. At night, excursions from the extended state result in a C_2-symmetric hexamer where two subunits of the CII domain are compressed to prime KaiC for KaiB association. An initial KaiB binding event takes place through this compressed intermediate to pave the way for cooperative saturation of the CI hexamer with KaiB molecules. **B**) Schematic depiction of the regulatory conduit through which the CI and CII domains communicate to regulate KaiB association according to clock phase.

helix, leading to *cis* domain compression and translocation of CII-α8 towards the arginine tetrad on CI (**Fig. 7B**). From there, dynamic interactions radiate down into

the CI active site, as well as to adjacent protomers, where ATP hydrolysis and CI nucleotide state are coupled with KaiB occupancy on both *cis* and *trans* CI domains. The fact that this occurs in the context of a C_2-symmetric intermediate further reinforces the cooperative aspect of this phenomenon, because the direct priming of KaiC for KaiB association occurs in concert for two protomers across the hexamer.

The presumptive role of KaiC-K224 in coupling of ATP hydrolysis to switch-like biochemical activity of KaiB binding bears a striking similarity to a recently reported 'arginine coupler' in the bacterial helicase loader DnaC (*154*). In this system, alanine substation of a positively charged amino acid just upstream of the arginine finger was found to increase ATPase activity, while being essential for the switch-like loading activity of DnaC. Notably, this motif is conserved in mammalian initiator ATPases (*154*). Our observation of a similar mechanism in KaiC in regulation of the cyanobacterial clock suggests that this may be an even more widespread design feature within the AAA+ family.

Although CI ATPase activity is correlated with circadian period *in vivo* and *in vitro* for many KaiC mutants (*39, 40, 99, 155*), no precise chemo-mechanical mechanism has yet been described to explain this. Our results, combined with crystal structures from the literature, demonstrate that the enzymatic cycle on CI is coupled

to the CII active site through a dynamic allosteric conduit involving the arginine tetrad and CII-α8. This could explain why the most extreme period-altering mutations in KaiC are located on CII-α8 or nearby in the linker that connects the CI and CII domains (*39, 99*). Mutations such as the Tyr402 substitutions reported by Ito-Miwa *et al.* likely alter interactions between the arginine tetrad and CII-α8 that couple CI-ATPase activity to the CII domain to give rise to such dramatic period effects. Together with the associated biochemistry, our structures identify the major waypoints in the allosteric pathway connecting the CI and CII domains, thus paving the way for a comprehensive understanding of the post-translational oscillator from both modeling and reverse-engineering perspectives.

3.7 Materials and Methods

Site-directed mutagenesis and protein expression/purification

All protein constructs were expressed from a kanamycin-resistant pET-28b plasmid with an N-terminal His-SUMO tag for affinity purification. Mutations were introduced by amplification of the whole vector, installing point mutations via primers using the method described by Liu *et. al* (*118*). KaiA and KaiB were purified as described previously (*35, 43*). KaiC constructs were expressed in BL21(DE3) cells (NEB). Cultures were grown in M9 medium under antibiotic selection to an optical density (λ = 600 nm) between 0.6 and 0.8 by shaking at 37°C, and were subsequently cooled to 18°C before induction with 200 μM IPTG and shaking overnight at 18°C.

Next, the cultures were spun down and resuspended in 50 mM NaH_2PO_4 pH 8.0, 500 mM NaCl, 20 mM Imidazole and 5 mM β-mercaptoethanol (Ni^{2+} Buffer A). For KaiC, all buffers also contained fresh stocks of 1 mM ATP and 1 mM $MgCl_2$. Cell suspensions were either frozen for later purification or lysed immediately by passing through an Emulsiflex high pressure homogenizer (Avestin) ≥ 10 times at ≥ 10,000 psi. The soluble portion of the lysate was recovered by centrifugation for 45 minutes at 45,000 x g at 4°C. Clarified lysate was loaded onto Ni-NTA agarose (Qiagen, 5 mL per 2 L of *E. coli* culture) that had been equilibrated with 10 column volumes of Ni^{2+} Buffer A.

The Ni-NTA resin loaded with lysate was washed with ≥10 column volumes of Ni^{2+} Buffer A and bound proteins were eluted with 30 mL (per 5 mL Ni-NTA) of Ni^{2+} Buffer containing 250 mM Imidazole. The eluted protein was then treated with ~10 nmol Ulp1 enzyme for ≥ 30 minutes at room temperature to cleave the SUMO tag. The cleaved KaiC was then concentrated to ≤ 2 mL using a 30 kDa centrifugal filter (Millipore) and injected on a Superdex 200 gel filtration column (GE Healthcare) equilibrated with 20 mM Tris pH 7.4, 150 mM NaCl, 1 mM ATP, 1 mM $MgCl_2$, and 1 mM TCEP (KaiC buffer). Fractions containing KaiC hexamer were quantified using absorbance readings (λ = 280 nm) using the calculated extinction coefficient, frozen in liquid nitrogen, and stored at -70°C.

KaiB binding assays

KaiB binding assays were performed generally as described in Chavan *et. al* (*104*). Briefly, 30 µL of KaiC buffer containing 0.1% Tween and 50 nM fluorescently labeled KaiB was pipetted into 21 adjacent wells of a 384-well flat-bottom black polystyrene assay plate (Corning). KaiC aliquots were then thawed and supplemented with 0.1% Tween and 50 nM fluorescently labeled KaiB before 90 µL portions were added to the plate in line with the 21 buffer wells. Serial dilution was executed by transferring 60 µL of KaiC mixture to the first buffer well, mixing by pipetting in and out ≥ 6 times and then transferring 60 µL from that well to the subsequent well and repeating this process for all 21 wells. The plates were sealed and incubated overnight (~15 hours) at room temperature. Fluorescence anisotropy was measured on uncovered plates using a SYNERGY2 microplate reader (BioTek). 10-20 measurements were collected and averaged for each well, and data were analyzed using Prism (GraphPad). Data were fit to the Langmuir isotherm:

$$a = \Delta a_{total} * \frac{[KaiC]}{[KaiC] + K_{d,app}} + BG$$

where a is anisotropy, Δa_{total} is the change in anisotropy between bound and unbound KaiB, [KaiC] is the concentration of KaiC variant, $K_{d,app}$ is the apparent dissociation equilibrium constant, and BG is the background anisotropy. In cases where saturation could not be reached, as evidenced by the lack of stable anisotropy value as a function of KaiC concentration, a lower limit for $K_{d,app}$ was estimated by holding Δa_{total} constant at 0.043 anisotropy units. The raw anisotropy values were subsequently

converted to change in anisotropy by subtracting the *BG* term from the anisotropy values in each titration curve. The reported $K_{d,app}$ values were then determined by refitting the background-subtracted Δ anisotropy values to the Langmuir isotherm function above with the *BG* term omitted.

Error arising from differences in protein stability between mutants, as well as the inherent error in our curve fitting method, was estimated by performing replicate titrations using protein stocks that were thawed on different days. Replicate $K_{D,app}$ values from derived from curve-fitting on separate days are logarithmically transformed and pooled prior to statistical comparison.

Electron microscopy

Sample Preparation

KaiC-EA or KaiC-AE was briefly incubated on ice in 20 mM Tris pH 7.4, 150 mM NaCl and 1 mM each of ATP, $MgCl_2$ and TCEP. Sample (2.5 µL at 1.5 mg/ml) was then applied to an UltraAuFoil R1.2/1.3 300-mesh grid (Electron Microscopy Services), which was previously plasma-cleaned using a Gatan Solarus (75% argon/2% oxygen atmosphere, 15 W for 7 seconds). To overcome orientation bias in ice, an additional dataset was obtained by applying KaiC-EA (2.5 µL at 0.2 mg/ml) to holey C-flat grids, which previously had thin carbon floated on them. These grids were pretreated with 5 µL of 0.1 % (w/v) poly-L-lysine hydrobromine (Polysciences), blotted to dryness and then washed 3X with 10 µL of water. Grids with applied

sample were then manually blotted with filter paper (Whatman No.1) for ~3 seconds in a 4°C cold room before plunge-freezing in liquid ethane cooled by liquid nitrogen.

For the detergent dataset, KaiC-AE was incubated on ice with 4 mM fluorinated fos-choline-8 (Anatrace) added to the sample buffer. 2.5 μL of 6 mg/ml sample was added to UltraAuFoil R1.2/1.3 300-mesh grids (Electron Microscopy Services) that were pretreated with the addition of a graphene monolayer, using a modified protocol (*156*) for the deposition of graphene and made hydrophilic via UV/ozone cleaner (UVOCS T10 x 10 system) as previously described (*157*), and then incubated for 4 minutes in a cold room to concentrate particles on the surface of the grid before manual blotting for ~3 seconds followed by plunge freezing into liquid ethane.

Data acquisition

All cryo-EM data were acquired using the Leginon automated acquisition software (*158*). For KaiC-EA, all real-time image pre-processing, consisting of frame alignment, local CTF estimation, and particle picking were performed using the Appion image-processing pipeline during data collection (*159*). For KaiC-AE, all preprocessing was performed using Relion 3.0 (*160*).

Image collection was conducted using a Thermo Fischer Talos Arctica operating at 200 KeV and equipped with a Gatan K2 Summit DED. We used a nominal magnification of 36,000X, corresponding to a pixel size of 1.15 Å at the detector. For KaiC-EA, 1,137 movies were collected at a 40° tilt to overcome preferred orientation (*161*) with an exposure time of 8 seconds and an exposure rate

of 7.94 e^-/pixels/s and a total exposure of 48 $e^-/Å^2$ (0.6 e^- per frame) with a nominal defocus range of 0.8 – 1.7 μM. For the thin carbon KaiC-EA dataset, we collected 8,405 movies with no tilt and with an exposure time of 9 seconds. We used an exposure rate of 7.5 e^-/pixels/s for a total exposure of 51 $e^-/Å^2$ (1.4 e^- per frame) with a nominal defocus range of 0.5 – 1.5 μM. In the tilted KaiC-AE dataset, 1,132 movies were collected at 40° tilt with an exposure time of 11 seconds and exposure rate of 5.71 e^-/pixels/s for a total exposure of 48 $e^-/Å^2$ (0.9 e^- per frame) and with a nominal defocus range of 0.8 – 1.7 μM. For the KaiC-AE detergent dataset, 1,541 movies were collected with no tilt, using an exposure time of 6.2 seconds and exposure rate of 8.61 e^-/pixels/s for a total exposure of 40.32 $e^-/Å^2$ (0.7 e^- per frame) with a nominal defocus range of 0.5 – 2.0 μM.

Image processing

Movies of all KaiC datasets were aligned and dose-weighted in the Appion pipeline using Motioncorr2. For the tilted KaiC-EA dataset, 239 images were used for automated particle picking using Difference of Gaussians (DoG) picker to yield an initial 151,640 particles (*162*). Gctf was used for local CTF estimation, using an increased raster spacing of 500 to accommodate the defocus gradient resulting from the tilted data collection (*163*). Fourier-binned 4x4 particles were then subjected to reference-free 2D classification with multivariate statistical analysis (MSA) and multi-reference alignment (MRA) in the Appion pipeline (*159*). The two best classes representing tilted and side views were selected for template-based particle picking using FindEM (*164*), resulting in 2,016,826 particle picks from the entire dataset.

For initial particle curation, the ~2 million particle picks were subjected to two rounds of reference-free 2D classification in Relion (*160*), leaving 1,341,217 particles bearing structural details. A previous crystal structure of KaiC (pdb: 3K0C) was used to generate an initial model using the molmap feature in UCSF Chimera (*135*). This model was low-pass filtered to 20 Å resolution for 3D autorefinement in Relion, which resulted in a ~9.6 Å map that did not have discernable density for the majority of the CII ring. 3D classification into 6 classes without alignment resulted in two classes with mostly intact CII and CI rings, totaling 579,706 particles. These particles were re-centered and re-extracted at 2.3 Å/pixel.

For the thin carbon dataset, FindEM was used along with the same tilted and side view templates from the tilted dataset, resulting in 2,856,972 particle picks. CTFFIND4 was used for CTF estimation prior to extracting particles. Particles were Fourier-binned 4×4 and then subjected to one round of 2D classification in Relion, allowing for the removal of false particle picks and for the identification and selection of side views. 2,856,972 particles that belonged to exemplary side views were re-centered and re-extracted at 2.3 Å/pixel and then combined with the 579,706 particles from the tilted dataset. 3D classification in Relion with alignment, asking for four classes, gave a single well-resolved class comprising 1,002,777 particles. 3D autorefinement of the well-resolved class resulted in a map with a global resolution of ~4.7 Å. These particles were re-centered and re-extracted at 1.15 Å/pixel before undergoing a second 3D autorefinement, giving a new map with a global resolution of ~4.1 Å. Additional 3D classification, without alignment and using a Tau value of 10

and asking for four classes, generating three high resolution classes – two seemingly C_2-symmetric and one seemingly C_6-symmetric.

The 658,212 particles belonging to the two seemingly C_2-symmetric classes were joined for one round of 3D classification into three classes with no alignment and a Tau value of 20. One class containing the highest resolution features was selected for further processing. These 122,855 particles underwent 3D autorefinement with applied C_2 symmetry, giving a map with a global resolution of ~3.7 Å. An in-house python script was used to group particles by image shift, which then underwent iterative rounds of CTF refinement in Relion 3.1 refining both beam tilt and per-particle astigmatism correction. Subsequent 3D autorefinement with applied C_2 symmetry and a soft mask around the CI ring resulted in a map at ~3.5 Å. Postprocessing in Relion yielded a final C_2-state map at ~3.2 Å global resolution.

Particles from the seemingly C_6-symmetric class from the earlier 3D classification without alignment underwent 3D autorefinement, resulting in a ~4.1 Å map with 91,869 particles. 3D autorefinement with applied C_6 symmetry returned a ~3.7 Å map. Image shift grouping and iterative CTF refinement in Relion 3.1, followed by 3D autorefinement with applied C_6 symmetry and a soft mask around the CI ring resulted in a ~3.2 Å map. Postprocessing resulted in a final map for the C_6-state at ~2.8 Å resolution.

Particle picking for the detergent dataset for KaiC-AE was done using FindEM template picking, using a single axial and side view from the earlier datasets as templates, resulting in 427,620 particle picks. Particles were extracted at 2.3

Å/pixel and then underwent 2D alignment with cryoSPARC. Particles belonging to classes that showed secondary structure were selected as input particles for *ab initio* reconstruction, asking for 3 classes. One class, containing 111,877 particles, resembled the stacked ring shape of KaiC, and was selected for homogeneous refinement resulting in a map at ~6.3 Å resolution. These particles then underwent a second round of ab initio reconstruction with 3 classes, with one class containing 57,067 particles that resolved to ~6.7 Å after homogenous refinement. These particles were subjected to one final round of ab initio reconstruction with 2 classes, resulting in one class showing detailed structural features, consisting of 42,838 particles. Homogeneous refinement using C_1-symmetry resulted in a ~6.5 Å reconstruction, followed by homogenous refinement with C_6-symmetry, yielding a map at ~4.8 Å resolution. The full dataset (427,620 particle picks) was extracted, unbinned at 1.15 Å/pixel, and underwent 2D classification in Relion. The selected 367,247 particles were then subjected to 3D classification in Relion with a limited resolution E-step of 7 Å, using the ~4.8 Å map obtained from cryoSPARC as an initial model. Of the 4 resulting classes, one was selected for further processing with 89,892 particles. These particles underwent 3D autorefinement, resulting in a ~5.6 Å map, followed by CTF Refinement and 3D autorefinement once again, resulting in a ~4.8 Å map. Another round of CTF Refinement was conducted, followed by 3D autorefinement with C_6-symmetry resulting in a ~4.2 Å map which led to a final sharpened map at ~3.8 Å after postprocessing. All reported resolution are according to the FSC at a cutoff of 0.143.

Atomic model building and refinement

For both the extended and compressed state models of KaiC-EA, a crystal structure of the phosphomimetic mutant S431A/T432E was used as a starting point for model building (PDB: 3K0C) (*41*) with the C-terminal A-loops deleted. For the C_2-state, which showed large-scale repositioning of the C-terminal domains, proSMART local restraints (*165*) were generated in Coot (*166*) and then used to refit the domains into the cryo-EM density. After one round of real-space refinement in Phenix using default parameters and 5 macrocycles (*167*), Coot and ISOLDE (*168*) were used to improve main chains and side chains. The Molprobity server (*169*) (http://molprobity.biochem.duke.edu/) and PDB validation service server (https://validate-rcsb-1.wwpdb.org/) were used to identify problem regions for subsequent correction in Coot.

KaiC autophosphorylation assays

Samples of each KaiC variant were freshly prepared in KaiC buffer and mixed with KaiA to generate a final concentration of 1.5 μM KaiA and 3.4 μM KaiC. Samples were incubated at 30℃ for 24 hours, at which point 50 μL was removed and quenched with 10 μL of 6X SDS before incubating at 95℃ for 5 minutes.

Phos-Tag™ acrylamide gels were prepared with a resolving gel consisting of 10% (w/v) acrylamide (29:1 acrylamide/bis-acrylamide) containing Tris-HCl pH 8.8 supplemented with 50 μM Phos-tag™ reagent and 100 μM Mn^{2+}. Gels were run at constant 25mA with a 165V limit for 35 minutes before loading any samples into the

gel. Samples were loaded and run at room temperature with the same mA and voltage parameters as stated above for 170-190 minutes. Gels were stained using SYPRO® Orange following the Bio-Rad protocol and density was analyzed using ImageJ software (*119*). Error was estimated as the standard deviation from n = 3 replicate measurements analyzed separately.

Multiple sequence alignments

KaiC protein sequences were obtained from the UniProt database (*170*) and aligned using Clustal Omega (*171*).

KaiC ATPase activity assays

After the initial protein purification, frozen aliquots of each KaiC variant were thawed and run over a Sephadex 200 size-exclusion column (GE Healthcare) to exchange them into fresh buffer containing 50 mM MOPS pH 7.4, 150 mM $NaCl_2$, 1 mM TCEP, 1 mM $MgCl_2$, 400 μM ATP (ATPase buffer). Fractions containing KaiC hexamer were diluted to working assay concentrations with ATPase buffer for a final volume of 50 μL. Samples were then incubated at 30℃ and 5 μL aliquots were removed at 0, 4, and 8 hours timepoints and quenched using the ADP-Glo assay kit (Promega) according to manufacturer's instructions. Luminescence measurements (in relative light units, RLU) were taken at room temperature with a SYNERGY2

microplate reader in 384-well microplates. Data analysis was performed using Prism (GraphPad).

Standard curves were generated each day in ATPase buffer containing 20%, 40%, 60%, 80%, and 100% ADP while maintaining 400 μM total nucleotide concentration with ATP. Aliquots (5 μL) of these samples were mixed with ADP Glo reagent as described above. Plotting RLU versus μM ADP and solving for the x-intercept gives an equation that converts RLU values to μM ADP. Because the concentration of substrate (ATP) was in vast excess of the K_M of 2 μM (*172*), the Michaelis-Menten equation simplifies to the following:

$$v_0 = k_{\mathrm{cat}} \times [enzyme]$$

and the slope of the v_0 is the initial velocity, k_{cat} is the catalytic turnover rate and [enzyme] is, in this case, the concentration of KaiC variant in the assay. Thus, we plotted v_0 for each concentration of a given mutant against [KaiC] and, using the equation above, extracted k_{cat} as the slope of the resulting line.

Thermodynamic modeling of cooperativity indices

KaiC titrations were performed as described above, but with various concentrations of KaiB-I87A (fsKaiB) in both the KaiC and diluent stocks. Background anisotropy was subtracted from these data before analysis. Least squares fitting was performed using DynaFit (BioKin) as described in Chavan et al. with modifications. Specifically, the assumption that $K_5 = K_1$ was replaced by the assumption that $K_5 = K_3$ because that study used the KaiB-related protein SasA as a

secondary titrant, whereas here we used fsKaiB. Because wild-type KaiB assumes the same fold-switched conformation when in complex with KaiC (*37*), the assumption that $K_5 = K_3$ is therefore appropriate when fsKaiB is used as the secondary titrant.

Anisotropy values were allowed to float initially, and then restricted for extraction of the final model. The two highest fsKaiB concentrations were also allowed to float when fitting data for the mutant KaiC variants. Coefficients of variation for all parameters were found to be near or below 50% in almost all cases, indicating that the standard error from the regression is small compared to the best-fit value, and that the least-squares fitting gave reliable convergence to the thermodynamic model. Best-fit estimates for the equilibrium constants K_1, K_2 and K_4 were obtained, with K_3 being defined in this case by the thermodynamic balance equation,

$$K_1 \times K_2 = K_3 \times K_4$$

referring to the reaction scheme in Figure S10A (see reference for derivation and additional details) (*138*). Cooperativity indices, defined as K_1/K_3, were then calculated by dividing K_2 by K_4, which is equal to the cooperativity index by rearranging the thermodynamic balance equation to

$$cooperativity\ index = \frac{K_3}{K_1} = \frac{K_4}{K_2}$$

And error from least-squares fitting was estimated by propagation of the standard errors via the equation:

$$\sigma_{\frac{K_4}{K_2}} = \frac{K_4}{K_2} \times \sqrt{\left(\frac{\sigma_{K_4}}{K_4}\right)^2 + \left(\frac{\sigma_{K_2}}{K_2}\right)^2}$$

where K_x refers to the best-fit value for a given output and σ_x refers to the standard error for that particular parameter. In the 2D-titrations with KaiC-EA the absolute values of K_2 and K_4 were not well-defined by the data, with CV% greater than 100 observed. However, cooperativity indices of these estimates were consistent between replicate titrations, and Monte Carlo simulation of n = 1000 fits good correlation between the values of K_2 and K_4. Error was therefore estimated by calculating the cooperativity index for each individual Monte Carlo simulation, sorting them by magnitude and taking n = 25 and n = 975 as the upper and lower bound of the 95% confidence interval, respectively, and taking n = 500 as the average.

In vitro oscillation assays

KaiABC oscillator reactions were performed as described previously (*101, 104*). Briefly, purified protein stocks were mixed in buffer containing 20 mM Tris pH 8.0, 150 mM NaCl, 5 mM $MgCl_2$, and 1 mM ATP to a final concentration of 3.5 μM KaiC, 3.5 μM KaiB, 1.2 μM KaiA and 50 nM KaiB-K25C-fluorescein. Fluorescence anisotropy of was monitored at 30°C using a CLARIOstar (BMG Labtech) microplate reader. All data collection was performed using the fluorescein channel (λ_{ex}, 490 ± 5 nm; λ_{em}, 520 ± 5 nm), with a measurement taken every 15 minutes.

Strains and culture conditions for in vivo experiments

Markerless incorporation of the K224A point mutation into *kaiC* of *Synechococcus elongatus* PCC 7942 was performed by CRISPR/Cas12a engineering

as described previously (*110*). Characterization of circadian rhythms in the *kaiC*-K224A strain were performed as described in Chavan et al. (*104*). Briefly, bioluminescence was monitored from the P*kaiBC*::*luc* fusion reporter, inserted into a neutral site of the *S. elongatus* chromosome as previously described (*173*). Strains to be monitored were diluted to OD_{750} = 0.2. Aliquots (20 μL) of the suspension were added to 280 μL pads of BG-11 agar with 3.5 mM firefly luciferin in 96-well plates. Cells were entrained under 12-hour light-dark cycles (80 μmol $m^{-2}s^{-1}$) to synchronize clock phases. After 48 h of entrainment, cells were released into continuous light (30 μmol $m^{-2}s^{-1}$). Plates were transferred to a lighted stacker (40 μE light) attached to a Tecan Infinite M200 Pro and bioluminescence monitored every 2-3 hours.

Chapter 4: Structural and functional consequences of the tandem ATP cycle in KaiC

4.1 Abstract

While there is considerable existing structural and functional data on KaiC, the precise chemo-mechanical function of the ATP cycle is still up for debate. As we explored the previous chapter, the interactions between the enzymatic activities in the CI and CII are key factors in the ability of KaiC to perform its biological function. In this chapter, I examine the role of the ATP and ADP bound states in KaiC structure and function, using equilibrium KaiB binding assays to show that when the ATP hydrolysis cycle is circumvented, KaiB binds to KaiC regardless of phosphomimetic state. To begin to explore how nucleotide state affects the structural features of KaiC, I used a differential scanning fluorimetry assay that monitors binding of the solvatochromatic dye Sypro Orange to report on KaiC's tertiary and quaternary structure. Based on the results obtained with this assay, we performed a high-throughput screen with the goal of identifying solvatochromatic dyes that can detect biochemical oscillation of the KaiABC system continuously without covalent labeling. Initial lead compounds and next steps are summarized.

4.2 Dependence of KaiB discrimination on the ATPase cycle

Nucleotide interactions are known to affect the dynamic structural properties of KaiC (*146, 147*), and are involved in multiple different aspects of its various functions, including timekeeping (*39, 40, 99*), entrainment (*78, 82*) and KaiB-dependent phosphorepression (*28, 37, 51, 91*). Previous studies have shown that when the CI domain is restricted to the ATP-bound state, KaiC cannot bind to KaiB. However it was not clear whether this was due to lack of enzymatic activity, or the inability to adopt a permissive conformation for KaiB binding. To determine whether the entire ATP hydrolysis cycle is required for KaiB association, we tested KaiB association to both daytime and nighttime KaiC in the presence of either ATP, ADP or with the CI ATPase inactive mutations E77A-E78A in place (**Fig 4.1**).

In the presence of ATP, daytime KaiC, weaker binding curves were observed, but had increase sigmoidicity and required a Hill Coefficient >> 1 in order to extract a KD from the Langmuir isotherm. In all of the published work from this thesis, data points at high concentrations of KaiC were omitted for daytime KaiC for lack of of a physical explanation to explain this phenomenon, and an upper bound for KaiC affinity was estimated from the portion of the curve that reflected the Langmuir isotherm with Hill coefficients near 1. Figure 4.1 shows that daytime KaiC binds KaiB with the same affinity as nighttime KaiC when it is saturated with ADP. Because the CI domain hydrolyzes ATP continuously, more ADP accumulates at higher KaiC concentrations, possibly explaining why KaiB binding is observed in those data points.

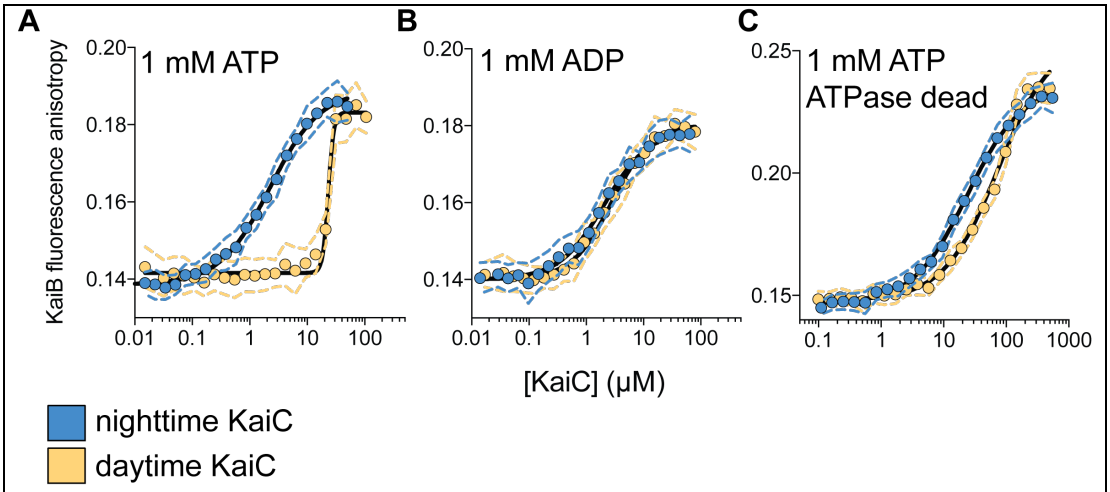

Figure 4.1 Dependence of KaiB affinity on the ATPase cycle of KaiC. **A)** Equilibrium binding titrations where the fluorescence anisotropy of fluorescently labeled KaiB-K25C is monitored as a function of KaiC concentration (daytime or nighttime) under standard assay conditions with 1 mM ATP or (**B**) ADP. Binding curves are fit to the K_D equation including with floating Hill Coefficient. Note that no data were omitted from these binding curves to minimize Hill Coefficients, as was done in Chapter 3. See text for discussion of this. **C**) Equilibrium binding titrations as described for (**A**) but with E77Q and E78Q mutations in place for the CI domain of daytime and nighttime KaiC phosphomimetics.

In addition to explaining the large hill coefficients in the daytime KaiC binding curves, binding of daytime KaiC to KaiB in the presence of ADP supports our conclusion from Chapter 3 that regulation of KaiB binding by the CII domain occurs through influencing over the CI active site, which enables cooperative recruitment of KaiB. In chapter 3, I showed that regulating the cooperativity of KaiB association is a key function of ATPase activity in the CI domain of KaiC. Furthermore, our cryo-EM structure of compressed KaiC identified the allosteric conduit through which information encoded in the phosphostate of the CII domain is transmitted to the CI active site where it can influence KaiB binding.

Note that in Figure 3.5, the K457A mutation also increases the affinity of daytime KaiC for KaiB. Abolishing the interaction of this positively charged residue with the nearby nucleotide might be expected to recapitulate the effect of saturating the CII ring with ADP, so we might also expect to see higher affinity for KaiB when CII is bound to ADP. However, ADP was observed exclusively in the CII domains of the extended daytime hexamers, despite that it was not supplied directly in the cryo-EM studies and was therefore present only as a result of enzymatic turnover of ATP. This strongly suggests that the gain of KaiB affinity observed for daytime KaiC in Fig. 4.1B is a result of accumulation of ADP in the CI domain in the daytime KaiC phosphomimetic, since the CII domain could be occupied with ADP in the ATP condition shown in Fig. 4.1A.

While it has been shown previously that KaiB cannot bind to nighttime KaiC in the presence of ATP when the catalytic activity of CII is abolished, nor can catalytically active KaiC bind KaiB in the presence of non-hydrolyzable ATP analog (*28*), these data provide significant clarification to the interpretation of those studies. Importantly, the data presented in Fig. 4.1 show that ATP hydrolysis itself is not necessary, but suggest instead that adoption of the post-hydrolysis conformation in the CI domain is required, regardless of whether ATP hydrolysis has occurred or not.

In this sense, another way of stating the result in Fig. 4.1 is that ATP hydrolysis is required for discrimination of KaiB association to the nighttime state. This is consistent our model presented in Fig. 3.17B, whereby interactions between the CI and CII domains, which are phosphostate dependent, influence the relationship

between ATP hydrolysis and KaiB recruitment, whereby ADP is locked into the CI domain upon KaiB association in a manner that is dependent on interactions of CI with CII via the arginine tetrad. CII phosphostate is known to alter ATPase turnover rates in the CI domain (*39*), likely through the regulation of ADP product release. Thus, it is reasonable to assume that regulation of KaiB association to the CI domain is regulated by the CII domain through a related mechanism, and when the CII is forced into the ADP saturated state, this influence becomes irrelevant.

4.3: Dye binding reveals a complex thermal stability landscape in KaiC.

To determine whether we could differentiate daytime and nighttime KaiC based on the thermal stability of their respective conformational states, we performed thermal melting studies, whereby daytime and nighttime KaiC were monitored by either DSF or circular dichroism (CD, **Fig. 4.2A**). We found that overall folding of KaiC, reported by CD ellipticity at 222 nm, was remarkably stable, with loss of secondary structure beginning to occur at around 85 °C. Notably this observation is consistent with similar studies on other hexameric AAA+ proteins (*174, 175*).

By contrast, Sypro Orange fluorescence observed by DSF exhibited a complex curve of fluorescence intensity over the course of increasing temperature, with plateaus occurring around 37, 50, 65 and 80 °C. However, the features of the protein melting curves measured by Sypro Orange fluorescence do not necessarily report on denaturation of protein secondary structures, they just report on the binding of Sypro Orange to hydrophobic areas of KaiC that are occluded from solvent due to

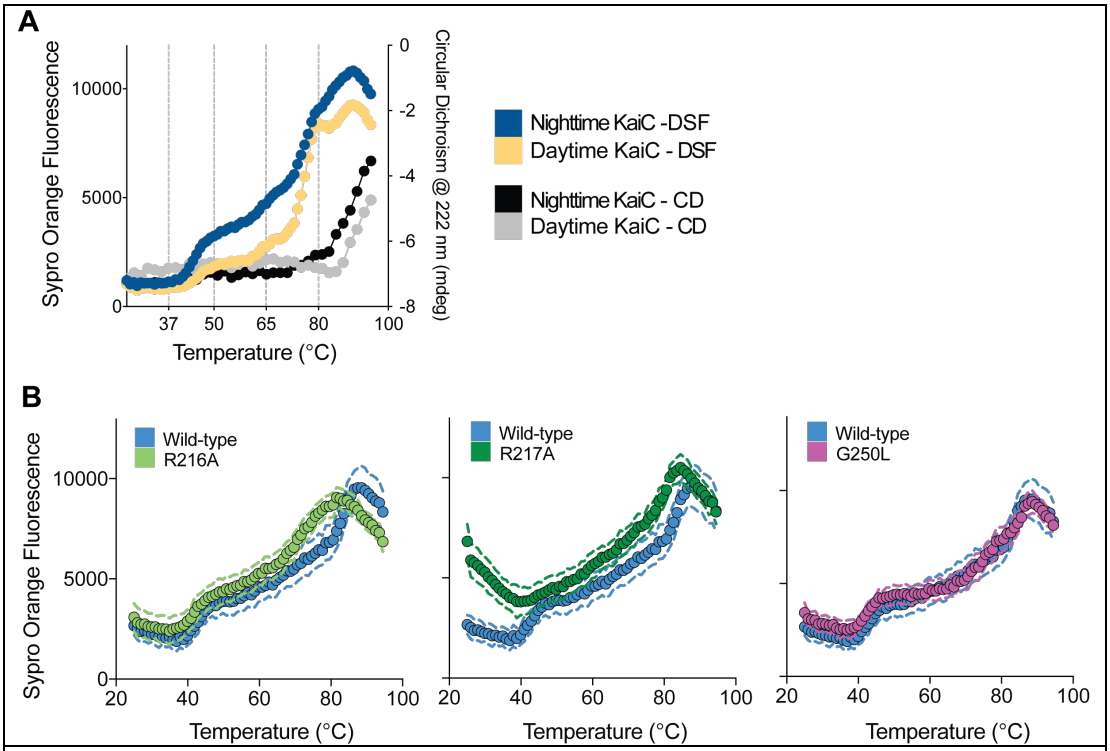

Figure 4.2 Sypro Orange reports tertiary unfolding transitions.
A) Thermal denaturation of daytime and nighttime KaiC phosphomimetics monitored by either Sypro Orange fluorescence or circular dichroism at 222 nm. **B**) Mutants of nighttime KaiC analyzed by DSF alongside unsubstituted nighttime KaiC phosphomimetic using identical parameters to those in **A**. Dots represent average values for each temperature from n=5 replicate wells that were assayed alongside each other in the plate. Dashed lines show standard deviations between these measurements.

tertiary and quaternary (i.e. between individual protomers within the hexamer) protein-protein interactions. For this reason, such protein melting curves will be referred to in this thesis as tertiary denaturation curves.

Given the dynamic nature of the KaiC hexamer, I hypothesized that mutations that alter the dynamics and inter-subunit interactions of KaiC might give specific signatures in the tertiary denaturation curves. To test this, I ran DSF on two mutants of nighttime KaiC, R216A and R217A (**Fig. 4.2B**), which are located at the arginine

tetrad at the interface between the CI and CII domains of KaiC and are critical for interdomain communication.

Comparing the tertiary denaturation curves for these mutants to the wild type nighttime KaiC, R216A differs from wild-type at low temperatures, while R217A seems to bind Sypro Orange more readily at the beginning of the denaturation experiment, around room temperature, but then behaves more similarly to wild type after the transition around 50 °C. Another mutant I tested was G250L (*176*), expected to alter interdomain dynamics; however, very little difference was observed between this and wild-type nighttime KaiC.

Next, I explored the relationship between KaiC dynamics and the ATPase cycle by testing the effect of nucleotide state on the tertiary denaturation profile for both daytime and nighttime KaiC (**Fig. 4.3A**). In both cases, Sypro Orange binding was increased in the presence of ADP during the initial transition around 50 °C. Furthermore, in both cases, the highest temperature shift in Sypro Orange binding happens around 80 °C in the presence of ATP, but this is shifted by around 15 degrees to 65 °C in the presence of ADP, in a similar to what was seen for the R216A nighttime KaiC mutant.

In chapter 3, the homologous K224A and K457A residues were shown to sense nucleotide state in the CI and CII active sites, respectively, and relay that information to other domains to regulate KaiC function. To test whether the structural effects of these mutations alter the stability of the conformations detected in our tertiary denaturation assay, I performed DSF on these mutants in the presence of ATP

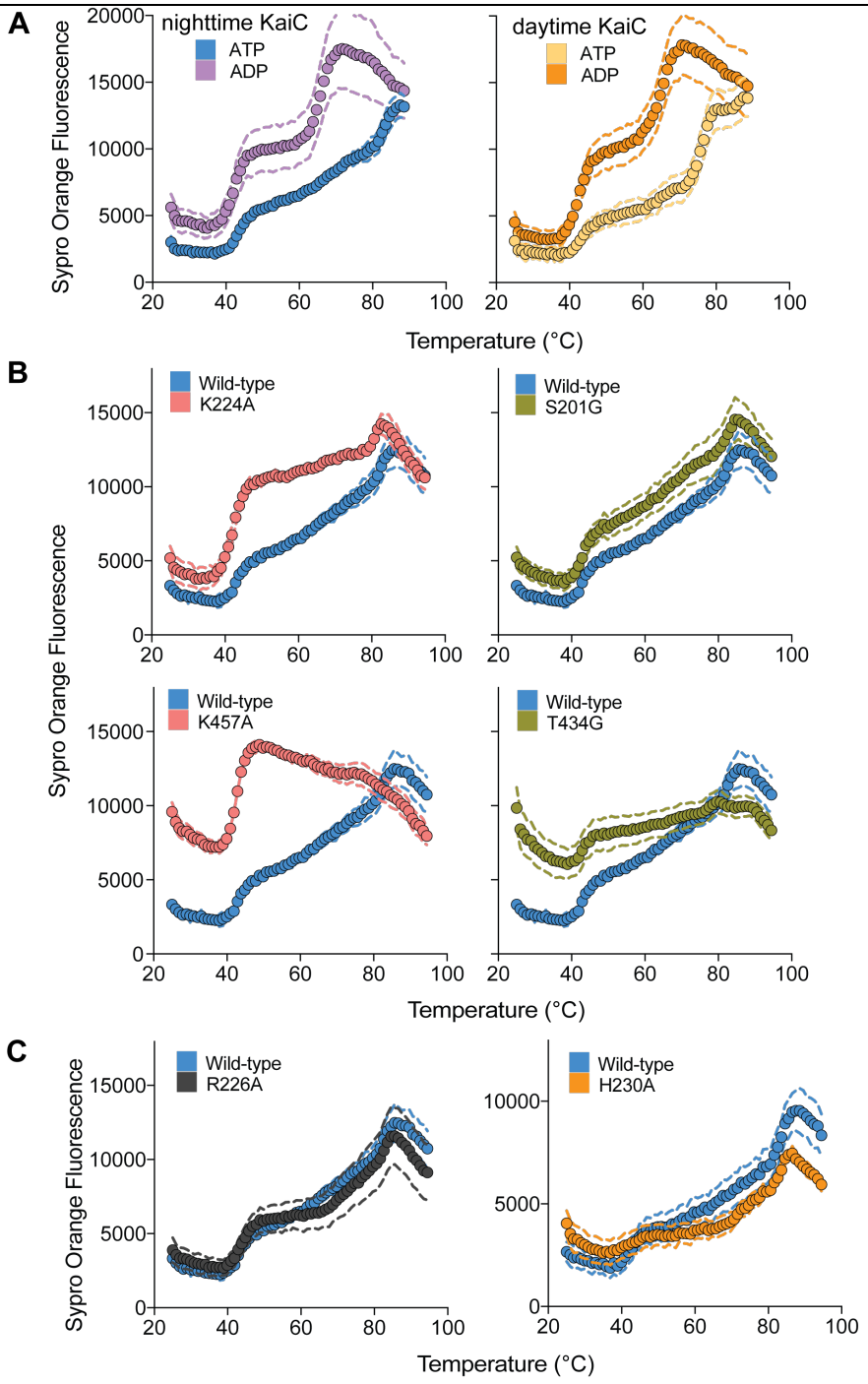

Figure 4.3 Tertiary denaturation of KaiC reports on stability of the nucleotide binding cleft.
A) Thermal denaturation curves measured by Sypro Orange fluorescence are compared for daytime and nighttime KaiC in the presence of either 1 mM ATP or 1 mM ADP. **B**) Thermal denaturation, as monitored by Sypro Orange fluorescence

for CI and CII active site mutants is compared to unsubstituted nighttime KaiC. Homologous CI and CII residues are shown in same colors. Additional CI active site mutants are shown in **C**.

(**Fig. 4.3B**). Strikingly, both mutants showed large increases in Sypro Orange binding in the initial transition around 50 °C. Another set of homologous CI and CII active site mutants, S201G and T434G, were tested as well and gave their own unique profiles of Sypro Orange binding. I also tested active site mutants that had shown interesting activities in Chapter 3, nighttime KaiC with R226A or H230A mutations. These had smaller effects on the tertiary denaturation profile.

Qualitatively, the tertiary denaturation profiles presented in Fig. 4.3 are possibly rich in information about the conformations of KaiC, although it has thus far proven challenging to draw direct conclusions from these changes.

4.4 Discrimination of KaiC phosphostates using solvatochromatic dyes

Based on the result that different tertiary conformational states might be detectable using Sypro Orange, we sought to identify other solvatochromatic dyes that can distinguish daytime and nighttime KaiC at physiologically relevant temperatures (25-30 °C). If identified, such a small molecule could be used to monitor KaiC oscillations *in vitro* continuously, similar to the fluorescence anisotropy method reported by Heisler et al. (*101*), but bypassing the requirement of fluorescently labeling KaiB. Another advantage of such an approach is that it would

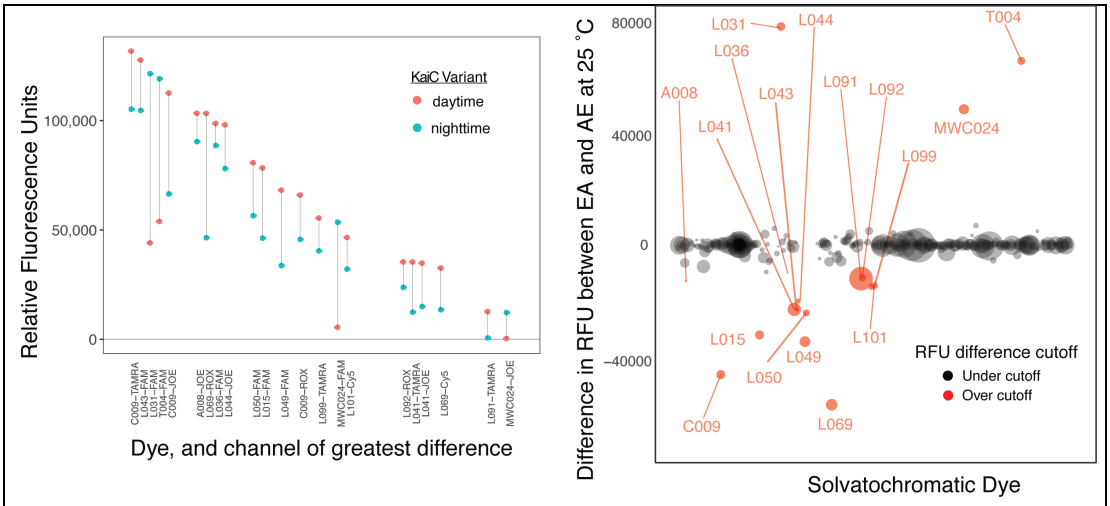

Figure 4.4: High throughput solvatochromatic dye screen to differentiate KaiC phosphomimetics.
Screening of solvatochromatic dyes was performed to identify compounds that have the greatest difference in fluorescence depending on the presence of daytime or nighttime KaiC phosphomimetics. Overall winners are shown in the left panel, with color codes to describe whether greater fluorescence was observed for daytime or nighttime KaiC. In the right panel, these results are compared with the results for compounds that were not considered winners.

report directly on KaiC state, similar to the manual phosphorylation assays that have dominated the field since autonomous biochemical oscillation was first discovered (*3, 39, 99, 111*) rather than KaiB association as the Heisler *et. al* method does. Additionally, small molecules such as dyes that bind preferentially to daytime or nighttime KaiC states might be expected to affect the timing of the biochemical oscillator, by virtue of stabilizing or destabilizing the KaiC phosphostate to which it binds discriminately.

To identify such compounds, we collaborated with Taia Wu from the Gestwicki lab at UC San Francisco. Using a library of over 300 solvatochromatic dyes, Taia performed thermal denaturation studies where fluorescence was measured

as a function of temperature for each dye in the presence of either daytime KaiC or nighttime KaiC phosphomimetic. Because each dye has its own distinct excitation and emission properties, the screen was monitored using 4 different excitation and emission filter sets, corresponding to the optimal wavelength parameters for FAM, TAMRA, JOE and Cy5. Note that these data were also collected at a range of dye concentrations (6.25, 12.5, 25 and 50 μM). Since our goal was to identify dyes that bind differentially to the different phosphoforms of KaiC at room temperature, Further analysis of this dataset focused only on the 25 °C datapoint. The data for each dye was parsed according to the fluorescence emission channel and dye concentration that gave the largest difference between the two KaiC phosphomimetics at °25 C to identify several "winners." (**Fig. 4.4**).

In our initial collaboration with the Gestwicki lab, many promising compounds were identified using the thermal denaturation assay, the overall goal of identifying molecules for fluorescent monitoring of unlabeled biochemical oscillation reactions would likely be better served by performing the high-throughput screen on the oscillator reactions themselves. A set of filters has been installed in the Partch Lab's Synergy2 platereader to perform such a study, whereby multiple excitation and emission wavelengths could be used to monitor oscillator reactions, each containing a different compound from the dye library.

4.5 Materials and Methods

Preparation of ADP bound KaiC

For the ADP conditions described in this chapter, the KaiC phosphomimetics were prepped with ADP in place of ATP throughout the entire process, from when the cell pellets were resuspended to the final size exclusion chromatography step. Otherwise, protein purification was performed as described for Chapters 2 and 3.

Equilibrium binding assays

Binding assays were carried out as described in Chapter 2.

Differential scanning fluorimetry with Sypro Orange.

Sypro Orange (Thermo Fisher) is available as a 5000x stock in DMSO. For DSF assays, it was first diluted to 5x using distilled sterilized water, and then mixed with 4 parts of the buffered KaiC mixture by adding 3 μL of 5x dye with 12 μL of buffered KaiC mixture in a 384 well qPCR plate (MicroAmp Optical 384-Well Reaction Plate with Barcode, reference no. 4309849). Thermal denaturation was monitored on a QuantStudio qPCR machine using ROX fluorescence filters. Thermal denaturation was performed in 1 °C increments, incubating for 1 minute before taking fluorescence measurements. The samples were allowed to equilibrate for 10 minutes to 25 °C in the instrument prior to the starting the denaturation protocol.

Circular Dichroism

CD measurements were conducted using a JASCO CD spectrometer. Because of interference from ATP absorption, full spectra (190-260 nm) could only be obtained using a 50 μM cuvette, but sample evaporation was a challenge under these conditions. Therefore, a 1 mm pathlength quartz cuvette was used to monitor the ellipticity at 222 nm with thermal denaturation performed in 2 °C increments, keeping the total time of denaturation constant between the DSF and CD thermal melts.

Bibliography

1. S. J. Kuhlman, L. M. Craig, J. F. Duffy, Introduction to Chronobiology. *Cold Spring Harb Perspect Biol*, (2017).
2. J. M. Hurley, J. J. Loros, J. C. Dunlap, Circadian Oscillators: Around the Transcription-Translation Feedback Loop and on to Output. *Trends Biochem Sci* **41**, 834-846 (2016).
3. M. Nakajima *et al.*, Reconstitution of circadian oscillation of cyanobacterial KaiC phosphorylation in vitro. *Science* **308**, 414-415 (2005).
4. C. H. Johnson, C. Zhao, Y. Xu, T. Mori, Timing the day: what makes bacterial clocks tick? *Nat Rev Microbiol* **15**, 232-242 (2017).
5. A. Mitsui *et al.*, Strategy by Which Nitrogen-Fixing Unicellular Cyanobacteria Grow Photoautotrophically. *Nature* **323**, 720-722 (1986).
6. H. Ito *et al.*, Cyanobacterial daily life with Kai-based circadian and diurnal genome-wide transcriptional control in Synechococcus elongatus. *Proc Natl Acad Sci U S A* **106**, 14168-14173 (2009).
7. Y. Liu *et al.*, Circadian orchestration of gene expression in cyanobacteria. *Genes Dev* **9**, 1469-1478 (1995).
8. R. M. Smith, S. B. Williams, Circadian rhythms in gene transcription imparted by chromosome compaction in the cyanobacterium Synechococcus elongatus. *Proc Natl Acad Sci U S A* **103**, 8564-8569 (2006).

9. V. Vijayan, R. Zuzow, E. K. O'Shea, Oscillations in supercoiling drive circadian gene expression in cyanobacteria. *Proc Natl Acad Sci U S A* **106**, 22564-22568 (2009).

10. M. Ishiura *et al.*, Expression of a gene cluster kaiABC as a circadian feedback process in cyanobacteria. *Science* **281**, 1519-1523 (1998).

11. J. Tomita, M. Nakajima, T. Kondo, H. Iwasaki, No transcription-translation feedback in circadian rhythm of KaiC phosphorylation. *Science* **307**, 251-254 (2005).

12. Y. Kitayama, T. Nishiwaki, K. Terauchi, T. Kondo, Dual KaiC-based oscillations constitute the circadian system of cyanobacteria. *Genes Dev* **22**, 1513-1521 (2008).

13. X. Qin *et al.*, Intermolecular associations determine the dynamics of the circadian KaiABC oscillator. *Proc Natl Acad Sci U S A* **107**, 14805-14810 (2010).

14. N. Hosokawa, H. Kushige, H. Iwasaki, Attenuation of the posttranslational oscillator via transcription-translation feedback enhances circadian-phase shifts in Synechococcus. *Proc Natl Acad Sci U S A* **110**, 14486-14491 (2013).

15. S. Hunter *et al.*, InterPro: the integrative protein signature database. *Nucleic Acids Res* **37**, D211-215 (2009).

16. F. Sievers *et al.*, Fast, scalable generation of high-quality protein multiple sequence alignments using Clustal Omega. *Mol Syst Biol* **7**, 539 (2011).

17. K. Onai, M. Morishita, S. Itoh, K. Okamoto, M. Ishiura, Circadian rhythms in the thermophilic cyanobacterium Thermosynechococcus elongatus: compensation of period length over a wide temperature range. *J Bacteriol* **186**, 4972-4977 (2004).

18. Y. Taniguchi *et al.*, labA: a novel gene required for negative feedback regulation of the cyanobacterial circadian clock protein KaiC. *Genes Dev* **21**, 60-70 (2007).

19. M. Hanaoka *et al.*, RpaB, another response regulator operating circadian clock-dependent transcriptional regulation in Synechococcus elongatus PCC 7942. *J Biol Chem* **287**, 26321-26327 (2012).

20. J. S. Boyd *et al.*, A Combined Computational and Genetic Approach Uncovers Network Interactions of the Cyanobacterial Circadian Clock. *J Bacteriol* **198**, 2439-2447 (2016).

21. J. Espinosa *et al.*, Cross-talk and regulatory interactions between the essential response regulator RpaB and cyanobacterial circadian clock output. *Proc Natl Acad Sci U S A* **112**, 2198-2203 (2015).

22. T. Osanai *et al.*, Alteration of cyanobacterial sugar and amino acid metabolism by overexpression hik8, encoding a KaiC-associated histidine kinase. *Environ Microbiol* **17**, 2430-2440 (2015).

23. N. B. Ivleva, M. R. Bramlett, P. A. Lindahl, S. S. Golden, LdpA: a component of the circadian clock senses redox state of the cell. *EMBO J* **24**, 1202-1210 (2005).

24. S. E. Cohen, S. S. Golden, Circadian Rhythms in Cyanobacteria. *Microbiol Mol Biol Rev* **79**, 373-385 (2015).

25. T. Mori *et al.*, Circadian clock protein KaiC forms ATP-dependent hexameric rings and binds DNA. *Proc Natl Acad Sci U S A* **99**, 17203-17208 (2002).

26. R. Pattanayek *et al.*, Visualizing a circadian clock protein: crystal structure of KaiC and functional insights. *Mol Cell* **15**, 375-388 (2004).

27. F. Hayashi, R. Iwase, T. Uzumaki, M. Ishiura, Hexamerization by the N-terminal domain and intersubunit phosphorylation by the C-terminal domain of cyanobacterial circadian clock protein KaiC. *Biochem Biophys Res Commun* **348**, 864-872 (2006).

28. C. Phong, J. S. Markson, C. M. Wilhoite, M. J. Rust, Robust and tunable circadian rhythms from differentially sensitive catalytic domains. *Proc Natl Acad Sci U S A* **110**, 1124-1129 (2013).

29. F. Hayashi *et al.*, Roles of two ATPase-motif-containing domains in cyanobacterial circadian clock protein KaiC. *J Biol Chem* **279**, 52331-52337 (2004).

30. H. Kageyama, T. Kondo, H. Iwasaki, Circadian formation of clock protein complexes by KaiA, KaiB, KaiC, and SasA in cyanobacteria. *J Biol Chem* **278**, 2388-2395 (2003).

31. T. Nishiwaki *et al.*, A sequential program of dual phosphorylation of KaiC as a basis for circadian rhythm in cyanobacteria. *EMBO J* **26**, 4029-4037 (2007).

32. H. Kageyama *et al.*, Cyanobacterial circadian pacemaker: Kai protein complex dynamics in the KaiC phosphorylation cycle in vitro. *Mol Cell* **23**, 161-171 (2006).

33. H. Iwasaki, T. Nishiwaki, Y. Kitayama, M. Nakajima, T. Kondo, KaiA-stimulated KaiC phosphorylation in circadian timing loops in cyanobacteria. *Proc Natl Acad Sci U S A* **99**, 15788-15793 (2002).

34. Y. I. Kim, G. Dong, C. W. Carruthers, Jr., S. S. Golden, A. LiWang, The day/night switch in KaiC, a central oscillator component of the circadian clock of cyanobacteria. *Proc Natl Acad Sci U S A* **105**, 12825-12830 (2008).

35. Y. G. Chang, R. Tseng, N. W. Kuo, A. LiWang, Rhythmic ring-ring stacking drives the circadian oscillator clockwise. *Proc Natl Acad Sci U S A* **109**, 16847-16851 (2012).

36. Y. G. Chang *et al.*, Circadian rhythms. A protein fold switch joins the circadian oscillator to clock output in cyanobacteria. *Science* **349**, 324-328 (2015).

37. R. Tseng *et al.*, Structural basis of the day-night transition in a bacterial circadian clock. *Science* **355**, 1174-1180 (2017).

38. M. J. Rust, J. S. Markson, W. S. Lane, D. S. Fisher, E. K. O'Shea, Ordered phosphorylation governs oscillation of a three-protein circadian clock. *Science* **318**, 809-812 (2007).

39. K. Terauchi *et al.*, ATPase activity of KaiC determines the basic timing for circadian clock of cyanobacteria. *Proc Natl Acad Sci U S A* **104**, 16377-16381 (2007).

40. J. Abe *et al.*, Circadian rhythms. Atomic-scale origins of slowness in the cyanobacterial circadian clock. *Science* **349**, 312-316 (2015).

41. R. Pattanayek *et al.*, Structures of KaiC circadian clock mutant proteins: a new phosphorylation site at T426 and mechanisms of kinase, ATPase and phosphatase. *PLoS One* **4**, e7529 (2009).

42. Y. Murayama *et al.*, Tracking and visualizing the circadian ticking of the cyanobacterial clock protein KaiC in solution. *EMBO J* **30**, 68-78 (2011).

43. Y. G. Chang, N. W. Kuo, R. Tseng, A. LiWang, Flexibility of the C-terminal, or CII, ring of KaiC governs the rhythm of the circadian clock of cyanobacteria. *Proc Natl Acad Sci U S A* **108**, 14431-14436 (2011).

44. T. Nishiwaki, T. Kondo, Circadian autodephosphorylation of cyanobacterial clock protein KaiC occurs via formation of ATP as intermediate. *J Biol Chem* **287**, 18030-18035 (2012).

45. M. Egli *et al.*, Dephosphorylation of the core clock protein KaiC in the cyanobacterial KaiABC circadian oscillator proceeds via an ATP synthase mechanism. *Biochemistry* **51**, 1547-1558 (2012).

46. D. Stock, A. G. Leslie, J. E. Walker, Molecular architecture of the rotary motor in ATP synthase. *Science* **286**, 1700-1705 (1999).

47. M. Egli *et al.*, Loop-loop interactions regulate KaiA-stimulated KaiC phosphorylation in the cyanobacterial KaiABC circadian clock. *Biochemistry* **52**, 1208-1220 (2013).

48. T. Nishiwaki-Ohkawa, Y. Kitayama, E. Ochiai, T. Kondo, Exchange of ADP with ATP in the CII ATPase domain promotes autophosphorylation of cyanobacterial clock protein KaiC. *Proc Natl Acad Sci U S A* **111**, 4455-4460 (2014).

49. R. Pattanayek, M. Egli, Protein-Protein Interactions in the Cyanobacterial Circadian Clock: Structure of KaiA Dimer in Complex with C-Terminal KaiC Peptides at 2.8 A Resolution. *Biochemistry* **54**, 4575-4578 (2015).

50. R. Tseng *et al.*, Cooperative KaiA-KaiB-KaiC interactions affect KaiB/SasA competition in the circadian clock of cyanobacteria. *J Mol Biol* **426**, 389-402 (2014).

51. J. Snijder *et al.*, Structures of the cyanobacterial circadian oscillator frozen in a fully assembled state. *Science* **355**, 1181-1184 (2017).

52. M. Sugiyama *et al.*, Structural characterization of the circadian clock protein complex composed of KaiB and KaiC by inverse contrast-matching small-angle neutron scattering. *Sci Rep* **6**, 35567 (2016).

53. R. Iwase *et al.*, Functionally important substructures of circadian clock protein KaiB in a unique tetramer complex. *J Biol Chem* **280**, 43141-43149 (2005).

54. K. Hitomi, T. Oyama, S. Han, A. S. Arvai, E. D. Getzoff, Tetrameric architecture of the circadian clock protein KaiB. A novel interface for

intermolecular interactions and its impact on the circadian rhythm. *J Biol Chem* **280**, 19127-19135 (2005).

55. R. Murakami *et al.*, The roles of the dimeric and tetrameric structures of the clock protein KaiB in the generation of circadian oscillations in cyanobacteria. *J Biol Chem* **287**, 29506-29515 (2012).

56. J. Snijder *et al.*, Insight into cyanobacterial circadian timing from structural details of the KaiB-KaiC interaction. *Proc Natl Acad Sci U S A* **111**, 1379-1384 (2014).

57. N. Takai *et al.*, A KaiC-associating SasA-RpaA two-component regulatory system as a major circadian timing mediator in cyanobacteria. *Proc Natl Acad Sci U S A* **103**, 12109-12114 (2006).

58. A. Y. Mitrophanov, E. A. Groisman, Signal integration in bacterial two-component regulatory systems. *Genes Dev* **22**, 2601-2611 (2008).

59. R. Gao, A. M. Stock, Biological insights from structures of two-component proteins. *Annu Rev Microbiol* **63**, 133-154 (2009).

60. C. P. Zschiedrich, V. Keidel, H. Szurmant, Molecular Mechanisms of Two-Component Signal Transduction. *J Mol Biol* **428**, 3752-3775 (2016).

61. M. T. Laub, M. Goulian, Specificity in two-component signal transduction pathways. *Annu Rev Genet* **41**, 121-145 (2007).

62. M. K. Ashby, J. Houmard, Cyanobacterial two-component proteins: structure, diversity, distribution, and evolution. *Microbiol Mol Biol Rev* **70**, 472-509 (2006).

63. A. Gutu, E. K. O'Shea, Two antagonistic clock-regulated histidine kinases time the activation of circadian gene expression. *Mol Cell* **50**, 288-294 (2013).

64. Y. Taniguchi, N. Takai, M. Katayama, T. Kondo, T. Oyama, Three major output pathways from the KaiABC-based oscillator cooperate to generate robust circadian kaiBC expression in cyanobacteria. *Proc Natl Acad Sci U S A* **107**, 3263-3268 (2010).

65. J. S. Markson, J. R. Piechura, A. M. Puszynska, E. K. O'Shea, Circadian control of global gene expression by the cyanobacterial master regulator RpaA. *Cell* **155**, 1396-1408 (2013).

66. I. Vakonakis, D. A. Klewer, S. B. Williams, S. S. Golden, A. C. LiWang, Structure of the N-terminal domain of the circadian clock-associated histidine kinase SasA. *J Mol Biol* **342**, 9-17 (2004).

67. S. J. Valencia *et al.*, Phase-dependent generation and transmission of time information by the KaiABC circadian clock oscillator through SasA-KaiC interaction in cyanobacteria. *Genes Cells* **17**, 398-419 (2012).

68. M. Wojnowska *et al.*, Autophosphorylation activity of a soluble hexameric histidine kinase correlates with the shift in protein conformational equilibrium. *Chem Biol* **20**, 1411-1420 (2013).

69. G. Rivera-Cancel, W. H. Ko, D. R. Tomchick, F. Correa, K. H. Gardner, Full-length structure of a monomeric histidine kinase reveals basis for sensory regulation. *Proc Natl Acad Sci U S A* **111**, 17839-17844 (2014).

70. R. Murakami *et al.*, Cooperative Binding of KaiB to the KaiC Hexamer Ensures Accurate Circadian Clock Oscillation in Cyanobacteria. *Int J Mol Sci* **20**, (2019).

71. S. E. Cohen *et al.*, Dynamic localization of the cyanobacterial circadian clock proteins. *Curr Biol* **24**, 1836-1844 (2014).

72. S. R. Mackey *et al.*, Proteins found in a CikA interaction assay link the circadian clock, metabolism, and cell division in Synechococcus elongatus. *J Bacteriol* **190**, 3738-3746 (2008).

73. O. Schmitz, M. Katayama, S. B. Williams, T. Kondo, S. S. Golden, CikA, a bacteriophytochrome that resets the cyanobacterial circadian clock. *Science* **289**, 765-768 (2000).

74. N. B. Ivleva, T. Gao, A. C. LiWang, S. S. Golden, Quinone sensing by the circadian input kinase of the cyanobacterial circadian clock. *Proc Natl Acad Sci U S A* **103**, 17468-17473 (2006).

75. S. B. Williams, I. Vakonakis, S. S. Golden, A. C. LiWang, Structure and function from the circadian clock protein KaiA of Synechococcus elongatus: a potential clock input mechanism. *Proc Natl Acad Sci U S A* **99**, 15357-15362 (2002).

76. G. K. Pattanayak, C. Phong, M. J. Rust, Rhythms in energy storage control the ability of the cyanobacterial circadian clock to reset. *Curr Biol* **24**, 1934-1938 (2014).

77. D. A. Golombek, R. E. Rosenstein, Physiology of circadian entrainment. *Physiol Rev* **90**, 1063-1102 (2010).

78. M. J. Rust, S. S. Golden, E. K. O'Shea, Light-driven changes in energy metabolism directly entrain the cyanobacterial circadian oscillator. *Science* **331**, 220-223 (2011).

79. Y. I. Kim, D. J. Vinyard, G. M. Ananyev, G. C. Dismukes, S. S. Golden, Oxidized quinones signal onset of darkness directly to the cyanobacterial circadian oscillator. *Proc Natl Acad Sci U S A* **109**, 17765-17769 (2012).

80. T. L. Wood *et al.*, The KaiA protein of the cyanobacterial circadian oscillator is modulated by a redox-active cofactor. *Proc Natl Acad Sci U S A* **107**, 5804-5809 (2010).

81. T. Gao, X. Zhang, N. B. Ivleva, S. S. Golden, A. LiWang, NMR structure of the pseudo-receiver domain of CikA. *Protein Sci* **16**, 465-475 (2007).

82. E. Leypunskiy *et al.*, The cyanobacterial circadian clock follows midday in vivo and in vitro. *Elife* **6**, (2017).

83. D. A. Bryant, *The molecular biology of cyanobacteria*. Advances in photosynthesis (Kluwer Academic Publishers, Dordrecht ; Boston, 1994).

84. B. J. H. M. Rosier, T. F. A. De Greef, How to make an oscillator. *Elife* **4**, (2015).

85. E. Bartocci, L. Bortolussi, L. Nenzi, A Temporal Logic Approach to Modular Design of Synthetic Biological Circuits. *Lect N Bioinformat* **8130**, 164-177 (2013).

86. L. Potvin-Trottier, N. D. Lord, G. Vinnicombe, J. Paulsson, Synchronous long-term oscillations in a synthetic gene circuit. *Nature* **538**, 514-517 (2016).

87. O. Purcell, N. J. Savery, C. S. Grierson, M. di Bernardo, A comparative analysis of synthetic genetic oscillators. *J R Soc Interface* **7**, 1503-1524 (2010).

88. A. H. Chen, D. Lubkowicz, V. Yeong, R. L. Chang, P. A. Silver, Transplantability of a circadian clock to a noncircadian organism. *Sci Adv* **1**, (2015).

89. J. S. van Zon, D. K. Lubensky, P. R. Altena, P. R. ten Wolde, An allosteric model of circadian KaiC phosphorylation. *Proc Natl Acad Sci U S A* **104**, 7420-7425 (2007).

90. L. Ma, R. Ranganathan, Quantifying the rhythm of KaiB-C interaction for in vitro cyanobacterial circadian clock. *PLoS One* **7**, e42581 (2012).

91. J. Lin, J. Chew, U. Chockanathan, M. J. Rust, Mixtures of opposing phosphorylations within hexamers precisely time feedback in the cyanobacterial circadian clock. *Proc Natl Acad Sci U S A* **111**, E3937-3945 (2014).

92. J. Paijmans, D. K. Lubensky, P. R. Ten Wolde, A thermodynamically consistent model of the post-translational Kai circadian clock. *PLoS Comput Biol* **13**, e1005415 (2017).

93. J. C. Dunlap, J. J. Loros, P. J. DeCoursey, *Chronobiology : biological timekeeping*. (Sinauer Associates, Sunderland, Mass., 2004), pp. xix, 406 p.

94. M. A. Woelfle, Y. Ouyang, K. Phanvijhitsiri, C. H. Johnson, The adaptive value of circadian clocks: an experimental assessment in cyanobacteria. *Curr Biol* **14**, 1481-1486 (2004).

95. T. Kondo *et al.*, Circadian rhythms in prokaryotes: luciferase as a reporter of circadian gene expression in cyanobacteria. *Proc Natl Acad Sci U S A* **90**, 5672-5676 (1993).

96. Y. Kitayama, H. Iwasaki, T. Nishiwaki, T. Kondo, KaiB functions as an attenuator of KaiC phosphorylation in the cyanobacterial circadian clock system. *EMBO J* **22**, 2127-2134 (2003).

97. Y. Xu, T. Mori, C. H. Johnson, Cyanobacterial circadian clockwork: roles of KaiA, KaiB and the kaiBC promoter in regulating KaiC. *EMBO J* **22**, 2117-2126 (2003).

98. H. Iwasaki *et al.*, A kaiC-interacting sensory histidine kinase, SasA, necessary to sustain robust circadian oscillation in cyanobacteria. *Cell* **101**, 223-233 (2000).

99. K. Ito-Miwa, Y. Furuike, S. Akiyama, T. Kondo, Tuning the circadian period of cyanobacteria up to 6.6 days by the single amino acid substitutions in KaiC. *Proc Natl Acad Sci U S A* **117**, 20926-20931 (2020).

100. G. K. Chow *et al.*, A Night-Time Edge Site Intermediate in the Cyanobacterial Circadian Clock Identified by EPR Spectroscopy. *J Am Chem Soc* **144**, 184-194 (2022).

101. J. Heisler, A. Chavan, Y. G. Chang, A. LiWang, Real-Time In Vitro Fluorescence Anisotropy of the Cyanobacterial Circadian Clock. *Methods Protoc* **2**, (2019).

102. C. S. Theile *et al.*, Site-specific N-terminal labeling of proteins using sortase-mediated reactions. *Nat Protoc* **8**, 1800-1807 (2013).

103. C. P. Guimaraes *et al.*, Site-specific C-terminal and internal loop labeling of proteins using sortase-mediated reactions. *Nat Protoc* **8**, 1787-1799 (2013).

104. A. G. Chavan *et al.*, Reconstitution of an intact clock reveals mechanisms of circadian timekeeping. *Science* **374**, eabd4453 (2021).

105. B. Guo *et al.*, Monitoring ATP hydrolysis and ATPase inhibitor screening using (1)H NMR. *Chem Commun (Camb)* **50**, 12037-12039 (2014).

106. A. H. West, A. M. Stock, Histidine kinases and response regulator proteins in two-component signaling systems. *Trends Biochem Sci* **26**, 369-376 (2001).

107. P. B. Straughn *et al.*, Modulation of Response Regulator CheY Reaction Kinetics by Two Variable Residues That Affect Conformation. *J Bacteriol* **202**, (2020).

108. M. L. Paddock, J. S. Boyd, D. M. Adin, S. S. Golden, Active output state of the Synechococcus Kai circadian oscillator. *Proc Natl Acad Sci U S A* **110**, E3849-3857 (2013).

109. J. S. Boyd, J. R. Bordowitz, A. C. Bree, S. S. Golden, An allele of the crm gene blocks cyanobacterial circadian rhythms. *Proc Natl Acad Sci U S A* **110**, 13950-13955 (2013).

110. J. Ungerer, H. B. Pakrasi, Cpf1 Is A Versatile Tool for CRISPR Genome Editing Across Diverse Species of Cyanobacteria. *Sci Rep* **6**, 39681 (2016).

111. M. Nakajima, H. Ito, T. Kondo, In vitro regulation of circadian phosphorylation rhythm of cyanobacterial clock protein KaiC by KaiA and KaiB. *FEBS Lett* **584**, 898-902 (2010).

112. J. Chew, E. Leypunskiy, J. Lin, A. Murugan, M. J. Rust, High protein copy number is required to suppress stochasticity in the cyanobacterial circadian clock. *Nat Commun* **9**, 3004 (2018).

113. M. Kaur, A. Ng, P. Kim, C. Diekman, Y. I. Kim, CikA Modulates the Effect of KaiA on the Period of the Circadian Oscillation in KaiC Phosphorylation. *J Biol Rhythms* **34**, 218-223 (2019).

114. R. G. Garces, N. Wu, W. Gillon, E. F. Pai, Anabaena circadian clock proteins KaiA and KaiB reveal a potential common binding site to their partner KaiC. *EMBO J* **23**, 1688-1698 (2004).

115. Y. Xu, T. Mori, C. H. Johnson, Circadian clock-protein expression in cyanobacteria: rhythms and phase setting. *EMBO J* **19**, 3349-3357 (2000).

116. C. K. Holtman *et al.*, High-throughput functional analysis of the Synechococcus elongatus PCC 7942 genome. *DNA Res* **12**, 103-115 (2005).

117. K. Imai, Y. Kitayama, T. Kondo, Elucidation of the role of clp protease components in circadian rhythm by genetic deletion and overexpression in cyanobacteria. *J Bacteriol* **195**, 4517-4526 (2013).

118. H. Liu, J. H. Naismith, An efficient one-step site-directed deletion, insertion, single and multiple-site plasmid mutagenesis protocol. *BMC Biotechnol* **8**, 91 (2008).

119. C. A. Schneider, W. S. Rasband, K. W. Eliceiri, NIH Image to ImageJ: 25 years of image analysis. *Nat Methods* **9**, 671-675 (2012).

120. A. Moore, T. Zielinski, A. J. Millar, Online period estimation and determination of rhythmicity in circadian data, using the BioDare data infrastructure. *Methods Mol Biol* **1158**, 13-44 (2014).

121. T. Zielinski, A. M. Moore, E. Troup, K. J. Halliday, A. J. Millar, Strengths and limitations of period estimation methods for circadian data. *PLoS One* **9**, e96462 (2014).

122. S. R. Mackey, J. L. Ditty, E. M. Clerico, S. S. Golden, Detection of rhythmic bioluminescence from luciferase reporters in cyanobacteria. *Methods Mol Biol* **362**, 115-129 (2007).

123. A. Taton *et al.*, Broad-host-range vector system for synthetic biology and biotechnology in cyanobacteria. *Nucleic Acids Res* **42**, e136 (2014).

124. E. M. Clerico, J. L. Ditty, S. S. Golden, Specialized techniques for site-directed mutagenesis in cyanobacteria. *Methods Mol Biol* **362**, 155-171 (2007).

125. J. Elhai, A. Vepritskiy, A. M. Muro-Pastor, E. Flores, C. P. Wolk, Reduction of conjugal transfer efficiency by three restriction activities of Anabaena sp. strain PCC 7120. *J Bacteriol* **179**, 1998-2005 (1997).

126. J. Elhai, C. P. Wolk, Conjugal transfer of DNA to cyanobacteria. *Methods Enzymol* **167**, 747-754 (1988).

127. S. S. Golden, L. A. Sherman, Optimal conditions for genetic transformation of the cyanobacterium Anacystis nidulans R2. *J Bacteriol* **158**, 36-42 (1984).

128. N. B. Ivleva, S. S. Golden, Protein extraction, fractionation, and purification from cyanobacteria. *Methods Mol Biol* **362**, 365-373 (2007).

129. D. G. Welkie *et al.*, Genome-wide fitness assessment during diurnal growth reveals an expanded role of the cyanobacterial circadian clock protein KaiA. *Proc Natl Acad Sci U S A* **115**, E7174-E7183 (2018).

130. T. G. Battye, L. Kontogiannis, O. Johnson, H. R. Powell, A. G. Leslie, iMOSFLM: a new graphical interface for diffraction-image processing with MOSFLM. *Acta Crystallogr D Biol Crystallogr* **67**, 271-281 (2011).

131. P. R. Evans, G. N. Murshudov, How good are my data and what is the resolution? *Acta Crystallogr D Biol Crystallogr* **69**, 1204-1214 (2013).

132. A. J. McCoy *et al.*, Phaser crystallographic software. *J Appl Crystallogr* **40**, 658-674 (2007).

133. D. Liebschner *et al.*, Macromolecular structure determination using X-rays, neutrons and electrons: recent developments in Phenix. *Acta Crystallogr D Struct Biol* **75**, 861-877 (2019).

134. P. Emsley, B. Lohkamp, W. G. Scott, K. Cowtan, Features and development of Coot. *Acta Crystallogr D Biol Crystallogr* **66**, 486-501 (2010).

135. E. F. Pettersen *et al.*, UCSF Chimera--a visualization system for exploratory research and analysis. *J Comput Chem* **25**, 1605-1612 (2004).

136. M. F. Sanner, A. J. Olson, J. C. Spehner, Reduced surface: an efficient way to compute molecular surfaces. *Biopolymers* **38**, 305-320 (1996).

137. E. F. Pettersen *et al.*, UCSF ChimeraX: Structure visualization for researchers, educators, and developers. *Protein Sci* **30**, 70-82 (2021).

138. C. R. Bagshaw, *Biomolecular kinetics : a step-by-step guide*. Foundations of biochemistry and biophysics (CRC Press, Taylor & Francis Group, Boca Raton, 2017), pp. xxiv, 445 pages.

139. P. Kuzmic, Program DYNAFIT for the analysis of enzyme kinetic data: application to HIV proteinase. *Anal Biochem* **237**, 260-273 (1996).

140. S. Diamond, D. Jun, B. E. Rubin, S. S. Golden, The circadian oscillator in Synechococcus elongatus controls metabolite partitioning during diurnal growth. *Proc Natl Acad Sci U S A* **112**, E1916-1925 (2015).

141. R. Pattanayek, Y. Xu, A. Lamichhane, C. H. Johnson, M. Egli, An arginine tetrad as mediator of input-dependent and input-independent ATPases in the clock protein KaiC. *Acta Crystallogr D Biol Crystallogr* **70**, 1375-1390 (2014).

142. G. Dong *et al.*, Elevated ATPase activity of KaiC applies a circadian checkpoint on cell division in Synechococcus elongatus. *Cell* **140**, 529-539 (2010).

143. A. Mukaiyama *et al.*, Conformational rearrangements of the C1 ring in KaiC measure the timing of assembly with KaiB. *Sci Rep* **8**, 8803 (2018).

144. K. Oyama, C. Azai, J. Matsuyama, K. Terauchi, Phosphorylation at Thr432 induces structural destabilization of the CII ring in the circadian oscillator KaiC. *FEBS Lett* **592**, 36-45 (2018).

145. H. Ito *et al.*, Autonomous synchronization of the circadian KaiC phosphorylation rhythm. *Nat Struct Mol Biol* **14**, 1084-1088 (2007).

146. L. Hong, B. P. Vani, E. H. Thiede, M. J. Rust, A. R. Dinner, Molecular dynamics simulations of nucleotide release from the circadian clock protein KaiC reveal atomic-resolution functional insights. *Proc Natl Acad Sci U S A* **115**, E11475-E11484 (2018).

147. K. Oyama, C. Azai, K. Nakamura, S. Tanaka, K. Terauchi, Conversion between two conformational states of KaiC is induced by ATP hydrolysis as a trigger for cyanobacterial circadian oscillation. *Sci Rep* **6**, 32443 (2016).

148. R. G. Efremov, A. Leitner, R. Aebersold, S. Raunser, Architecture and conformational switch mechanism of the ryanodine receptor. *Nature* **517**, 39-43 (2015).

149. M. Jessop *et al.*, Structural insights into ATP hydrolysis by the MoxR ATPase RavA and the LdcI-RavA cage-like complex. *Commun Biol* **3**, 46 (2020).

150. Q. Z. Ye *et al.*, TRIP13 is a protein-remodeling AAA plus ATPase that catalyzes MAD2 conformation switching. *Elife* **4**, (2015).

151. S. E. Glynn, A. R. Nager, T. A. Baker, R. T. Sauer, Dynamic and static components power unfolding in topologically closed rings of a AAA+ proteolytic machine. *Nat Struct Mol Biol* **19**, 616-622 (2012).

152. A. Chavan *et al.*, Reconstitution of an intact clock reveals mechanisms of circadian timekeeping. *Science* **(in press)**, (2021).

153. J. P. Erzberger, J. M. Berger, Evolutionary relationships and structural mechanisms of AAA+ proteins. *Annu Rev Biophys Biomol Struct* **35**, 93-114 (2006).

154. N. Puri *et al.*, The molecular coupling between substrate recognition and ATP turnover in a AAA+ hexameric helicase loader. *Elife* **10**, (2021).

155. D. Ouyang *et al.*, Development and Optimization of Expression, Purification, and ATPase Assay of KaiC for Medium-Throughput Screening of Circadian Clock Mutants in Cyanobacteria. *Int J Mol Sci* **20**, (2019).

156. K. Naydenova, M. J. Peet, C. J. Russo, Multifunctional graphene supports for electron cryomicroscopy. *Proc Natl Acad Sci U S A* **116**, 11718-11724 (2019).

157. Y. Han *et al.*, High-yield monolayer graphene grids for near-atomic resolution cryoelectron microscopy. *Proc Natl Acad Sci U S A* **117**, 1009-1014 (2020).

158. B. Carragher *et al.*, Leginon: an automated system for acquisition of images from vitreous ice specimens. *J Struct Biol* **132**, 33-45 (2000).

159. G. C. Lander *et al.*, Appion: an integrated, database-driven pipeline to facilitate EM image processing. *J Struct Biol* **166**, 95-102 (2009).

160. S. H. Scheres, RELION: implementation of a Bayesian approach to cryo-EM structure determination. *J Struct Biol* **180**, 519-530 (2012).

161. Y. Z. Tan *et al.*, Addressing preferred specimen orientation in single-particle cryo-EM through tilting. *Nat Methods* **14**, 793-796 (2017).

162. N. R. Voss, C. K. Yoshioka, M. Radermacher, C. S. Potter, B. Carragher, DoG Picker and TiltPicker: software tools to facilitate particle selection in single particle electron microscopy. *J Struct Biol* **166**, 205-213 (2009).

163. K. Zhang, Gctf: Real-time CTF determination and correction. *J Struct Biol* **193**, 1-12 (2016).

164. A. M. Roseman, FindEM--a fast, efficient program for automatic selection of particles from electron micrographs. *J Struct Biol* **145**, 91-99 (2004).

165. R. A. Nicholls, M. Fischer, S. McNicholas, G. N. Murshudov, Conformation-independent structural comparison of macromolecules with ProSMART. *Acta Crystallogr D Biol Crystallogr* **70**, 2487-2499 (2014).

166. P. Emsley, K. Cowtan, Coot: model-building tools for molecular graphics. *Acta Crystallogr D Biol Crystallogr* **60**, 2126-2132 (2004).

167. P. D. Adams *et al.*, PHENIX: a comprehensive Python-based system for macromolecular structure solution. *Acta Crystallogr D Biol Crystallogr* **66**, 213-221 (2010).

168. T. I. Croll, ISOLDE: a physically realistic environment for model building into low-resolution electron-density maps. *Acta Crystallogr D Struct Biol* **74**, 519-530 (2018).

169. V. B. Chen *et al.*, MolProbity: all-atom structure validation for macromolecular crystallography. *Acta Crystallogr D Biol Crystallogr* **66**, 12-21 (2010).

170. C. UniProt, UniProt: the universal protein knowledgebase in 2021. *Nucleic Acids Res* **49**, D480-D489 (2021).

171. F. Sievers, D. G. Higgins, The Clustal Omega Multiple Alignment Package. *Methods Mol Biol* **2231**, 3-16 (2021).

172. F. Hayashi *et al.*, ATP-induced hexameric ring structure of the cyanobacterial circadian clock protein KaiC. *Genes Cells* **8**, 287-296 (2003).

173. S. R. Mackey, S. S. Golden, Winding up the cyanobacterial circadian clock. *Trends Microbiol* **15**, 381-388 (2007).

174. J. K. Blackwood *et al.*, Structural and functional insights into DNA-end processing by the archaeal HerA helicase-NurA nuclease complex. *Nucleic Acids Res* **40**, 3183-3196 (2012).

175. J. L. Burgess *et al.*, Spa47 is an oligomerization-activated type three secretion system (T3SS) ATPase from Shigella flexneri. *Protein Sci* **25**, 1037-1048 (2016).

176. C. Huang, G. Li, W. J. Lennarz, Dynamic flexibility of the ATPase p97 is important for its interprotomer motion transmission. *Proc Natl Acad Sci U S A* **109**, 9792-9797 (2012).